UNIVERSITY OF TRENTO - Italy

**International Doctoral School in Biomolecular Sciences**
**XXV Cycle**

# "CHOLESTEROL-DEPENDENT CYTOLYSINS AND PERFORIN: SIMILAR PORE-FORMING MECHANISMS IN PATHOGENIC ATTACK AND HUMAN IMMUNE DEFENSE"


**Ph.D. student**

***Marta Marchioretto***

*University of Trento*

*CNR - Institute of Biophysics*

**Tutor**

Mauro Dalla Serra

*CNR - Institute of Biophysics*

**Advisor**

Valeria Antonini

*CNR - Institute of Biophysics*


**April 2013**

# Declaration

I confirm that this is my own work and the use of all material from other sources has been properly and fully acknowledged.

The research work of doctoral thesis was carried out at the Institute of Biophysics, CNR, in Trento with a scholarship in the honor of Gianfranco Menestrina.

Atomic force microscopy was performed in the laboratory of Cecilia Pederzolli at Bruno Kessler Foundation.

Protein production/purification and primary structural characterization was performed at the laboratory of Gregor Anderluh at the National Institute of Chemistry, Ljubljana (Slovenia).

# Abstract

MACPF/CDCs proteins are a huge family of pore-forming proteins present from the bacteria to the human genera. Cholesterol-dependent cytolysins (CDCs) are a family of toxins that participate in bacterial infection pathway at the membrane level. Great interest in this family is due to their similarity, in structure and in pore-forming mechanism, with some human immune system proteins (MACPF). We focused our attention particularly on two bacterial CDCs, Perfringolysin O and Listeriolysin O, and on the human protein Perforin, which is involved in the apoptotic pathway facilitating Granzyme release. In the literature, two possible configurations of CDCs and Perforin pores are proposed: ring and arc structures that could have different implications on the biological mechanism of action of these pore-forming proteins. By electrophysiological measurements and atomic force microscopy technique on different artificial membrane, we are able to enrich the ring and the arc fraction and demonstrate that both kinds of pore are active, i.e. conduct ions.

Thus, my PhD work underlines two physiological structures which are involved in several ways, more than merely by disrupting membrane integrity, in pathogenic attack (bacterial CDCs proteins) as well as in immune response (human Perforin proteins).

# Summary

# List of Figures

# List of Tables

# 1. Introduction

## 1.1. *Pore-forming Proteins*

Pore-forming proteins (PFPs) are soluble proteins that are able to bind to cellular membrane, oligomerize on the lipid surface and insert into it as a trans-membrane form.

PFPs are associated with bacterial infections where they act as weapons to facilitate bacterial survival into the host organism. The best characterized class is that of bacterial pore-forming toxins (PFTs), which represents one-third of all Gram-positive and Gram-negative bacteria toxins characterized till now. However, pore-forming proteins are also present in eukaryotic organisms, as members of the immune system or as main actors in attacking prey.

A primary and simple classification of PFPs can be based on the structure of their spanning portion: ***α-PFTs***, proteins that form pores by α-helix structures, and ***β-PFTs***, pores formed by β-strand structure.

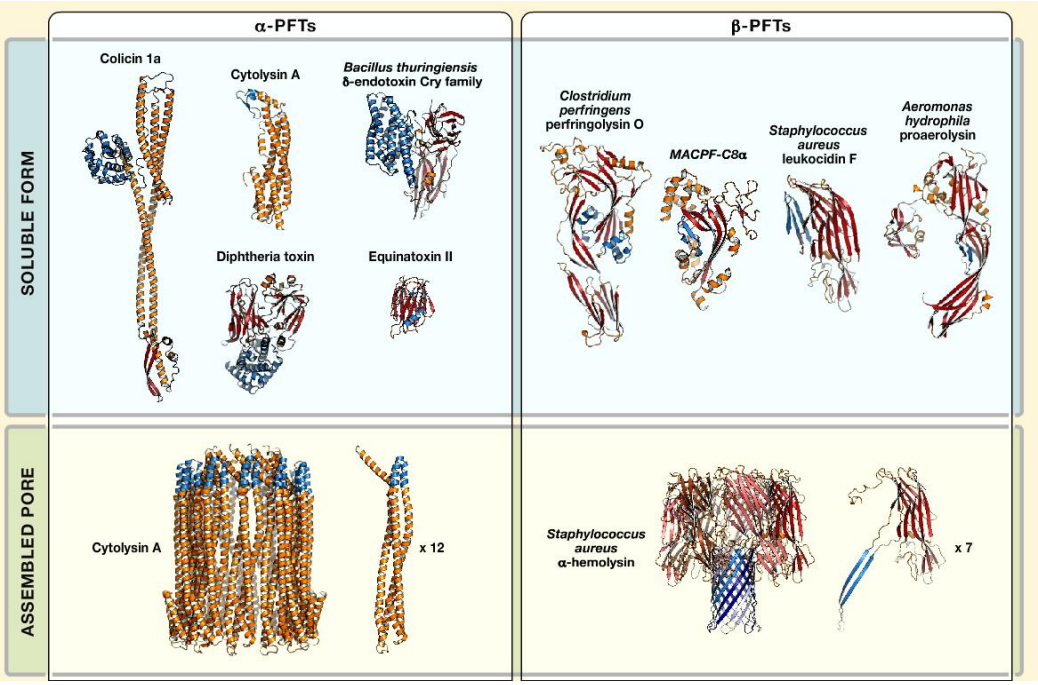


**Figure 1.1 Classification of pore-forming toxins.**

PFTs can be divided into two groups on the basis of their spanning structure in the assembled pore: α-helix and β-barrel. Upper part of the panel presents some examples of the two PFTs group. Lower part presents an example for each group of an assembled pore structure. (Figure taken from Mueller and Ban, 2010)

In Figure 1.1, there are depicted some known PFTs structures of soluble form and assembled pore.

## 1.2. MACPF/CDCs super-family

Inside PFTs' classification, it is possible to identify other protein sub-classifications. In particular, inside the β-PFTs, a large number of toxins can be grouped together by their dependence on membrane cholesterol to form the Cholesterol-Dependent Cytolysins (CDCs) family. In the following Table 1.1, beside other examples of PFTs of the two main groups (α and β), is reported the sub-classification of CDCs family and some toxin examples.

| Toxin type | Species | Toxin | Receptor[b] | Pore diameter (nm) | $M_w$ (kDa)[c] |
|---|---|---|---|---|---|
| **α-Pore-forming toxins** | | | | | |
| Colicins | | | | | |
| | *Escherichia coli* | Colicin Ia | Cir | 2 | 67 |
| Actinoporins | | | | | |
| | *Actinia equina* | Equinatoxin II | lipids | 2 | 24 |
| **β-Pore-forming toxins** | | | | | |
| Cholesterol-dependent cytolysins[d] | | | | | |
| | *Arcanobacterium pyogenes* | Pyolysin | Cholesterol | 250–350 | 62 |
| | *Bacillus anthracis* | Anthrolysin O (ALO) | Cholesterol | 250–350 | 57 |
| | *Clostridium botulinum* | Botulinolysin | Cholesterol | 250–350 | 58 |
| | *Clostridium perfringens* | Perfringolysin O (PFO) | Cholesterol | 250–350 | 56 |
| | *Clostridium tetani* | Tetanolysin | Cholesterol | 250–350 | 59 |
| | *Gardnerella vaginalis* | Vaginolysin | CD59/cholesterol | 250–350 | 57 |
| | *Listeria ivanovii* | Ivanolysin | Cholesterol | 250–350 | 59 |
| | *Listeria monocytogenes* | Listeriolysin O (LLO) | Cholesterol | 250–350 | 59 |
| | *Streptococcus intermedius* | Intermedilysin (ILY) | CD59/cholesterol | 250–350 | 58 |
| | *Streptococcus pneumoniae* | Pneumolysin (PLY) | Cholesterol | 250–350 | 53 |
| | *Streptococcus pyogenes* | Streptolysin O (SLO) | Cholesterol | 250–350 | 64 |
| **Aerolysin and related toxins** | | | | | |
| | *Aeromonas hydrophila* | Aerolysin | GPI-anchored proteins | 2–3 | 54 |
| | *Chlorohydra viridissima* | Hydralysin-1 | ND | 1–2 | 26 |
| **Others** | | | | | |
| | *Bacillus anthracis* | Anthrax toxin (PA moiety) | TEM8/CMG2 | 1–2 | 86 |
| | *Staphylococcus aureus* | α-Hemolysin | ADAM-10 | 2–3 | 36 |
| **Others** | | | | | |
| | *Helicobacter pylori* | Vacuolating cytotoxin (VacA) | Several | 6–10 | 140 |

**Table 1.1 List of pore-forming toxins classified by their pore structure.**

PFTs are divided in α-, β- and others PFTs. Inside β-toxins group, the more represented proteins belong to the Cholesterol-Dependent Cytolysins. Note that CDCs pore diameter is erroneously reported in *Å* and should be read 25-35nm. Table from Hamon et al., 2012.

CDCs is a huge family of pore-forming toxins that share sequence and structural similarity and they also have similar pore-forming activity, i.e. sterol-dependence and pore formation mechanism. These toxins are produced by Gram-positive bacteria; only very recently two of them are found in Gram-negative bacteria (see below). Much interest in this family of toxins was attracted when a high 3D structural similarity was discovered with another family of pore-forming proteins belonging to mammalian cells, the membrane-attack complex/perforin (MACPF) family. In fact, besides PFTs with high sequence similarity there are examples of proteins diverse in sequence but with high 3D-structural similarities,

i.e. MACPF/CDCs domain and Bcl architecture and *E.coli* pore forming colicins (Anderluh and Lakey, 2008).

MACPFs are a group of proteins that share a common domain with perforin and with the complement membrane attack complex (from which the origin of the family name) and they are involved in several cell mechanisms, i.e. immune defense, embryonic development or neurobiological networks. It is known for years that some of them are able to form oligomeric pore complexes (like complement C9 protein and perforin), but the detailed pore-forming mechanism is still not completely understood. A few years ago, Rosado et al. discovered that the MACPF domain structure is very similar to the fold shape of domains D1 and D3 in CDC proteins (Rosado et al., 2007) opening the investigation about other possible similarity (pore structure, mechanism..).

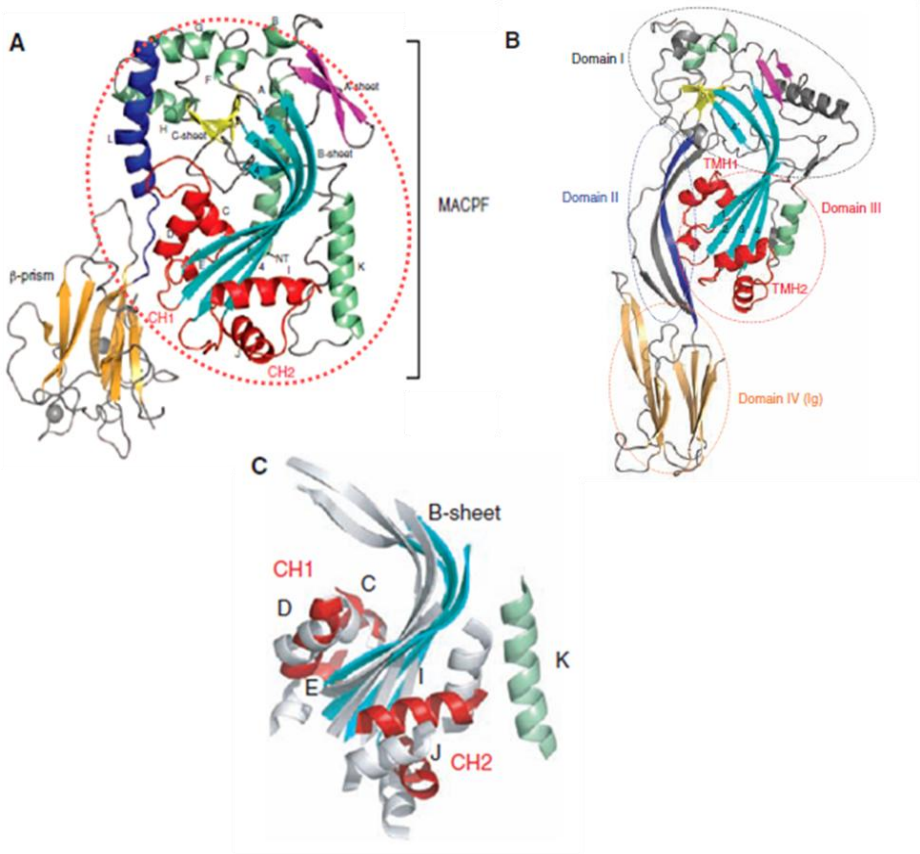


**Figure 1.2 Structural comparison between Plu-MACPF protein and perforin.**

A) Plu-MACPF (bacterial MACPF protein) structure: MACPF domain is highlighted by red dotted oval; the two α-helices CH1 and CH2 are colored in red. B) Perfringolysin O structure: each domain are signed by an oval dotted shape. Domain I and III are the corresponding part of MACPF domain. The two TMH1 and TMH2 are colored in red. All core elements of secondary structure common to both MACPF and CDCs are colored accordingly. C) Super-imposition of the similar cores of Plu-MACPF and PFO (Figure modified from Rosado et al., 2007)

So starting from this work, the members of these two families are associated into a super-family, the CDC/MACPF super-family, and the knowledge on CDCs is applied to study and characterize the less known MACPF family. In fact, only in recent years the crystal structure of perforin and MAC protein have been discovered (perforin crystal, Law et al., 2010), (Kondos et al., 2010), (complement C6 crystal, Aleshin et al., 2012). The conclusion that these works suggest is that the similarity in domain conformation is also reflected in a similar pore structure and mechanism: so studying both CDCs and MACPF proteins can be a good way to a deeper understanding of the oligomerization and pore formation mechanism.

## *1.3. Cholesterol-dependent cytolysins*

Cholesterol-dependent cytolysins (CDCs) known so far are 28 single chain pore-forming proteins produced by a large spectrum of Gram-positive bacteria, such as *Clostridium*, *Streptococcus*, *Bacillus* and *Listeria* genera. Recently, Hotze et al., 2012 reported the first CDC proteins from Gram-negative bacterial species, such as *Desulfobulbus propionicus* species Widdel 1981 (desulfolysin or DLY) and *Enterobacter ligolyticus* (formely *E.cloacae*) SCF1 (enterolysin or ELY). All CDCs-producing bacteria (except *Listeria monocitogenes* and *Listeria ivanovii*) are extracellular pathogens that use these toxins to carry out their pathogenic attack and enter the host cells. The two *Listeria* species are, instead, intracellular pathogens that are usually spontaneously uptaken by the cells and their pathogenic action is carried out inside the cytoplasm of the host cells. Another *Listeria* species is once more an exception inside this family: in fact, all CDCs are produced by bacteria to be pathogenic for human and/or animal, except the toxin Seeligerolysin O (LSO) from *L. seeligeri* which is considered a non-pathogenic bacterium (Alouf et al., 2006).

CDCs are also known as thiol-activated cytolysins, since it was early discovered that their activity was activated by thiol-reducing agents; by the way, the letter "O" at the end of their names reflects a supposed sensitivity of the toxin in the presence of oxygen. CDCs are produced as water soluble monomers of 50-60 kDa that recognize their membrane target, cholesterol, bind and assemble to finally form a huge β-barrel pore complex. Membrane cholesterol is present in all eukaryotic cells and it is very important in pathogenic processes such as virus fusion and budding as much as in infection caused by CDCs-producing bacteria.

### 1.3.1. Sequence and structure of CDCs

Many CDCs sequence are already known but the similarity at amino acidic level among them is not so high, it varies from 40 to 70%, even if some regions are very conserved. In particular, a sequence of eleven amino acids in the C-terminal region of the proteins is the most conserved part. Mutagenesis of the alanine residue to a cysteine in PLO (Ala is also present in ILY sequence in Figure 1.3 alignment) gives rise to the thiol-sensitivity of the

toxin (Billington et al., 2002) and vice versa a substitution of the cysteine to alanine in Pneumolysin (PLY) results in a fully active toxin (Saunders et al., 1989).

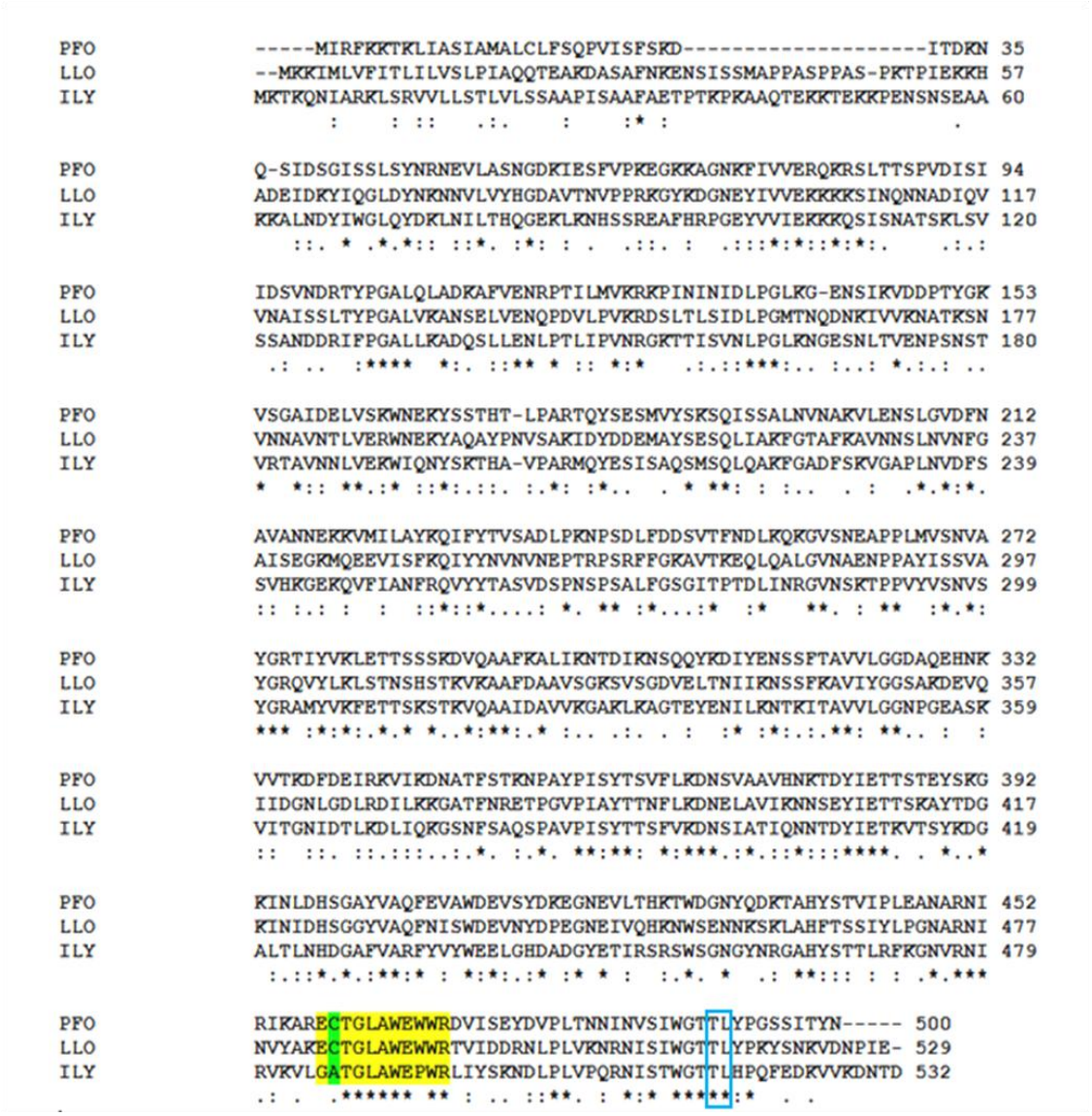


**Figure 1.3 PFO, LLO and PLY sequence alignment.**

Sequence alignment made using PFO (Q0TUS0), LLO (P13128), ILY (Q9LCB8) sequences. (*****), amino acid identity; (**:**), conservative substitution. In yellow, the undecapeptide sequence with inside highlighted the cysteine residue in green. The cyan box points out the two highly conserved Thr and Leu residues responsible to membrane binding.

In Figure 1.3, the sequence alignment of three CDCs shows the amino acid similarity and some characteristic features of this family of protein. Most interestingly is the structural similarity and the similar rearrangement in pore formation.

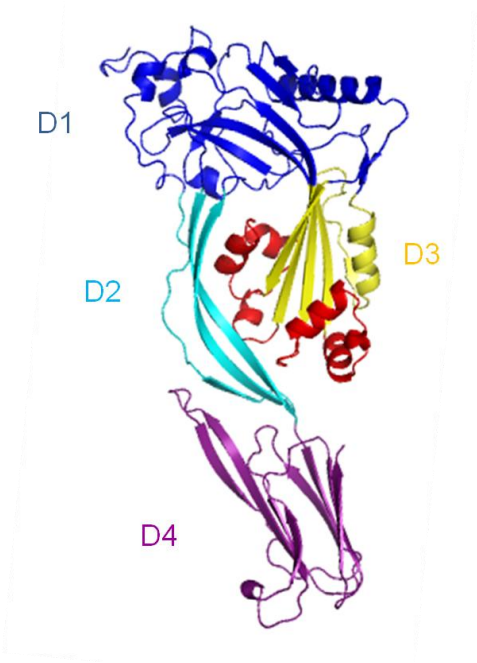


**Figure 1.4 PFO tridimensional structure.**

Pefringolysin O (PDB ID: 1PFO): Domain D1 is colored in blue, Domain D2 is colored in cyan, Domain D3 is colored in yellow and red; Domain D4 is colored in violet. The red α-helices in D3 are the two trans-membrane helices (TMH1 and 2) that, after membrane insertion, become the pore wall β-hairpins. (Cartoon image of 3D structure created by PyMOL).

The first crystal structure of a CDC protein, Perfringolysin O, was solved by Rossjohn et al., in 1997, but other studies on PLY demonstrated the same monomer shape and domain division (PLY crystal, Tilley et al., 2005). PFO monomer structure has a 3D elongated shape, as reported in Figure 1.4, that can be divided into four domains: two domains mainly composed of β-sheets structures and two domains in which α-helix structures are organized around a β-barrels core.

- ✓ ***Domain 1 (N-term):*** region implicated in the subunit-subunit interaction and in protein oligomerization. A binding experiment with a monoclonal antibody against the region of β5-sheet (closed to D3 interface) of PLY showed that Ab-β5 sheet binding prevents PLY oligomerization into the pore complex (De los Toyos et al., 1996). Ramachandran et al., (2004) confirmed that PFO monomer-monomer interaction occurs between β-strands in domains D1-D3 junction.

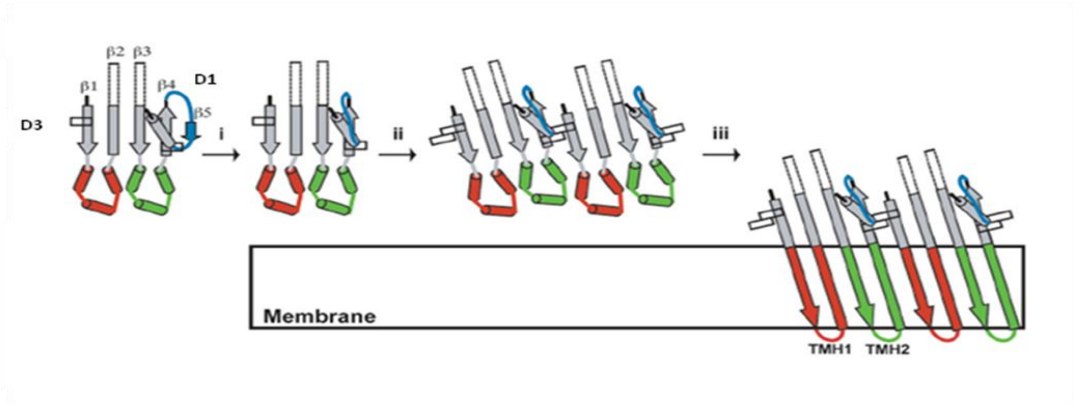


**Figure 1.5 Mechanism of PFO oligomerization.**

i) membrane binding through D4 domain modifies the β4 and β5 orientation; ii) oligomerization of PFO monomers on the membrane surface; iii) insertion of the oligomer TMHs into the membrane. D1 domain not shown, upper part of the β-barrels and α-helices. (Figure modified from Ramachandran et al., 2004).

- ✓ ***Domain 2:*** linkage domain composed of two long β-barrels that are subject to a tremendous collapse during monomer insertion into the bilayer, a vertical collapse that allows a significant movement of D3 domains towards the membrane bilayer during pore formation.

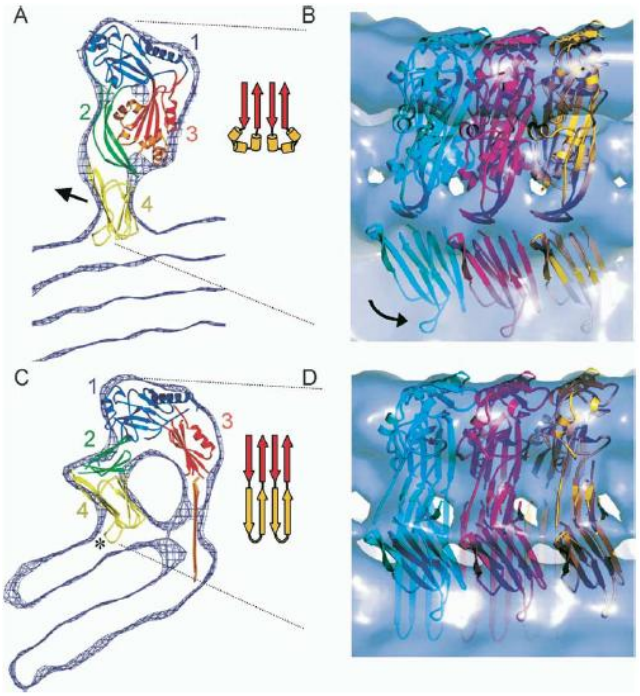


**Figure 1.6 Atomic structure fits of PLY pre-pore and pore structure.**

A) and C) cross-section of pre-pore and pore map with the four domains colored in blue (1), green (2), red/orange (3) and yellow (4). B) and D) view of three subunits from the outside of the pore. (Figure taken from Tilley et al., 2005)

- ***Domain 3:*** β-barrel core flanked by two α-helices (TMH1 and TMH2). This part of the molecule is the most interesting. In fact, it is subject to a significant structural alteration between the monomer and the membrane-inserted form. During pore opening, the β-hairpin's core relaxes and straightens becoming the upper part of the luminal wall and meanwhile the two α-helices unfurl and become two β-hairpins (bottom part of the pore).

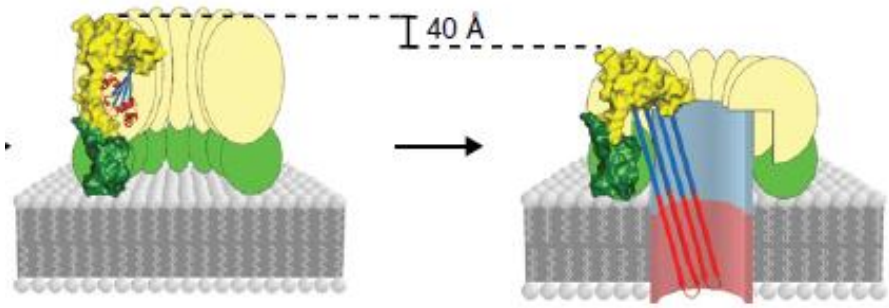


**Figure 1.7 D3 rearrangement during pore insertion.**

β-sheets in cyan are the upper part of the luminal pore and α-helices in red become β-hairpins and the trans-membrane part of the pore (Figure taken from Dunstone and Tweten, 2012)

- ***Domain 4:*** C-terminal Ig-like domain that is the membrane binding part of the protein. For many years, the Tryptophan-rich undecapeptide (ECTGLAWEWWR) was considered the cholesterol binding motif. Farrand et al., in 2010, instead, identified the real actors in membrane binding: a pair of highly conserved amino acids (Thr-Leu) that are responsible for cholesterol recognition and binding.

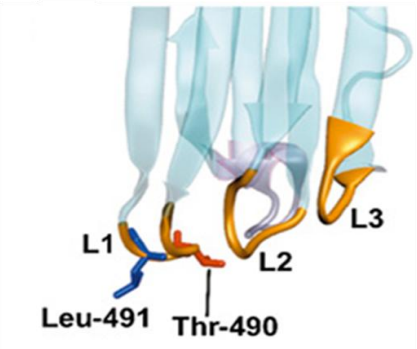


**Figure 1.8 PFO Domain D4 features.**

Tip part of D4 domain in which three hydrophobic loops are present, L1, L2 and L3 colored in yellow. The two amino acids Thr-490 and Leu-491, essential for cholesterol recognition and binding, are colored in red and blue respectively. (Figure taken from Farrand et al., 2010).

Once the two amino acids recognize and bind cholesterol, two of the three short hydrophobic loops (L2 and L3), at the very tip of Domain D4, insert into the membrane and block the protein on the lipid surface (Ramachandran et al., 2002). PFO mutagenesis of both the Thr-Leu and the two loop regions demonstrated the crucial role of these elements for PFO lytic activity. Even if the undecapeptide is not considered the binding motif anymore and its role is not clear yet, it is still a critical element for CDCs binding. Since it is located closed to the bilayer interface in the bound monomer, the most accepted hypothesis is that the tryptophan residues of the undecapeptide can be involved in the initial protein approach to the membrane.

### 1.3.2. Listeriolysin O

*Listeria monocitogenes* is a food-borne pathogen that causes severe infection in humans, especially in pregnant woman and immune compromised people. *L. monocitogenes* is a Gram-positive, intracellular bacteria able to spread cell to cell without being exposed to the immune system and also able to pass three human barriers: the intestinal barrier, the blood-brain barrier and the feto-placental barrier. After entry into host cells by phagocytosis (through E-cadherin and/or EGF receptor) or induced uptake (Vadia et al., 2011), this pathogen initially occupies a phagosome compartment; then, thanks to the action of Listeriolysin O (LLO), the bacteria is released into the host cytosol and start a rapid replication.

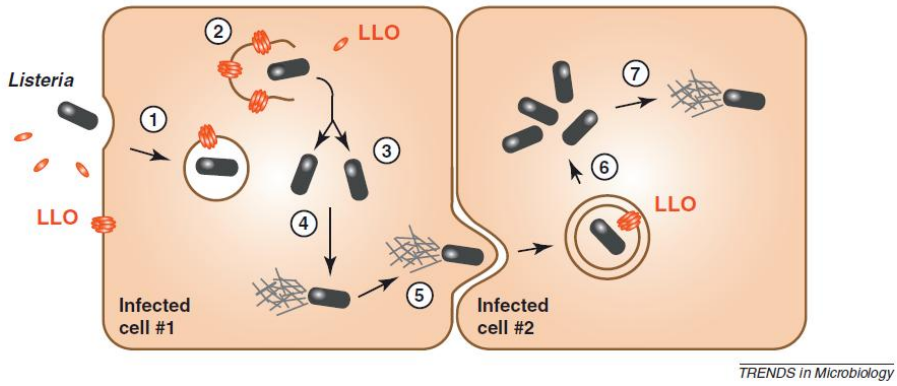


**Figure 1.9 Infective pathway of *L. monocytogenes*.**

LLO pore-forming protein is reported in the possible site of action during *Listeria* infection. (Figure modified from Hamon et al., 2012).

LLO is known as the primary virulence factor *of L. monocitogenes* since it was identified and purified by Njoku-Obi et al., 1963. LLO toxin is a member of the Cholesterol-Dependent Cytolysins family of pore-forming proteins and within this family of toxins, it has the unique feature of acting at acidic pH (major lytic activity at pH below 6). This toxin, in fact, is produced and released by the bacteria in the external endosomal acidic environment as an active protein. Once LLO disrupts the vesicle and the bacteria is released in the host cytosol, LLO protein starts to unfold and aggregate in the neutral pH environment (Schuerch et al., 2005). The modulation of LLO activity is a crucial point for bacterial pathogenesis; it allow to avoid host cell lysis and the recruitment of immune response actors that will block *Listeria* infection (survival and replication). A also well

known role of LLO is the blockage of phagosome–lysosome fusion by generating pores that uncouple pH and calcium gradients across the phagosome membrane, and promoting, in concert with the action of two phospholipases, bacterial escape from the phagosome. As reported before, once in the cytosol, *L. monocytogenes* replicates rapidly and usurps the host actin polymerization machinery to move through the cytosol and spread into neighboring cells (see Figure 1.9).

Since the crystal structure of LLO is still unpublished and Listeriolysin O structure can be only inferred from the sequence similarity with PFO, many studies reported supposition on LLO pore structures and the amino acids involved in the pH sensitivity.

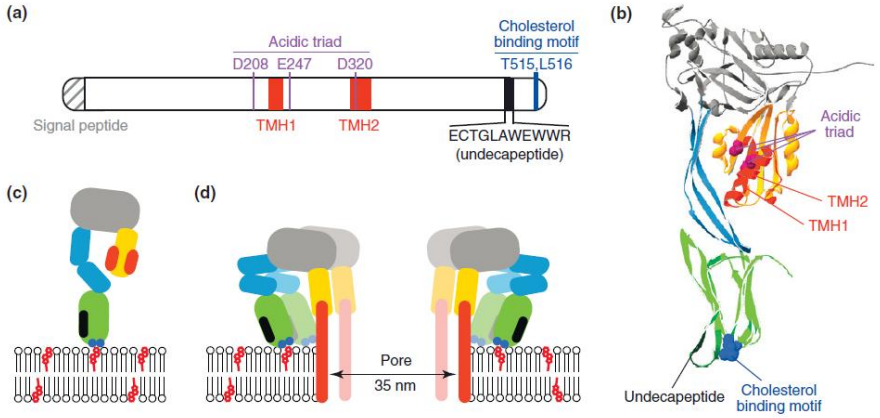


**Figure 1.10 Summary of LLO structural knowledge.**

a) sequence cartoon with reported the hallmark features; b) LLO 3D structure reconstructed on PFO similarity; c) monomer binding to the membrane; d) pore structure section with the luminal part highlighted. (Image modified from Hamon et al., 2012)

It has been reported that three negatively-charged amino acids (D208, E247 and D320) in the β-hairpins core region are responsible for LLO pH sensitivity (Schuerch et al., 2005). At physiological pH these residues completely protonate their carbossilic group in the side chain, breaking hydrogen bonds between the β-hairpins that leads to protein partial denaturation, aggregation and inactivation of the protein.

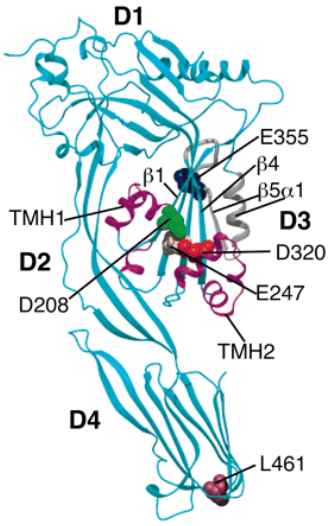


**Figure 1.11 Acidic trial on LLO supposed structure based on PFO crystal.**

LLO structure is divided in the 4 domains. In domain D3, TMH1 and TMH2 are colored in purple, the three negatively charged amino acid D208, E247, D320 are reported as colored spheres. (Image taken from Schuerch et al., 2005)

In Bavdek et al., 2007, however, the authors demonstrated that LLO shows some lytic activity at neutral pH as well, and that even this low pore-forming ability can be restored by enhancing the sterol percentage in the lipid bilayer (maintaining the temperature below 30°C).

## 1.4. MACPF family

The membrane attack complex/perforin (MACPF) family is a group of pore-forming proteins that have a common domain to the complement membrane attack complex (MAC) proteins. The MACPF domain consists of a β-barrel core flanked by two groups of α-helices, as for CDCs D1-D3 domains. Proteins belonging to this family are complement proteins of the Membrane Attack Complex and Perforin (see Figure 1.2).

### 1.4.1. Complement proteins

Complement are small proteins belonging to the innate immune system normally circulating in the blood as inactive precursor that, after a stimulation from the adaptive immune system, are rapidly activated to form the membrane attack complex. The complement membrane attack complex is a multi-protein pore assembly of C5b, C6, C7, C8αβγ, C9 monomers. These proteins have the common MACPF domain flanked by 4 to 9 auxiliary domains, with the exception of C5b and C8γ.

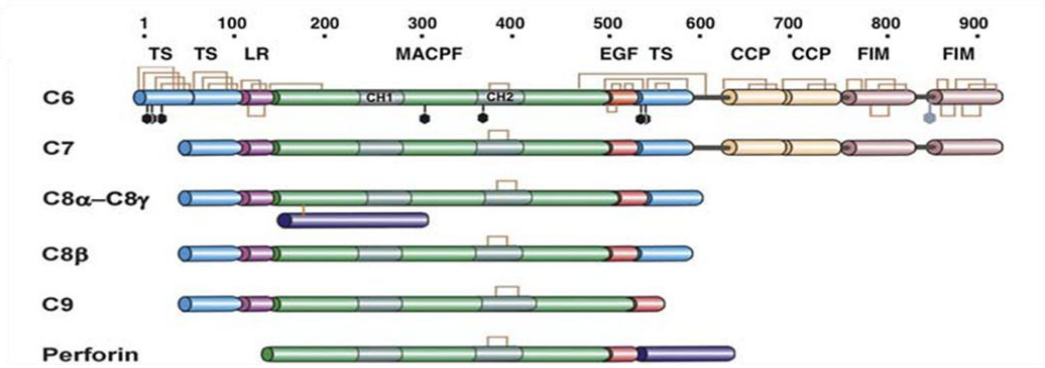


**Figure 1.12 Domain organization of complement proteins and perforin.**

MACPF domain is the central core of all the proteins (in green). TS modules are colored in cyan, LR in purple, EGF in red, CCP in light orange and FIM in pink. Perforin contains a C-terminal binding domain in violet. (Figure taken from Aleshin et al., 2012)

The formation of the huge MAC pore assembly is a sequential process that involves one monomer of each C5, C6, C7, C8α-β-γ and more units of C9 protein. The initial step of the pore-forming process consists in C5 cleavage into two regions, C5a and C5b. The C5b part is now able to bind a copy of C6 and subsequently a copy of C7. The newly formed C5b-7 complex interacts and binds to three C8 proteins (α, β and γ isoform) giving rise to the

complex that anchors the forming pore to the membrane. The pre-formed and bound C5b-C8 complex is not able to perforate the membrane by itself; the last passage to form the mature MAC lytic pore is the binding of C9 to the C8 portion and the oligomerization of other C9 units (about 12-18 monomers per pore).

What is clear from the work of Aleshin et al., 2012 is that the C5b-C8 complex has the ability to bind the membrane and partially insert into it, but then the perforation of the bilayer occurs only in the presence of C9 monomer. In fact, only C9 has a β-barrel length able to span the membrane and open a pore. The most relevant feature is the pore-forming model proposed by the authors. They assumed that the membrane perforation occurs as soon as one C9 monomer binds to the C5b-C8 complex and the small proteo-lipidic pore (see paragraph 1.5) then can grow by C9 monomers oligomerization.

### 1.4.2. Perforin

Perforin (PFN) is a 60kDa protein produced by cytotoxic T lymphocytes and Natural Killer cells during immunity response to bacterial infections, cell abnormities and cancer cells. PFN was first discovered and purified by Young et al., 1986 from granules of cloned NK-like cytolytic cells. That first work, already reported the calcium dependence of PFN cytolytic activity and, moreover, there was a primary channel characterization on planar lipid membrane that revealed an heterogeneity in size distribution (average single channel conductance 400pS in 0.1mM NaCl). So the formation of a very large trans-membrane pore was clear from the beginning. Many subsequent studies focused on PFN pore-forming activity *in vitro* but much attention was also concentrated on cellular function of this cytolytic protein of the immune system (*in vivo* characterization). In fact, it was early discovered that PFN has a key role in target cell death since more than 50 mutations of the genes are linked to familial haemophagocytic lymphohistiocytosis (type 2 FHL), a disorder that imbalances the number of the lymphocytes, in particular increasing T-cell number (resulting in anemia, tissue damages and death). Deficit of perforin activity is also linked with many other lighter disorders of the immune system.

Unlike the complement proteins of the innate immune system, perforin is not freely circulating in the blood but it is compartmentalized as an inactive protein inside the secretory granules of cytotoxic T cells and NK cells. In fact, perforin is synthesized in the endoplasmatic reticulum and bound to calreticulin (known to be its inhibitor). This protein complex passes then through the Golgi apparatus and is incapsulated into cytotoxic granules. Perforin is only one of the components of these specialized vesicles: inside this compartment, some serine proteases (granzymes, Grz) and the complex proteoglycan serglycin are also packed. The acidic pH of the granule allows maintaining Perforin protein stability. Since PFN is inactive at this pH, the producing cells become protected from its porating activity. In the cytotoxic granule, PFN lytic activity is maintained also through its binding to serglycin and by calcium sequestration by calreticulin. (Pipkin and Lieberman, 2007). Once the adaptive immune system is activated, the cytotoxic T and NK cells release the granules at the immunological synaptic level where at the neutral pH PFN is released from serglycin and the higher concentration of calcium activates PFN lytitc activity. Many studies have demonstrated the influence of PFN in the intracellular delivery of granzyme proteins, proteases able to stimulate the programmed cell death that brings the host cells to

disassemble and to be cleaned away by macrophages. Granzyme B, in fact, is an important actor of the apoptotic pathway: this protease selectively cleaves the BH3-interacting domain death agonist (BID) in two parts and the cleaved-activated BID goes to initiate the mitochondrial depolarization and the caspase pathway that leads to target cell death. The role of Grz release promoter is so far accepted by the scientific community but the mechanism of Grz delivery by PFN is still a controversial matter. The first hypothesis is that perforin makes pores into the target host membrane and Grz passes through them. Another model proposed the simultaneous uptake of PFN and Grz in endocytotic vesicles and the following release of Grz in the cytosol by PFN-dependent breaking of the endosomal vesicles (Froelich et al., 1996). Both models are based on the lytic activity of PFN but they differ in its site of action.

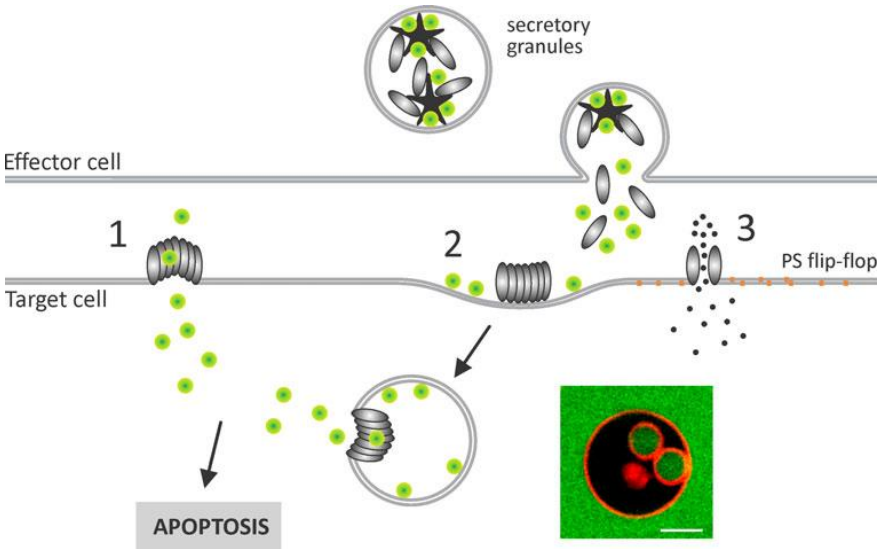


**Figure 1.13 Transfer of Grz into target cell cytosol.**

Three possible pathways of Granzyme B delivery induced by PFN activity. 1) Grz B transfer directly through PFN barrel-stave pore or smaller pore (3); 2) Grz and PFN simultaneous endocytosis cause by both a calcium-dependent response or a direct PFN stimulation of membrane invagination; 3) hybrid model: small PFN pores induce calcium influx and PS flip flop that improve the endocytotic way of Grz and PFN (Figure from Gilbert et al., 2012).

#### 1.4.2.1. Granzyme delivery

Electron microscopy experiments on cells treated with high concentration of purified PFN allow to visualize perforin pores. The high PFN concentration promotes the formation of defined ring pores on the membrane bilayer, pores with a diameter of 25-35 nm that should be large enough to allow granzyme passage (Grz dimension: 5 x 5 x 4.5 nm). The pores formed in this condition seem to be very stable and should be able to promote the unwanted cell necrosis. If this should be the mechanism of PFN/Grz action, the physiological PFN concentration in the synaptic space, which is still unknown, has therefore to be lower to guarantee granzyme uptake and controlled cell death (apoptosis) which are the real effects of PFN/Grz-containing granules of T cells and NK-cells. In cells, in fact, low concentration of purified PFN seems to be able to induce the internalization of PFN and Grz in endosomal vesicles.

In the endocytotic granzyme delivery model, PFN has the role of disrupting the endosomal membrane integrity releasing Grz in the cytosol. So PFN lytic action is performed in two different steps of the process. First, perforin released in the synaptic extracellular region is activated by high concentration of calcium and perturbs the host plasma membrane with small pores or transient pores that allow $Ca^{2+}$ influx in the host cytosol. The calcium flux then triggers cell damage repair response that consists in lysosome exocytosis and endocytosis of the damaged membrane. Perforin and Granzymes are simultaneously internalized in early-endosomal vesicles, called gigantosomes (Thiery et al., 2011). In this paper, the authors investigated how gigantosomes are formed and how granzymes are released from them. They found that PFN and Grz-containing gigantosomes are formed both with sublytic concentration of recombinant and purified PFN but also during cell-mediated cytolysis. Once internalized in gigantosomes, it takes 15 minutes to have granzymes released into the cell cytosol.

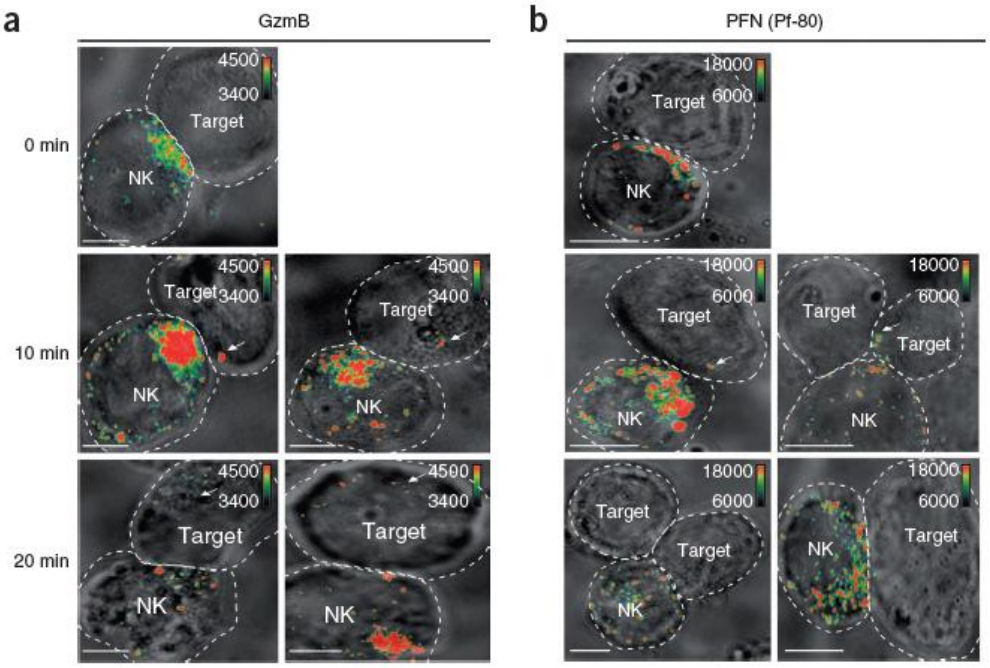


**Figure 1.14 Cell mediated cytolysis. NK cells incubated with 721.221 human B cells (as target cells) analyzed by spinning-disk confocal microscopy.**

a) Grz staining b) PFN staining with Pf-80, Ab which recognize a conformational epitope that is hidden in pore structure. So PFN is almost invisible by AB-binding in cells after PFN pores have disrupted the endosomal vesicles, i.e. in 20 min images. (Figure from Thiery et al., 2011).

The Pf-80 antibody used by Thiery et al., (2011), as shown in Figure 1.14, is an Ab previously used and characterized by Praper et al., in 2010. In this last paper, the authors analyze the pH influence in PFN binding and pore-forming activity by SPR (Surface Plasmon Resonance) technique by PFN immuno-labelling with two different commercial antibodies, Pf-80 and Pf-344. The epitope of Pf-344 is the sequence from amino acid 377 to amino acid 388, a region (at the MACPF-EGF interface) always exposes to the polar environment. Instead, concerning Pf-80, this Ab does not recognize a linear epitope but rather a conformational epitope that is not accessible when the PFN monomer is inserted into the lipid bilayer, i.e. in trans-membrane pore configuration, so its binding kinetics is very complex to be estimated. The two different epitopes of Pf-344 and Pf-80 are also evident in immune-staining experiments of HeLa cells (Thiery et al., 2011). The particular feature of Pf-80 is also useful to study PFN viability in high throughput experiments.

### 1.4.2.2. Structural features of Perforin

In 2010, Law et al. reported the crystal structure of PFN and, as other papers suggested before, the PFN monomeric structure is very similar to the shape of CDCs. The MACPF/CDC domain is located at the N-terminus; in the central region there is an EGF domain and at the C-terminus a CDC globulin like-domain, C2, is present.

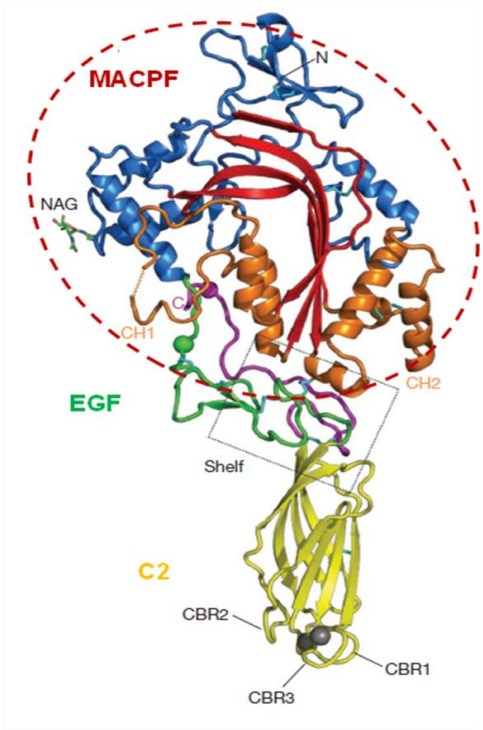


**Figure 1.15 PFN tridimensional structure.**

MACPF domain marked by dashed red circle, EGF-shelf like domain in green and C2 domain in yellow. (figure modified from Law et al., 2010)

The MACPF domain is composed of a central β-sheets core flanked by two groups of α-helices, termed CH1 and CH2 (homologous to TMH1 and TMH2 in CDC proteins). The central EGF domain, together with the extreme C-terminus, forms a shelf-like structure. C2 domain is a very important feature for PFN activity and regulation: three calcium-binding sites (CBR1,2 and 3) are located in this region. Once two calcium ions is bound in CBR1 and CBR3, the C2 domain interacts and binds to the membrane anchoring the molecule perpendicularly to the bilayer. PFN regulation by calcium is highly tuned: inside the granule, the low $Ca^{2+}$concentration and the acidic pH maintain PFN in its non active state (as I mentioned before); once perforin is released in the extracellular synaptic region high $Ca^{2+}$ concentration and neutral pH activate the protein and promote its binding,

oligomerization and pore formation. In this paper, Law and colleagues also tried to determine the monomer orientation in the pore structure.

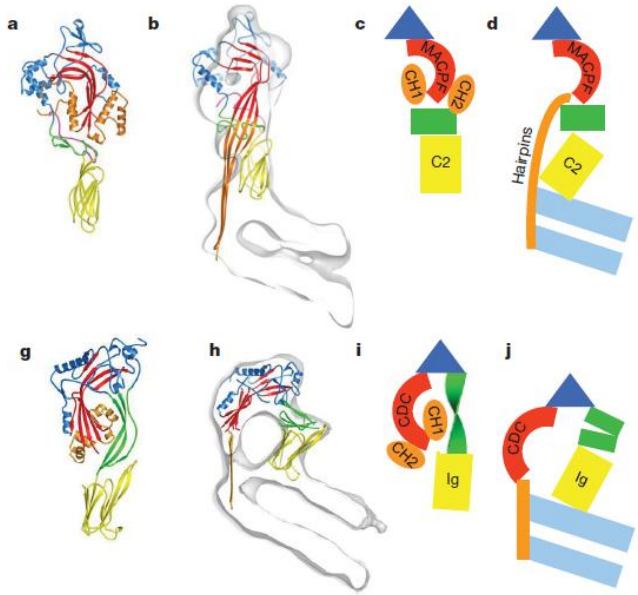


**Figure 1.16 Structural rearrangement of PFN and PFO proteins during pore formation.**

a-d) PFN monomer structure and PFN membrane-inserted structure. g-j) PFO monomeric and bound structure. Similar domain between proteins are colored with the same color, respectively. MACPF domain is proposed to be oriented on the opposite direction with respect to the analogue CDC domain. (Figure taken from Law et al., 2010)

Analyzing both the negative staining and Cryo-EM structure of the monomer unit and the pore structure in liposome, they modeled a pore structure in which MACPF domain is supposed to be inversely oriented with respect to the CDC domain in the PFO pore. A very recent paper (Gilbert et al., 2012), however, underlines how the orientation of MACPF domain couldn't be opposite to CDCs one, since the protein are philologically not so distant and there is not evidence of an intermediate structural configuration and oligomerization.

## 1.5. Pore forming mechanisms and pore activity

Many groups are working on CDC/MACPF protein structure and several proteins of both bacterial and mammalian origin have been crystallized and characterized. What is still not so clear, even if there are many cryo-EM images of the pore structure, is the pore-forming mechanism. In the literature, two major hypothesis of pore formation are present: the most accepted is a ring shape model in which monomers bind to the membrane and oligomerize till a complete proteic pre-pore ring is formed. A cooperative conformational transition permits the insertion of the transmembrane portion and the aperture of a water-filled pore into the membrane (Tilley et al., 2005), (Czajkowsky et al., 2004), (Tweten, 2005), (Hotze and Tweten, 2012). Another hypothesis, older but still not fully accepted, is the arc-shaped oligomeric pore formation (Palmer et al., 1998). The second mechanism differs on the kinetics of pore formation. CDCs, Streptolysin O in the original work by Palmer et al., bind and oligomerize on the membrane surface, but at a certain point, before the complete ring is formed, the oligomeric structure is able to insert and open a pore into the lipid bilayer. In the case of arc-shaped structure, the pore walls are completed by part of the lipid bilayer, which needs to structurally change to expose only the lipid heads to the pore lumen.

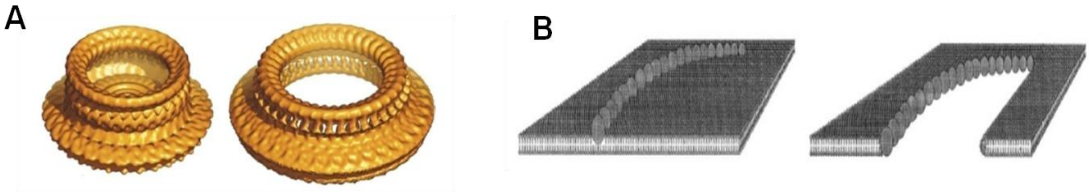


**Figure 1.17Two proposed models for CDCs pore formation.**

A) Pre-pore to pore transition, (image taken from Tilley et al., 2005); B) Arc-shaped oligomeric formation (image taken from Palmer et al., 1998).

As I said above, in the literature there are many Cryo-EM images of CDCs pore structures formed in liposome or in cell membrane and also AFM images of PFO pores on supported bilayers (Gilbert et al., 2012). As noted in the recent critical review by Gilbert et al 2012, in all the published pore images statistically relevant incomplete arc-shaped structures are reported. Those oligomeric structures are often considered transient and inactive forms of pre-pores towards the complete and fully active circular pore. Another emerging hypothesis is that CDCs can make different kind of pores depending on monomer availability, protein affinity for the membrane and some kinetic aspects linked to the

membrane fluidity. In this hypothesis, CDC proteins can form complete (and homogenous in size) ring pores or arc-shaped pores variable in dimension, as depicted in Figure 1.18.

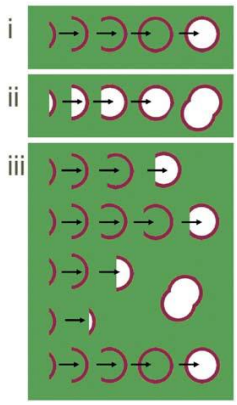


**Figure 1.18 Two pore-forming mechanisms.**

i) Pre-pore to pore models: monomers bind, oligomerize on membrane surface and when a complete ring is formed the pore is opened; ii-iii) Oligomeric pore formation: monomers bind and oligomerized but active pores can formed even if the ring structure is not completely organized (figure modified from Gilbert, 2005).

This third model proposed in the literature is also validated by some new data on perforin activity in model membranes. In fact, in Praper et al., (2011) perforin cytolytic activity was characterized by planar lipid membrane techniques on different membrane compositions and from this work, it is demonstrated that perforin is able to oligomerize and forms different pore structures depending on membrane properties.

# 2. Aim of the thesis

Membrane lipids structure (sterol and phospholipidic components) has a critical role on protein binding affinity and toxins activity, since the lipid compositions can modulate lipid packaging, sterol exposure, microdomains organization and membrane fluidity. MACPF/CDC proteins selectively bind lipid components and their binding determine their lytic activity. So it seems a crucial part for the pore-forming modeling to understand how the lipidic part of a cellular membrane can influence the binding but, most of all, the activity of these MACPF/CDC family of protein. In the literature there are already present some papers regarding the binding affinity of Perfringolysin O in different membrane compositions (Nelson et al., 2007 and Flanagan et al., 2009). What is still missing is a characterization of the lytic activity under different conditions which could be a useful starting point to understand the kind of pore that this proteins form, and solve the long-standing question of which mechanism is the correct one.

The aim of my thesis is the characterization of the pore-forming ability of some proteins belonging to this huge family of MACPF/CDCs pore-forming proteins. My attention is focused in particular on Listeriolysin O (LLO) and Perforin (PFN). LLO is very interesting because its activity is mostly at the endosomal level, a unique feature inside the CDC family, and LLO also shows a very precise mechanism of pH-dependent inactivation. Perforin is chosen because it is a very important proteins involved in apoptotic stimulation during the immune response. Since for both proteins, knowledge is missing, I decided to use Perfringolysin O (the most well known and characterized CDC) as a positive control for our analysis. The characterization of these three proteins consists on the electrophysiological measurement (pore activity) by the Planar Lipid Membrane technique and on the topographic visualization (pore structure) by Atomic Force Microscopy under several conditions. My screening will be able, hopefully, to discriminate which pore-forming mechanism is adopted by LLO and PFN, ring pore or proteolipidic pore (see Figure 1.18).

# 3. Materials and methods

# *3.1. Materials*

## 3.1.1. Lipids

All the lipids used are bought from Avanti Polar Lipids: 1-palmitoyl-2-oleoyl-sn-glycero-3-phosphocholine, **POPC** (APL, #850457); 1,2-dioleoyl-sn-glycero-3-phosphocholine, **DOPC** (APL, #850375); L-α-phosphatidylcholine (Egg, Chicken), **EggPC** (APL, #840051); cholesterol, **CHO** (APL, #700000).

## 3.1.2. Bacterial growth medium

| **Luria Bertani (LB) medium (1L)** | **Terrific Broth (TB) medium (900mL)** | **Phosphate buffer (100mL)** |
|---|---|---|
| 10g Tryptone | 12g Tryptone | 0.17M $KH_2PO_4$ (2.31g) |
| 5g Yeast Extract | 24g Yeast extract | 0.72 M $K_2HPO_4$ (12.54g) |
| 10g Sodium Chloride | 4mL glycerol | |

**Table 3.1 Table of bacterial medium recipes.**

First Column: Luria Bertani medium; second and third column: all the component for Terrific Broth medium.

**Protocol for LB liquid medium:**

Prepare LB medium as above and autoclave it on liquid cycle for 20 min at 15 psi (1.05 $kg/cm^2$).

**Protocol for LB agar plates:**

Prepare LB medium as above, but add 15 g/L agar. After autoclaving, cool to ~55°C, add antibiotic, and pour it into 10 cm plates. Let harden, then invert the plate and store at 4°C.

**Protocol for TB liquid medium:**

Prepare TB medium and phosphate buffer as reported above and autoclave them on liquid cycle for 20 min at 15 psi. Allow the solution to cool to 60°C or less and mix the two solutions.

### 3.1.3. LLO purification

Many buffers are needed during LLO purification, from bacterial lysis to final pure protein.

***Lysis Buffer***

50 mM BisTris pH 6.5

250 mM NaCl

10% glycerol

Addition of 2-mercaptoethanol and protease inhibitor to the suspension before sonication.

***Ni-NTA column buffers***

| Loading Buffer | Washing Buffer | Elution Buffer |
|---|---|---|
| 50mM Bis-Tris pH 6.5 | 50mM Bis-Tris pH 6.5 | 50mM Bis-Tris pH 6.5 |
| 250mM NaCl | 300mM NaCl | 300mM NaCl |
| 10mM Imidazole | 25mM Imidazole | 300mM Imidazole |
| 5% glycerol | 5% glycerol | 5% glycerol |

***Dialysis buffers***

| Dialysis 1 | Dialysis 2 | Dialysis 3 | Dialysis 4 |
|---|---|---|---|
| 10mM $NaH_2PO_4$ pH 5.7 | 10mM $NaH_2PO_4$ pH 5.7 | 10mM $NaH_2PO_4$ pH 5.7 | 10mM $NaH_2PO_4$ pH 5.7 |
| 250mM NaCl | 150mM NaCl | 80mM NaCl | 10mM NaCl |
| 5% glycerol | 5% glycerol | 5% glycerol | 5% glycerol |

***Cation-Exchange chromatography buffers***

| Cation-Exchange Buffer A | Cation-Exchange Buffer B |
|---|---|
| 10mM $NaH_2PO_4$ pH 5.7 | 10mM $NaH_2PO_4$ pH 5.7 |
| 10mM NaCl | 1M NaCl |
| 5% glicerol | 5% glicerol |

All the chromatographic passages were performed on AKTA-FPLC system (Pharmacia, GE Healthcare). Ni-NTA column was an homemade column regenerated every time before use. Cation Exchange chromatography was done on TSKgel SP-5PW column (Tosoh Bioscience).

### 3.1.4. Gel electrophoresis

SDS-PAGE electrophoresis was performed on precasted 4-12% acrylamide gels, NuPAGE NOVEX Bis-Tris Mini Gels (Invitrogen,# NP0321BOX). Gels were run on XCell *SureLock*® Mini-Cell (Invitrogen, #EI001) in MES Running Buffer (Invitrogen, # NP0002). hfhdd

Gels were colored with SimplyBlue Safe Stain (Invitrogen, # LC6065) and the reference Molecular weight standard was Precision Plus Protein™ Unstained Standards (Biorad, # 161-0363).

### 3.1.5. Hemolytic assay buffers

Red Blood Cells buffer is 10mM Hepes pH 7.4, 140mM NaCl, 0,1mM EDTA.

Hemolysis is followed by measuring OD at 608nm by a kinetic microplate reader (Uvmax, Molecular Devices).

### 3.1.6. Vesicles buffers

Large Unilamellar Vesicles (LUVs) were used in several assay, so lipids were dissolved in different buffers depending on the case.

***LUV buffers for AFM experiments:***

15mM $NaH_2PO_4$ buffer pH 7.4

150mM NaCl

Calcein release kinetics were followed exciting the samples at $\lambda ex$ = 485 nm and recovering the fluorescence at $\lambda em$ = 538 nm. The assay was performed on a BMG microplate reader (Flostar Galaxy pbi).

### 3.1.7. RT-PCR/DSF assay buffers

Protein aggregation was tested in a pH range from 3.5 to 9.

**pH 3.5-4-4.5-5:** 20mM Acetate, 150mM NaCl

**pH 5.5-6-6.5:** 20mM MES, 150mM NaCl

**pH 7-7.5-8:** 20mM Hepes, 150mM NaCl

**pH 8.5-9:** 20mM Glycine, 150mM NaCl

The RT-PCR/DSF assay was performed on LightCycler 480 system (Roche instruments).

### 3.1.8. Planar Lipid Membrane

PLM experiments on CDC proteins were performed at two different pHs.

| **Buffer pH 7.4** | **Buffer pH 5.5** |
|---|---|
| 20mM Hepes pH 7.4 | 10mM MES pH 5.5 |
| 100mM KCl | 100mM KCl |

PLM experiments on PFN, instead, were performed in 20mM Hepes pH 7.4, 100mM KCl, 0.1mM $CaCl_2$.

Current recordings were performed by Axonpatch 200 (Axon Instruments) and data were acquired by a PC equipped with a Digidata A/D converter (Axon Instruments).

### 3.1.9. Atomic Force Microscope

AFM experiments were performed in the same condition of PLM analysis in order to reproduce the same pore-forming activity, so the buffers used were the same describe above. AFM experiments were performed using a Cypher instruments(Asylum Research).

# 3.2. Methods

## 3.2.1. LLO expression and purification

Listeriolysin O gene is inserted in two different plasmids: at the beginning we used pET-8c (named also pET-3d) vector for LLO wt and the two double mutants (LLO A318C-L334C and Q216C-Y406C), then we decided to insert LLO gene on pPROEX-HTb plasmid. The second plasmid was chosen because it turned out that we lost a lot of protein during protein purification steps (decreasing salt concentration). In order to obtain a better purification yield, we decided to eliminate the cation-exhange step by changing the plasmid to pPROEX-HTb, which contains a TEV restriction site between His-tag sequence and LLO sequence. This change allowed us to purify the protein with two passages on Ni-NTA column: the first to select Hi-Tag LLO and the second to elute LLO without His-tag.

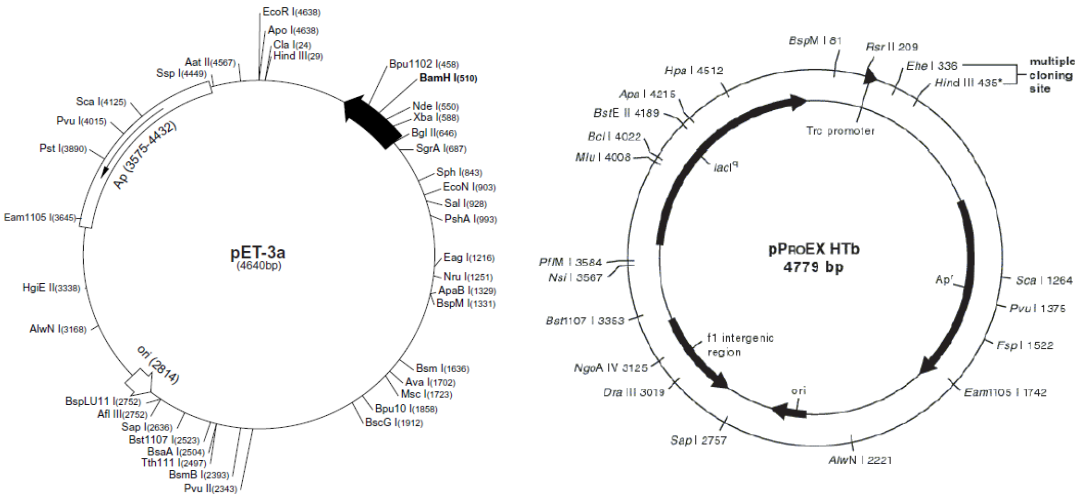


**Figure 3.1 Maps of the two plasmids used for LLO expression in bacteria.**

Plasmid pET-8c, corresponding to pET-3d, is derived from pET-3a with the following changes: 2bp less at each site beyond Bam HI at 510 position and Nco I site instead of Nde I, for a total plasmid length of 4637bp. Plasmid pPROEX HTb is longer, 4779bp, and in the multiple cloning site is present a His-Tag sequence with TEV protease site (see Figure 3.2).

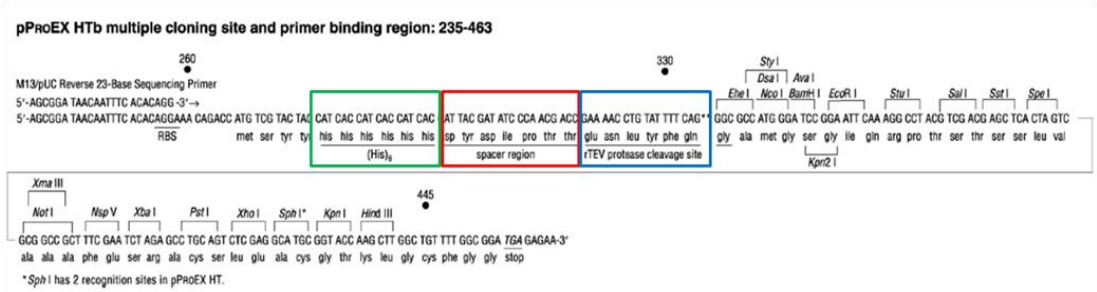


**Figure 3.2 Multiple cloning site of pPROEX HTb.**

$His_6$-Tag (green), a spacer region (red) and a rTEV protease cleavage site (blue) before the restriction sites for DNA cloning.

For protein expression, *E.coli* cells (BL21 pLysS (DE3) strain) were transformed with 150ng/uL of LLO DNA (wild-type or mutants) by thermal shock. LLO containing bacteria were then plated and grown overnight at 37°C on antibiotic (ampicillin and chloramphenicol) LB medium plate. From a selected colony, bacterial cells were cultured on TB medium broth and LLO expression was induced by IPTG addition (0.5mM).

After LLO overnight expression, bacteria were lysed and LLO was purified through two diverse chromatographic passages: affinity column (Ni-NTA) and cation-exchange column.

LLO protein was eluted from Ni-NTA column by passing 300mM Imidazole solution; from CEC column, LLO was eluted at around 35% of salt concentration (i.e. 320mM NaCl). This procedure is valid for wt LLO and the two double mutants produced on pET8c; instead for the H311 mutants expressed on pProEXb plasmid, the purification steps were the following: Ni-NTA column, overnight His-Tag cleavage with TEV protease, second Ni-NTA column to separate the cleaved LLO from the uncleaved one. All the purification chromatographic steps were performed by AKTA-FPLC system (Pharmacia, GE Healthcare).

### 3.2.2. Polyacrylamide gel electrophoresis

All samples from the preparation and purification steps were controlled on a SDS-PAGE gel (4-12% acrylamide) [Gel precast (NuPAGE Novex Tris-Acetate Mini gels, Invitrogen)] Gels were run for 40 min at 200V, 125mA, then stained with NuPAGE staining dye to visualize protein bands. LLO protein was concentrated and the final concentration was measured at 280nm.

Concentration (c) was estimated from the absorbance (A) through the Lambert-Beer equation

$$c\ (M) = A / (\varepsilon l) \qquad \textbf{Equation 1}$$

where l=1cm, ε=1,315 $M^{-1}$ $cm^{-1}$.

### 3.2.3. Hemolytic assay

Red blood cells (RBCs) are washed three times with Assay Buffer (see Materials 2.1.5) by a 5 min centrifugation step at 2100 rpm at 4°C. Once RBCs are cleaned from other cells and from free hemoglobin, the erythrocyte suspension is diluted several times in order to obtain an apparent OD value of 0.1 at 608nm wavelength. LLO activity is tested at different concentrations (2x serial dilution starting from 10nM) and the kinetics of lyses is followed for 30-45 minutes. In the case of the double mutants, the samples tested are proteins as they come out from the purification step, reduced protein and oxidized one. Hemolytic activity of each sample is calculated as following:

$$\%\ HA = (OD_{start}-OD_{end})/(OD_{start}-OD_{min})*100 \qquad \textbf{Equation 2}$$

where $OD_{start}$ is the OD corresponding to intact RBC sample and $OD_{end}$ is the OD at the end of the assay for each well. $OD_{min}$, means the OD of the complete disruption of RBC, as in the sample with ipotonic solution .

Plotting absorbance versus concentration values, it is possible to estimate the HC50 value, i.e. the LLO concentration that lysates 50% of RBC. This parameter is useful for comparing toxin and mutants activity in different conditions.

### 3.2.4. Liposome preparation

Starting from lipid stock in chloroform (10mg/mL), the desired membrane composition is prepared and mixed into a Round-bottom flask to get a final concentration of 6mg/ml.

After chloroform evaporation, lipids are re-suspend in buffer solution, typically PBS buffer (15mM phosphate buffer, 150mM NaCl, pH 7.4), and vortexed for 1-2 minutes to form multilamellar vesicles (MLVs)

MLVs are subject to six freeze/thaw cycles and then the vesicles are extruded 31 times through a 100nm cut-off membrane in order to obtain unilamellar vesicles (LUVs) homogeneous in dimension. After the extrusion, the dimension of vesicle is controlled by dynamic light scattering (DLS) and stored at 4°C till use.

### 3.2.5. RT-PCR/DSF assay

Differential Scanning Fluorimetry (DSF) is an easy method to monitor protein thermal unfolding in different buffer conditions (Niesen et al., 2007).

SYPRO Orange fluorescent dye (Sigma # S 5692, 5000X concentrated solution in 100% DMSO) binds to the hydrophobic part of proteins which are normally not exposed to water medium, so it is specific to follow protein denaturation and aggregation processes. DSF is usually performed by a RT-PCR instrument.

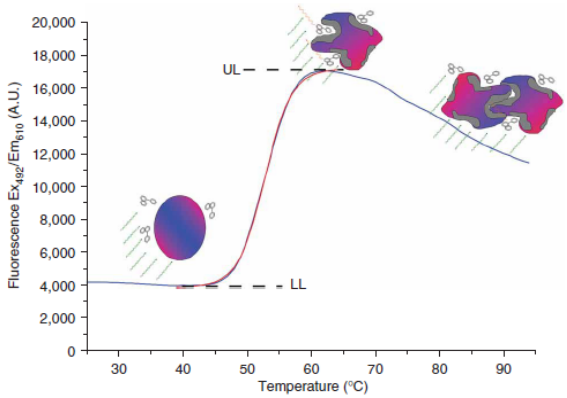


**Figure 3.3 Typical DSF curve.**

In the first part (low fluorescence) protein tested is still folded and SYPRO Orange is free in solution; increasing the temperature the protein starts to unfold and selectively binds SYPRO Orange dye. Once the protein is completely unfolded, it starts to aggregate causing a decrease in the fluorescence signal (last decreasing part of the curve).

The total volume of the samples is 20 µl for each well; SYPRO Orange has to be diluted 1:5000 and protein has to be in 1-10 µM concentration range. In our case, best LLO concentrations tested are 2.5-5 µM. SYPRO Orange is excited at 483 nm and the emitted fluorescence is collected at 610 nm. Thermal protocol consists on a first step of 5 min incubation at 20°C, then a step of gradual temperature increase from 20°C to 85°C with ramp rate of 0.02 °C/s (1,2 °C/min), and finally a third step of cooling to 20°C.

The curve 'fluorescence versus temperature' already gives some information and visually reveals differences in protein stability, but this curve is very sensitive to environmental variation (i.e. protein and/or dye amount), so in order to obtain a quantitative value it is

better to convert this curve in its first negative derivative. The obtained curve has a plateau profile before and after a single negative peak (if the sample/measurement is good). The peak temperature value, Tm, corresponds to the inflection point of the curve between LL and UL in Figure 3.3 and it is independent from the curve slope and the fluorescent levels of the sample (i.e. environmental differences).

### 3.2.6. Planar lipid membrane (PLM)

Solvent-free PLM were prepared as described by Dalla Serra and Menestrina, 2000.
Two teflon chambers (2ml each) are separated by a 25µm-thick teflom septum in which is made a hole of around 150 µm in diameter. Both chambers are filled with buffer and a planar membrane is formed on the septum hole. Lipid mixture is added from a 5mg/ml stock in pentane. As reported in the Materials paragraph, the solution used contains 100mM of salt (KCl), 20mM Hepes pH 7.4 or 10mM MES pH 5.5 and the experiments are performed in symmetric conditions.
PFO and LLO were added at nM concentrations on the *cis* chamber (*cis* chamber is where the electrical potential is applied, while *trans* chamber is grounded). Concerning the experiments with PFN, I added 100ng/ml on the *cis* side containing 20mM Hepes pH 7.4, 100mM KCl, 0.1mM $CaCl_2$. A constant voltage, typically +40mV, was applied to the system and the current across the membrane was recorded by Axon instruments (see specification above). From the recorded current data, it is possible to calculate the conductance of the pore (G) as shown in the equation 3,

$$\mathbf{G(nS) = I(pA)/V(mV)} \qquad \textbf{Equation 3}$$

where **I** is the current through the pore and **V** is the applied voltage. G values can be used to estimate the dimension of the pores. In fact assuming the pore as a cylinder water filled this parameter is proportional to pore area as shown in equation 4,

$$\mathbf{G(nS) = \sigma * A(nm^2)/L(nm)} \qquad \textbf{Equation 4}$$

Where **A** is the area of the pore, **L** is the length of the pore and **σ** is the conductance of the buffer used. All the experiments were done in 100mM KCl buffers, which has **σ=1.2nS/nm.** From equation 4, it is easy to get a rough estimate of the pore diameter, assuming it has circular section.

### 3.2.7. Bilayer preparation on mica

**Material:** mica attached on metal support, Teflon chamber, vacuum grease.

First, mica is freshly cleaved to obtain a smooth surface, then a teflon chamber is stuck on the external metal support with vacuum grease.
Liposome preparation (6mg/ml) is diluted in MilliQ water (final volume of 100µl) at the final concentration of 1.5-2 mg/ml in presence or absence of calcium.
Calcium chloride is used to facilitate the supported bilayer formation: the calcium concentration used changes on the basis of increasing cholesterol amount in the membrane. For POPC membrane (bilayer used with PFN), $Ca^{2+}$ concentration used is 0 or 1mM . For DOPC:CHO 20% (low CHO concentration), $Ca^{2+}$ concentration used is 2mM, instead for POPC:CHO 50% (high CHO concentration) membrane, $Ca^{2+}$ concentration needed to obtain a good bilayer was 4mM.
The liposome suspension is incubated on the mica surface for 1 hour at Room Temperature. After the incubation time, excess of liposome that is not attach on the mica, is washed away simply adding a large volume of the protein buffer solution on the sample. Typically for PFN experiments, we washed three times the sample with 1ml of PFN buffer (20mM Hepes, 100mM KCl, pH 7.4), and then we removed part of the washing solution until reaching a typical volume of 150µl. 1µg of PFN is added and the protein is incubated for 15 minutes at room temperature. The unbound protein was then washed away with the same PFN buffer used before (1ml and then the sample is placed into a Petri dish and wash with a large volume (~100ml of buffer). After the washing step, teflon chamber is removed, and the sample is analyzed by AFM. With regard to CDC (PFO and LLO) experiments, the washing procedure was changed. We improved the perfusion procedure by adapting an automatic perfusion system (sp260p syringe pump, WPI) with a homemade support for the two thin tubes for buffer insertion and withdrawal.

Washing steps were performed as follows:

- PFO: 2.5mL of buffer pH 7.4 at 0.5mL/min between liposome and protein incubation, and after protein incubation a final wash with 0.5 mL at 0.1mL/min.
- LLO: 0.5mL of buffer pH7.4 and 2mL of buffer pH 5.5 at 0.5mL/min between protein addition, and after incubation, 0.5mL buffer pH 5.5 at 0.1mL/min.

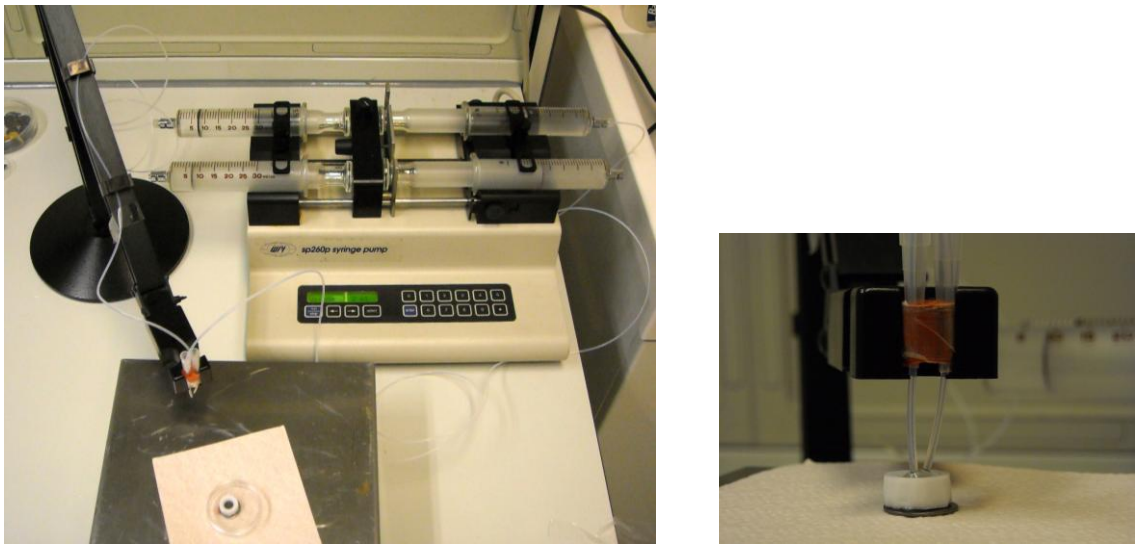

**Figure 3.4 Homemade perfusion system based on automatic sp260p syringe pump (WPI)**

After sample washing, the Teflon ring was taken away and the samples, containing a drop of about 100µl of buffer, were visualized by the microscope in closed loop. The images were performed in AC mode with a Cypher AFM (Asylum Research) equipped with a droplet cantilever holder.

The cantilevers used are the silicon nitride TR400PSA (from Olympus) with a pyramidal shape and a radius of 15 nm. We always acquired images with the cantilever smaller tip (nominal stiffness of 0,08 N/m) driven approximately at 7 kHz.

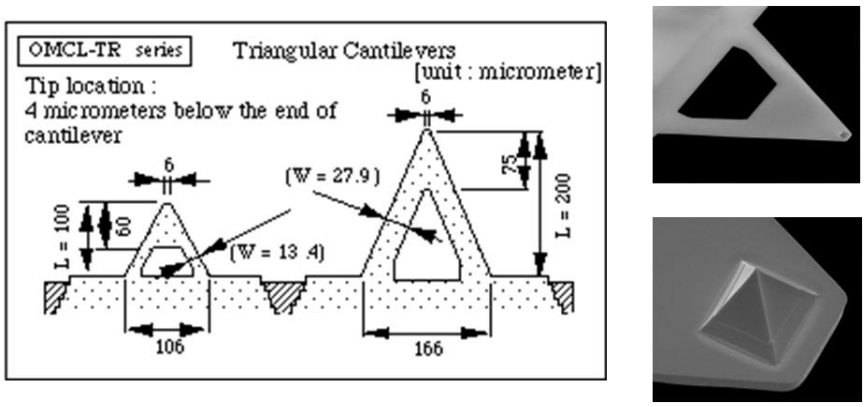


**Figure 3.5 Cantilever shape and properties.**

On the left, a scheme of TR400PSA cantilever reporting the dimension of the tips. On the right, two images: cantilever shape (upper image) and tip shape (bottom image).

Image acquisition was performed by AFM software Igor Pro 6.12A (WaveMetrics, ZDA) and Gwyddion 2.24.

# 4. Results and Discussion

## 4.1. Perfringolysin O conductance at pH 7.4

Nelson et al., 2007 demonstrated that membrane lipids' composition (sterol and phospholipid components) has a critical role on PFO binding affinity and that protein binding is also influenced by the environmental pH. Their major conclusions were that: i) less cholesterol is needed for PFO binding/activity at acidic pH, ii) a free OH group in the β-OH cholesterol configuration is strictly necessary for PFO recognition and interaction, and iii) the head and the acyl chain moiety of phospholipids modulate PFO monomers binding to the membrane.

Flanagan et al., 2009 focused their attention on the influence of the acyl chain order on PFO binding and oligomerization. In particular, they demonstrated that, in presence of more disordered acyl chain phospholipids (i.e. more unsaturated bonds), the cholesterol amount necessary for PFO oligomerization is lower. So, changing the sterol to phospholipid ratio and the degree of acyl chain saturation it is possible to modulate PFO binding and probably its pore-forming activity. In order to investigate the correlation between binding modulation and pore-forming ability, and the pore structure, we decided to test PFO activity on four different membrane compositions and at two pHs with electrophysiological measurements on Planar Lipid Membranes. These results will be then compared with AFM images of PFO adsorbed on similar supported lipid membranes.

Starting from the published data, we decided to screen PFO activity on four different lipid compositions: two membranes with high and two with low PFO binding affinities. Our experiments showed a very complex scenario of PFO pore-forming ability. In Figure 4.1, I report some characteristic and representative examples of PFO lytic activity at pH 7.4.

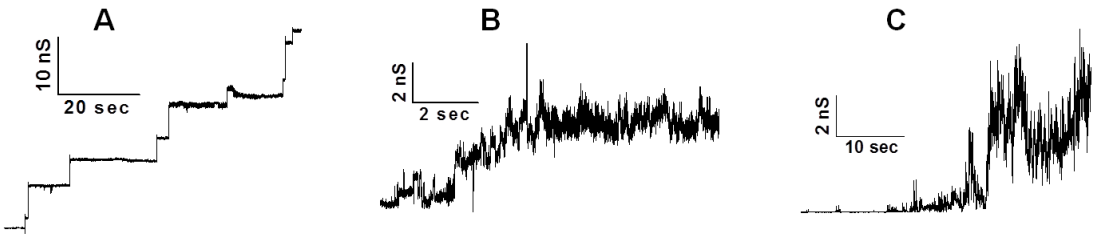


**Figure 4.1 Examples of PFO traces at pH 7.4**

A) Step-like increase: well define pore visible on POPC:CHO 1:1 membrane; B) very noisy small step-like increase: pores visible on DOPC:CHO 1:1 and POPC:CHO 4:1; C) unresolved current increase: lytic activity on DOPC:CHO 4:1. Note the different scales in the panels.

As visible in the examples reported, PFO can produce different features of ionic conductive paths through the lipid membrane. In fact, as I will discuss later on, we can detect defined, even though broadly distributed, single step increases in membrane conductance, as well as not resolved and noisy current increases. The noise on the current trace is also an important fingerprint that can reveal information on the pore architecture. As reported in Praper et al., (2011a) for perforin, stable pores could be correlated with complete and purely proteic pores, where inter-molecular bindings render the complex thermodynamically stable; instead the presence of toroidal pores with a proteolipidic composition (where the pore walls are constituted by both protein and lipid) can be correlated with the more noisy openings. In Table 4.1, I summarized the different PFO pore-forming characteristics on the basis of membrane composition.

| PFO @pH 7.4 | n° pores considered | G value (nS) | Pores description |
|---|---|---|---|
| **POPC:CHO 1:1** | 425 | 0.1<G<30 | well defined and stable pores with step-like current increases, only few unresolved current increases |
| **DOPC:CHO 1:1** | 31 | < 5 | step-like increase with small conductance, some noise, instability of the pore |
| **POPC:CHO 4:1** | 61 | < 5 | small step-like increases very noisy, some unresolved increments in current and much opening and closure |
| **DOPC:CHO 4:1** | 0 | N.D. | pore activity very noisy, increase in current without defined step-like pores |

**Table 4.1 Summary of PFO results at pH 7.4.**

In the table, PFO pores divided by membrane composition; numbers, conductances range and a brief description of ionic current characteristics are reported. N.D. non detected

The different pore activities are membrane-dependent and linked to PFO binding affinity in that particular condition. In particular, more affinity for the bilayer leads to more defined pores and also more pores per fixed experimental time and similar PFO concentration. In the next paragraph, more detailed descriptions of PFO lytic activity are presented.

### 4.1.1. High cholesterol-containing membrane

The first membrane screened was POPC:CHO 1:1 mol, similar to that reported in Sheppard et al. (2000), which can be considered as a reference for setting all experimental conditions. In this membrane composition, PFO formed very defined and stable large pores with heterogeneous conductances (G), as reported in Figure 4.2, where representative current traces and the cumulative histogram are reported.

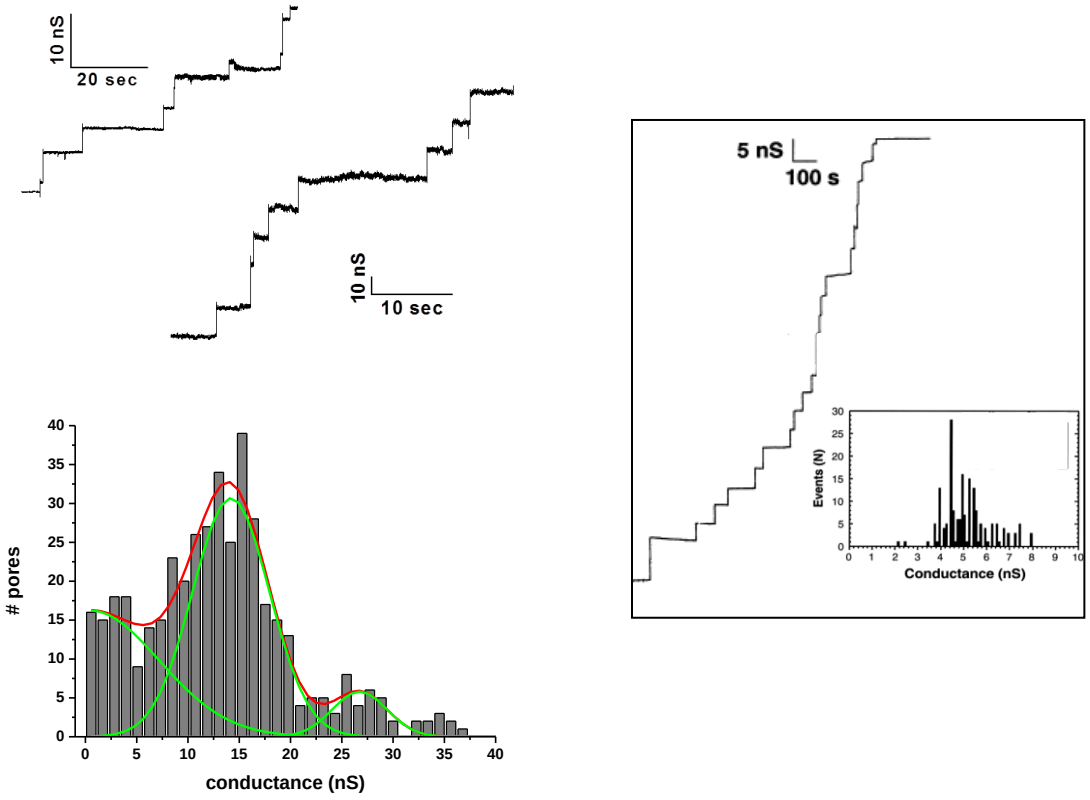


**Figure 4.2 PFO activity on POPC:CHO 1:1 membrane.**

On the left upper panel, two representative examples of current traces recorded at +40mV. On the bottom, a cumulative histogram with conductance values of 425 pores. PFO concentration used in the experiments was from 12 to 48 nM. Right panel: PFO behavior adapted from what reported in Shepard et al. (2000) for comparison.

In these conditions PFO can induce a typical step-like increase in membrane current. The single channel conductance values we measured are higher than those reported by Shepard (e.g. between 4 and 6 nS), and this could be related to differences in membrane preparation (they used painted bilayer which may be thicker and more fluid) and protein used (they reported experiments for the PFO mutant C459A). From my conductance histogram, it is

possible to support the presence of at least two channel populations: "small" pores with a G smaller than 5nS and a broad population of "big" pores with G centered at 14.2 ± 3.7nS which corresponds to an estimated radius of 6.9 nm (see Eq.4).

In the second membrane with high cholesterol composition, we used DOPC lipid (1,2-dioleoyl-*sn*-glycero-3-phosphocholine) that has two 18C chains each containing an unsaturated bond at carbon C9. This lipid composition caused some difficulties in getting stable bilayers, which also, after formation, do break more easily. Anyway we succeeded in getting at least few experiments.

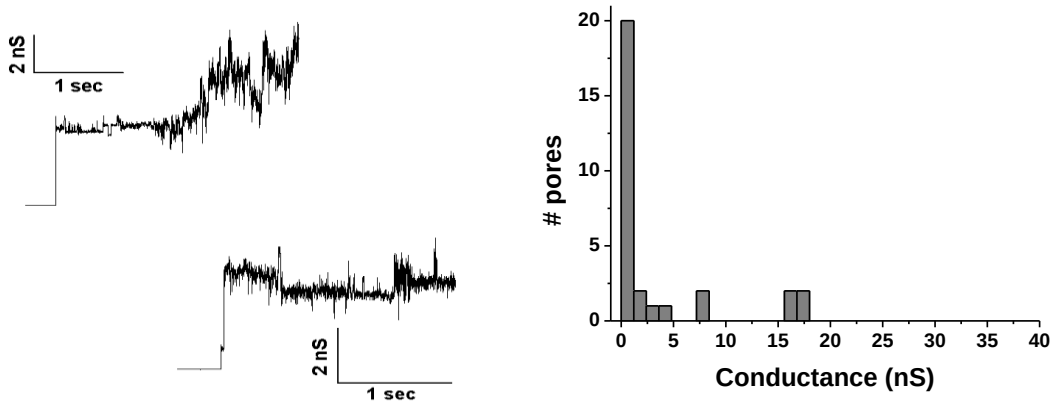


**Figure 4.3 PFO activity on DOPC:CHO 1:1 membrane.**

On the left panel, two examples of current traces recorded at +40mV. On the right, conductance cumulative histogram of 31 pores. PFO concentration used in the experiments was from 12 to 72 nM.

In Figure 4.3 histogram, I summarized all the data I obtained in seventeen different experiments. The pore behavior looks very different from what seen before, even though a careful statistical analysis of pore conductances could not be performed due to the paucity of clear single pore apertures. Big sudden jumps are still present, but much higher noise is clearly visible on top of them. Furthermore, some unresolved current increases are recorded.

### 4.1.2. Low cholesterol-containing membrane

Another important aspect coming from the two papers mentioned before (i.e. Nelson et al., 2007 and Flanagan et al., 2009), was the modulation of PFO binding by cholesterol concentration. In particular, the free accessible cholesterol in membrane (threshold value for binding) varied from phospholipid to phospholipid present and probably affected the pore-forming ability of the protein. In order to determine if PFO, besides complete and fully proteic circles, can induce changes in the membrane structure and produce different pore structures (like arciform toroidal pores) we decided to decrease cholesterol content in both phospholipids used before. The chosen phospholipid:cholesterol ratio was 4:1, composition for which it was reported that PFO poorly binds on POPC while discretely binds on DOPC containing membrane.

On POPC:CHO 4:1, PFO formed smaller pores with G values less than 4 nS. Most of the current steps were very noisy and pores tend to close after some seconds (from 2 sec to 1 min). This pore-forming behavior could be correlated with less stable pore, probably proteo-lipidic one.

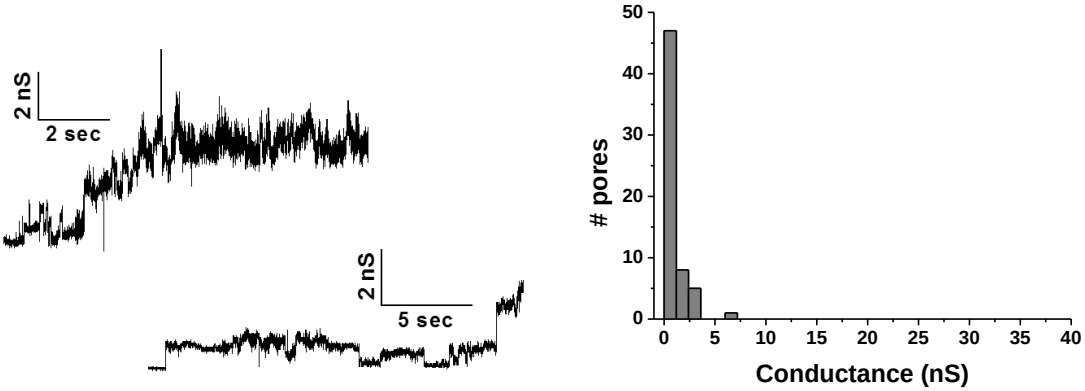


**Figure 4.4 PFO activity on POPC:CHO 4:1 membrane.**

Left panel, some examples of current traces obtained applying +40mV. Right panel, conductance histogram of 61 PFO pores. PFO concentration used in the experiments was comprised from 12 to 48 nM.

Finally, when we tested PFO activity on DOPC:CHO 4:1, we found that it was impossible to detect single step increases in current traces. Noisy and unresolved current changes are the only effect of PFO, as depicted in Figure 4.5. Since a single pore formation, either small or big, is characterized by a sudden and defined current increase, the behavior we

recorded at low cholesterol content should have a different origin. The noise could be correlated to the presence of less stable lesions, which may vary in dimension during time. As suggested by Praper et al., (2011a) this may be compatible with the opening of toroidal arc-shaped pores. We interpreted the unresolved current increases as related to growing arcs in which every additional monomer contributes to modest current increase.

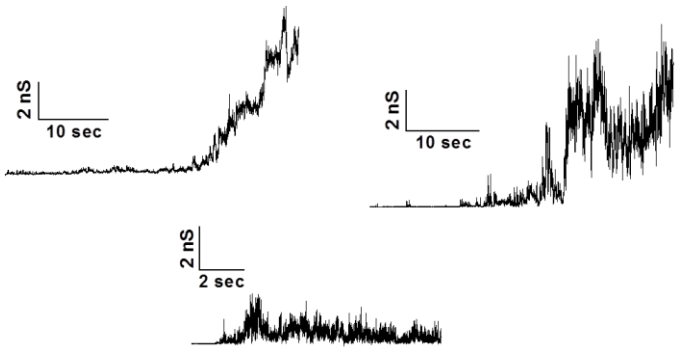


**Figure 4.5 Examples of current traces recorded on DOPC:CHO 4:1 membrane.**

The high noise on the current is a typical feature of low cholesterol containing membrane. PFO concentration used in the experiments is comprised from 12 to 96 nM.

With the effort to rationalize those diverse behaviors, we tried to clusterize the variety of pore-forming abilities obtained. A first separation that could be made was between defined current step-like increases and noisy or not defined current increases (left panel of Figure 4.6). The second analysis could be done on the dimensions of defined step increases. According to the qualitative histograms presented above, we fixed our cut-off at 5nS for separating small pores (G < 5nS), which are probably incomplete rings or arc-shaped pore, from big pores (G > 5nS).

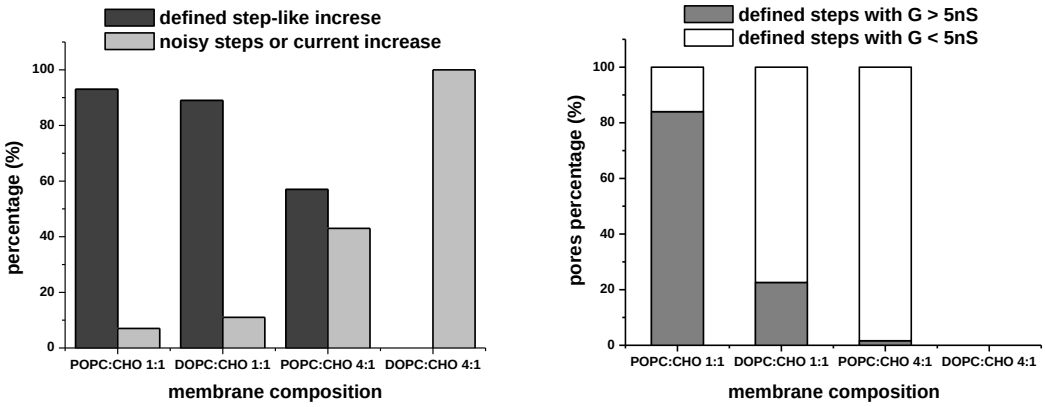


**Figure 4.6 Histogram of defined vs not defined pores and small vs big pores at pH 7.4.**

Left panel, percentage of defined pores and increase openings in every membrane composition. Right panel, separation of the define pores in small (G<5nS) and big pores (G>5nS).

Based on these functional data we speculated that PFO, besides forming barrel stave pores, which are characterized by big, stable and low noise current jumps, could oligomerize to truncated rings in lipid membranes. These arc-shaped structures are active pores with a smaller conductance. The proteolipidic character may be inferred from their lower stability. Those incomplete arcs may grow in size by successive addition of further monomers, and this causes a gradual increase in current, which cannot be resolved in single step-like increments.

More rigid membranes (like POPC/chol) or high cholesterol content favor the appearance of more structured oligomers, either complete or incomplete rings. In fact, bigger pore structures are more abundant at high cholesterol content. This is consistent with the higher PFO binding affinity with membranes rich in cholesterol, which permits a higher amount of toxin immediately available to oligomerize and to form pores, as suggested by Gilbert (2005).

## 4.2. PFO is active at acidic pH 5.1

As mentioned above, besides membrane lipid composition, pH may also modulate PFO-membrane interaction. We decided to study PFO activity at acidic pH for getting indications useful to characterize Listeriolysin O, which works at pH 5.5, and also for catching key players in CDCs mode of action.

Nelson et al. (2007) reported that at acidic pH PFO is able to interact with membrane at lower cholesterol concentration than at neutral pH. So we decided to keep constant the four different membrane compositions and test the pore-forming activity at pH 5.1. In Table 4.2 are summarized the different PFO pore-forming activities on the basis of membrane composition.

| PFO @pH 5.1 | n° pores considered | G value (nS) | Pores description |
|---|---|---|---|
| **POPC:CHO 1:1** | 82 | 0.1<G<16 | well defined and stable pores with step-like current increases,<br>frequent pore opening/closing |
| **DOPC:CHO 1:1** | 23 | < 3 | step-like increase with small conductance,<br>few unresolved current increases |
| **POPC:CHO 4:1** | 101 | 0.1<G<16 | small and big step-like increases,<br>small pores very noisy<br>big pore with frequent opening/closing |
| **DOPC:CHO 4:1** | 40 | 0.1<G<10 | noisy small and medium step-like increase<br>few increments and frequent opening/closing |

**Table 4.2 Summary of PFO results at pH 5.1.**

In the table, PFO pores divided by membrane composition; numbers, conductances range and a brief description of ionic current characteristics are reported.

### 4.2.1. High cholesterol-containing membrane

On POPC:CHO 1:1 membrane, we observed the same kind of well defined step-like increases already seen at neutral pH meaning that also in this condition we are promoting the formation of very stable pore structures. As expected we also found that at acidic pH the protein is more active, in fact the same total current can be obtained with less than half of the protein used at neutral pH. This finding can be due to a partial unfolding of PFO

monomer structure that facilitates protein insertion or to a higher binding affinity of PFO to the membrane at acidic pH, as reported by Nelson et al., 2007.

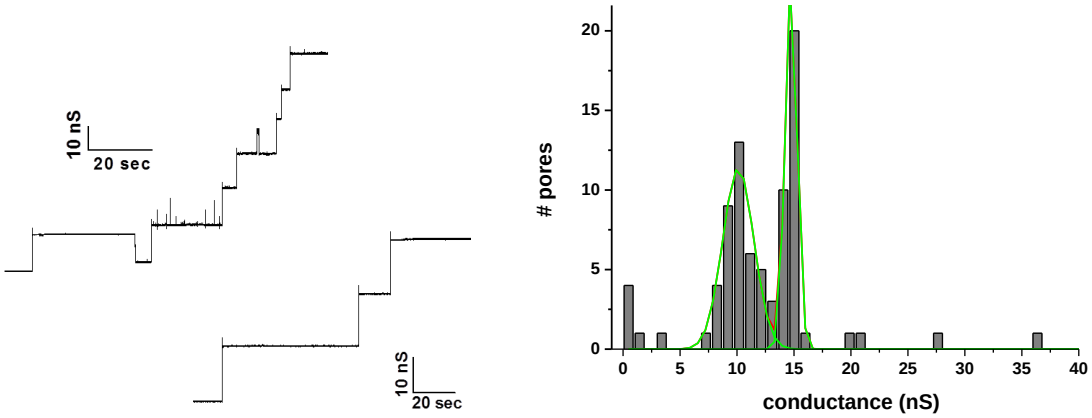


**Figure 4.7 PFO activity on POPC:CHO 1:1 membrane.**

On the left, two examples of current traces recorded at +40mV. PFO concentration used in the experiments was from 7.2nM to 12nM. On the right, conductance histogram of 82 pores.

From the cumulative histogram, it is possible to individuate two separated pore populations. A medium-sized pores with a G mean value of 10.1 ± 1.4nS and a big-sized pores of G mean value of 14.7 ± 0.5nS. Small channels (< 5nS) are very few.

DOPC:CHO 1:1 membranes are very unstable also at pH 5.1 and easily breaks after one or two PFO pores are formed. As reported in Figure 4.8 less PFO is necessary for increasing membrane current. Besides the presence of few pores classified as "big" (with conductance of 15 nS), the majority of the pores are small and noisy.

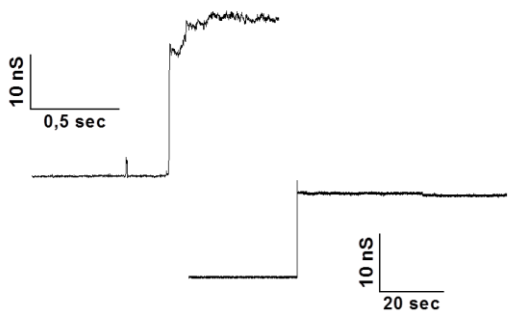


**Figure 4.8 PFO activity on DOPC:CHO 1:1 membrane.**

Two pores recorded at +40mV. PFO concentration used was 12nM, in experiments with one-two pores and membrane broken and 8nM in experiments containing more pores. 23 pores visualized.

### 4.2.2. Low cholesterol-containing membrane

On POPC:CHO 4:1 membrane, PFO formed very heterogeneous pores and surprisingly, in comparison with pH 7.4, the pores appear as well defined step-like increases (big or small) but also opening and closing events are present on the pore levels that reveal high instability of the lytic pore formed. In this particular condition, PFO was able to form several kinds of pore that support our idea of a not unique mechanism of pore formation.

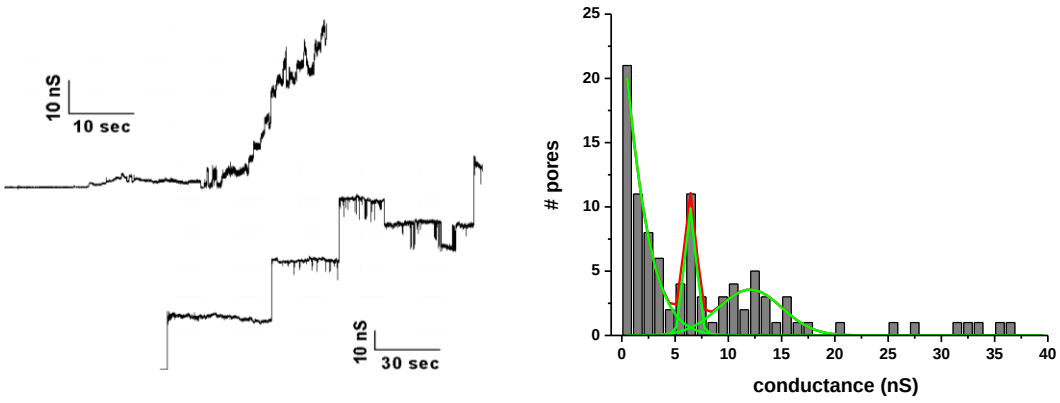


**Figure 4.9 PFO activity on POPC:CHO 4:1 membrane**.

On the left panel, some traces of pores opening recorded at +40mV. PFO concentration used was from 7.2nM to 24nM. **.** On the right panel, conductance histogram of 101 pores.

In my opinion, the most interesting results obtained during this screening was the one obtained on DOPC:CHO 4:1 membrane and pH 5.1. Working at acidic condition, PFO seems to be more active, or at least more able to form better structured pores than at neutral pH. In fact, at pH 7.4 it is almost impossible to see step-like increase, even small, in the current traces as if PFO interacts and destabilizes the bilayer making very unstable pores. At acidic pH, instead, current steps are easily identified.

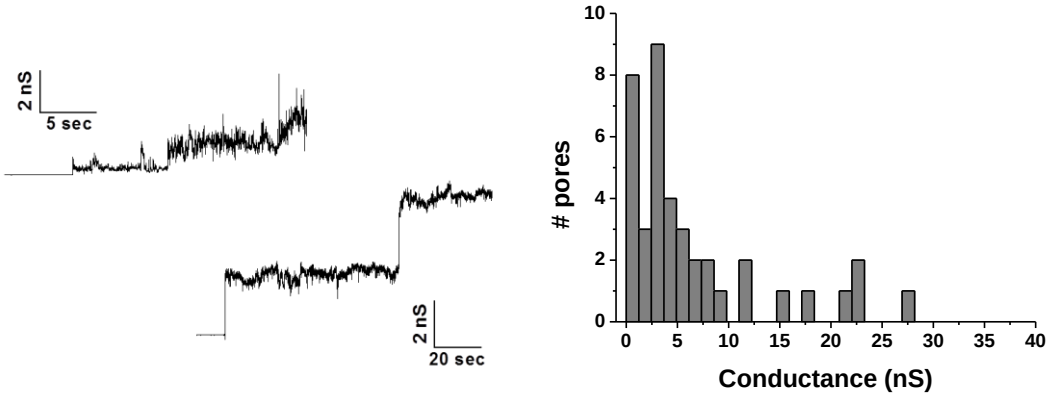


**Figure 4.10 PFO activity on DOPC:CHO 4:1 membrane.**

On the left panel, pores of different size recorded at +40mV. On the right, panel conductance histogram of 40 pores. PFO concentration used was from 12nM to 24nM.

As for pH 7.4 data, we analyzed the pores by dividing them into the two groups of defined and not defined pores and then, inside the defined ones, we classified the pores into small and big ones.

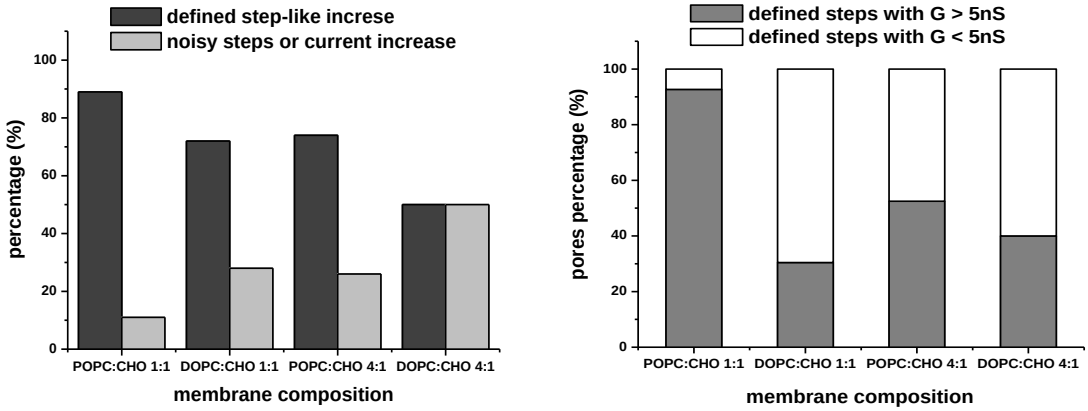


**Figure 4.11 Histogram of define vs not define pores and small vs big pores at pH 5.1.**

Left panel, percentage of define pores and increase openings in every membrane composition. Right panel, separation of the define pores in small (G<5nS) and big pores (G>5nS).

The low pH increases the presence of defined current increases, already at low cholesterol content. This effect is particularly evident with the more fluid DOPC:CHO 4:1 membrane, if one compares the similar conditions at neutral pH, and it is compatible with a higher availability of bound PFO experienced at low pH (Nelson et al., 2007).

## 4.3. LLO pore-forming activity at pH 5.5

Listeriolysin O (LLO) acts at the endosomal membrane level in order to disrupt and facilitate *L. monocitogenes* escape from the vesicle compartment. For that reason, this toxin shows an optimum lytic ability at acidic pH, which is the typical internal pH of the endosomal-phagosomal vesicles (estimated to be around 5.5). This LLO property is a unique feature among all the CDCs that usually act at neutral pH. LLO, instead, is mostly produced and released by bacteria in the phagosomal acidic environment as active monomeric protein. Once LLO disrupts the vesicle, the toxin is released into the cytosol and starts a denaturing process due to the higher pH (Schuerch et al., 2005, and Hamon et al., 2012). The modulation of LLO activity is a crucial point for bacteria pathogenesis: it allows to avoid the lysis of host cell and the recruitment of immune response actors that will block the progression of *Listeria* infection (survival and replication). In Bavdek et al., 2007, however, the authors reported that, at room temperature, LLO shows some lytic activity at neutral pH and that this low pore-forming ability can be restored enhancing the sterol percentage inside the lipid bilayer. As we did for PFO analysis, we decided to characterized LLO activity on four different membrane composition and at two pHs.

| LLO pH 5.5 | n° pores considered | G value (nS) | Pores description |
|---|---|---|---|
| **POPC:CHO 1:1** | 276 | 0.1<G<25 | very well defined and stable step-like pores,few current increments on pore step |
| **DOPC:CHO 1:1** | N.D. | N.D. | pore opening with subsequentmembrane disruption |
| **POPC:CHO 4:1** | 41 | 2<G<20 | medium and big step-like increase, frequent opening/closure |
| **DOPC:CHO 4:1** | 125 | <6 | increment in current with few small defined step-like pores (very noisy) |

**Table 4.3 Summary of LLO results at pH 5.5.**

In the table, PFO pores divided by membrane composition; numbers, conductances range and a brief description is reported. N.D. pores not detected

### 4.3.1. High cholesterol-containing membrane

Similarly to PFO, in POPC:CHO 1:1 membrane LLO shows well defined step-like increases in membrane current, suggesting the formation of structured and stable pores.

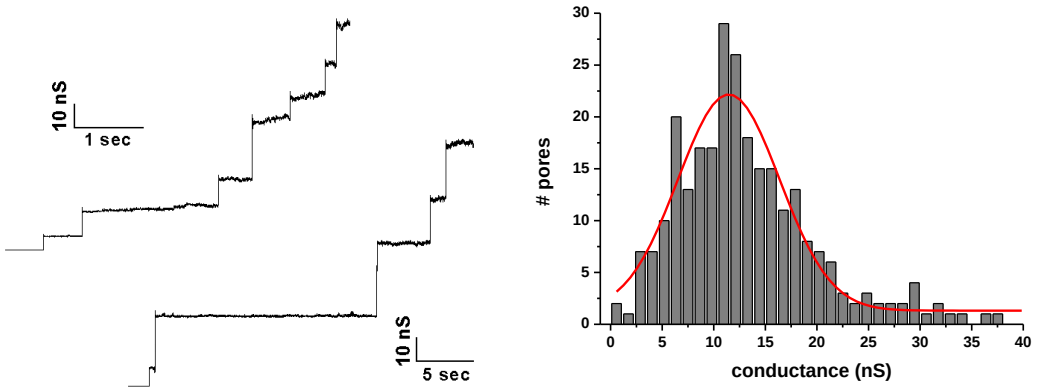


**Figure 4.12 LLO activity on POPC:CHO 1:1 membrane.**

On the right, I reported some current traces of well defined pore openings, typical pore-formation at +40mV. The histogram on the left shows the conductance of 276 pores. LLO concentration was 5-10nM.

LLO pores conductance was analyzed and reported in a cumulative histogram. The broadly distributed values fall in the range between 5 and 20 nS with a mean G value of 11.8 ± 4.8 nS which corresponds to an estimated radius of 6.1 nm (see Eq.4).

As mentioned before , DOPC:CHO 1:1 membranes are very difficult and time consuming to be obtained. Moreover, the addition of LLO to a stable bilayer rapidly breaks the membrane as if the interaction of LLO with this particular membrane is strong enough to completely destabilize the bilayer structure. The few current traces obtained were not significant and, unfortunately, for LLO pores I could not make any kind of analysis.

### 4.3.2. Low cholesterol-containing membrane

Then, we tested the lower sterol concentration (20%) in presence of the POPC and DOPC. On POPC:CHO 4:1 membrane, LLO forms pores very similar to those obtained at higher cholesterol content, both for dimension and step-like opening with an average G value of 12.9 ± 2.9 nS. This is a difference between the two CDCs functionality: LLO seems to be

less influenced than PFO (at its optimal pH 7.4) by the limited cholesterol presence in POPC bilayer.

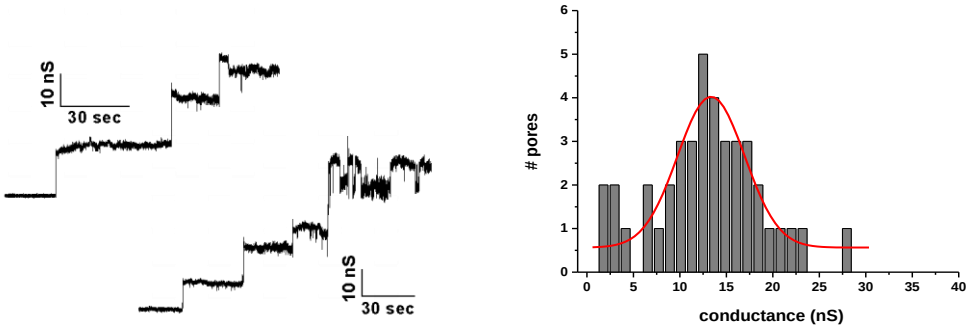


**Figure 4.13 LLO activity on POPC:CHO 4:1 membrane.**

In the left panel, some traces recorded at +40mV. The histogram in the right panel shows the conductance of 41 pores. LLO concentration used was 5-10 nM.

On DOPC:CHO 4:1, most of LLO pores are small and very noisy, as visible in Figure 4.14.

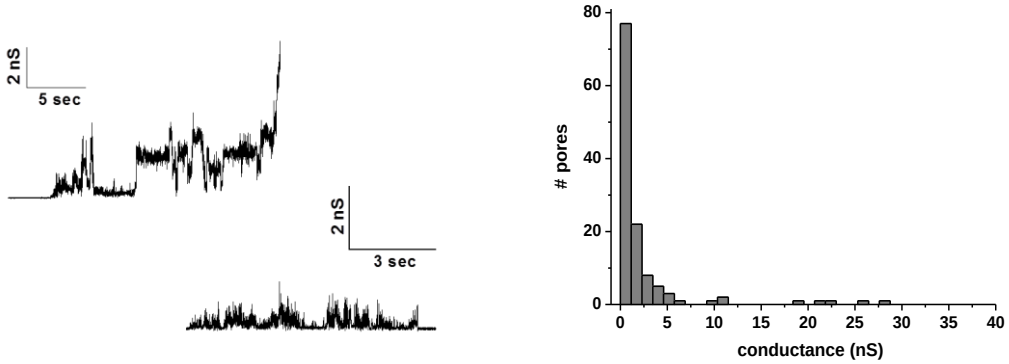


**Figure 4.14 LLO activity on DOPC:CHO 4:1 membrane.**

The histogram in the right panel shows the conductance of 125 pores. On the left, some traces of pore-forming activity at +40mV.

The obtained conductance heterogeneity can reflect the formation of diverse pore structures in the membrane. The noisy traces also suggest the formation of dynamic and instable lesions. Our general hypothesis is that LLO binds and oligomerizes on the membrane until there is the energy sufficient to penetrate the membrane and punch a hole into the bilayer, both in ring-shaped or in arc-shaped configuration, depending on the toxin availability on the membrane which influences the speed of oligomer growing before membrane penetration. Furthermore, incomplete and conducting rings can continue to

grow in dimension towards annular structure completion, and this may be related to the recorded unresolved increases in ionic current.

The same approach used with PFO (two classifications related to defined or not pores and small vs big pores)was applied with LLO pores at pH 5.5 (Figure 4.15).

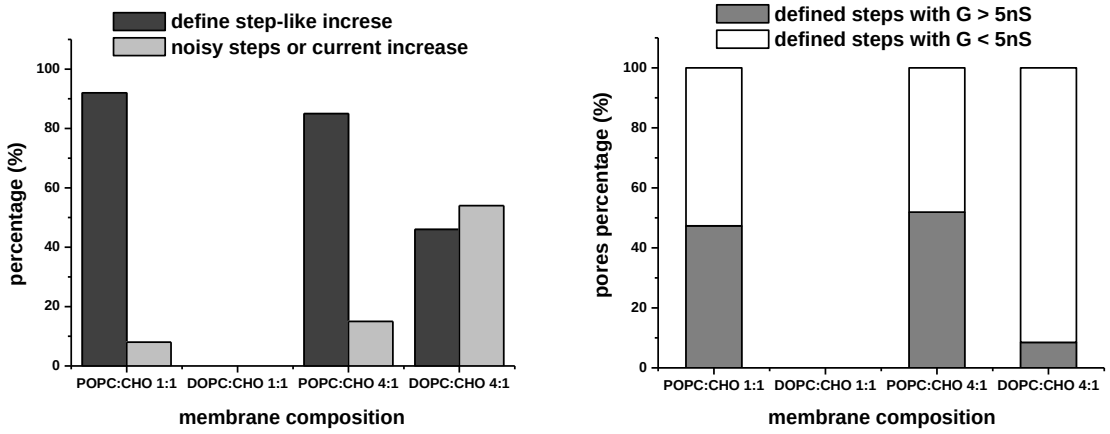


**Figure 4.15 Histogram of LLO defined vs not defined pores and small vs big pores at pH 5.5.**

Left panel, percentage of defined pores and unresolved increases in current for the different membrane compositions tested. Right panel, normalized amount of appearance of defined small (G<5nS) and big pores (G>5nS).

From our classifications, it is clear that LLO formed more defined and bigger pores in POPC:CHO 1:1 membrane, probably due to the higher binding affinity for that particular membrane composition. Lowering cholesterol amount, LLO produced less stable and smaller pores compatible with proteolipidic structures.

## 4.4. *LLO 'low' activity at pH 7.4*

As already mentioned, it was demonstrated that LLO is inactivated at neutral cytosolic pH of the host cell. Many papers, however, reported a binding and lytic activity of LLO at neutral pH, especially in presence of a high cholesterol-containing membrane and temperature under 30°C. These published data are the starting point for our investigations at pH 7.4. In the following table, the results we got for this characterization are summarized by number of step-like pores, dimension and aspect.

| LLO pH 7.4 | n° pores considered | G value (nS) | Pores description |
|---|---|---|---|
| **POPC:CHO 1:1** | 150 | 1<G<16 | Defined step-like pores but noisy, few opening/closure events |
| **DOPC:CHO 1:1** | N.D. | N.D. | small (and few big) step-like increase little current increase on pore opening |
| **POPC:CHO 4:1** | 79 | 0.1<G<12 | step-like pores very noisy and with some instability in current level |
| **DOPC:CHO 4:1** | 47 | < 6 | noisy small and medium step-like increase few increments and frequent open/close |

**Table 4.4 Summary of LLO results at pH 5.5.**

In the table, LLO pores divided by membrane composition; numbers, conductances range and a brief description is reported. N.D. pores not detected

### 4.4.1. High cholesterol-containing membrane

LLO formed well-defined and stable pores but with smaller conductance values if compared with those recorded at pH 5.5. The cumulative histogram shows a mean conductance of 5.8 ± 1.6 nS. Since the noise of current traces is smaller than in other conditions tested, we are wondering if LLO can form smaller ring pores at this pH or if the arc-shaped pores can be more stable (e.g. to be related to a different membrane rigidity).

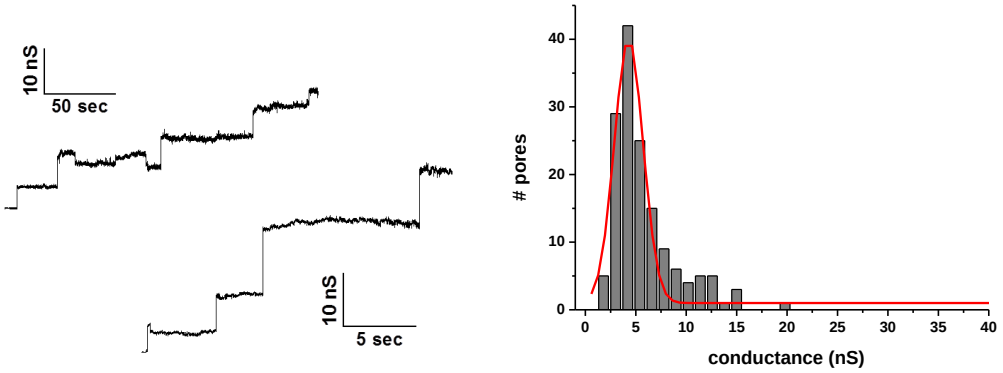


**Figure 4.16 LLO activity on POPC:CHO 1:1 membrane.**

On the left panel, some traces of pore openings at +40mV. On the right panel, conductance histogram of 150 pores.

## 4.4.2. Low cholesterol-containing membrane

On POPC:CHO 4:1, we obtained similar pore-forming activities as in presence of POPC:CHO 1:1 mixture. The step-like increase is clearly predominant and the dimensions are very similar (G mean value of 4.8 ± 2 nS). Even at this pH, LLO seems to be less sensitive than PFO to the decreased sterol amount.

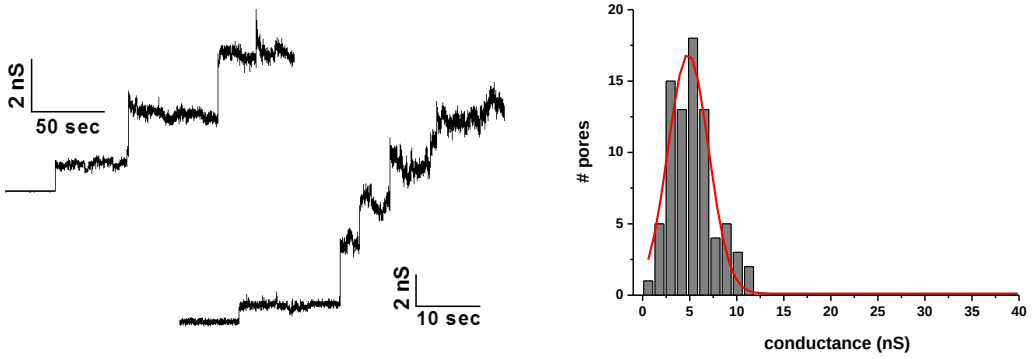


**Figure 4.17 LLO activity on POPC:CHO 4:1 membrane.**

The histogram in the right panel shows the conductance of 79 pores. On the left, some traces of pore formation at +40mV.

Finally, on DOPC:CHO 4:1 composition, LLO forms pores very heterogeneous in size but also in pore formation: step-like increase are present but at the same time not well defined opening are visible. Pores are very noisy and flickering between open and closed state.

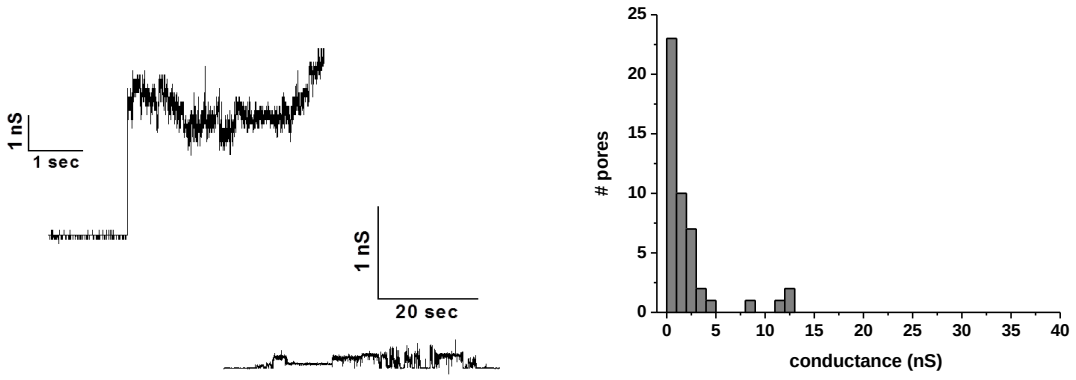


**Figure 4.18 LLO activity on DOPC:CHO 4:1 membrane.**

The histogram, present in the left panel, shows the conductance of 47 pores. On the right, some traces of pore openings at +40mV.

Summarizing LLO results at pH 5.5, we can fit them into our classical classification and report the well defined pores (ring structures) versus not defined ones (arcs configuration) leading to a primary understanding of the different pore-forming abilities on diverse membrane compositions. Also the dimension of the pores is taken into account and reflects LLO lower sensitivity to sterol concentration on POPC-containing membrane.

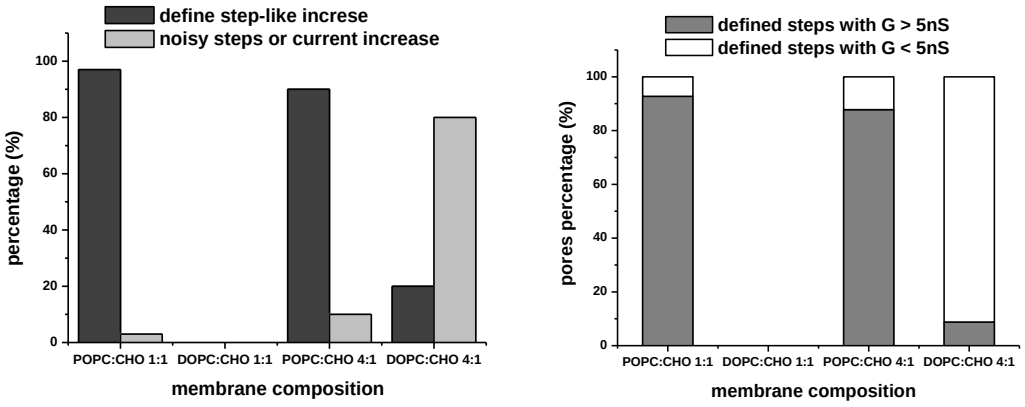


**Figure 4.19 Histogram of LLO defined vs not defined pores and small vs big pores at pH 5.5.**

Left panel, percentage of defined pores and unresolved increases in current for the different membrane compositions tested. Right panel, normalized amount of appearance of defined small (G<5nS) and big pores (G>5nS).

The general behavior described above for PFO and LLO at the two pHs supports the importance of cholesterol presence for improving toxin binding and the formation of more stable and bigger pores. Also for LLO the binding ability is reduced at neutral pH, as reported from the lower amount of defined openings in DOPC:CHO membranes. The fact that at neutral pH LLO pores have a smaller conductance will be analyzed at the paragraph 4.9.

## *4.5. PFO and LLO comparison*

Our results on Planar Lipid Membrane reveal the influence of membrane composition on the activity of the two CDCs, data that confirm the binding results present in literature. Both the cholesterol amount and the phospholipid component can modulate the pore-forming activity. In presence of 50% cholesterol, both PFO and LLO make very defined and stable pores, which we can be correlated to a complete ring pore structure. Instead, by reducing the cholesterol amount, the pores formed are smaller and more noisy and unstable. Similarly to what reported by Praper et al., (2011a), we hypothesize that big pores correspond to complete ring structures, smaller and noisy pores are caused by the aperture of incomplete arciform proteolipidic pores. We'd like to further support this interpretation by means of topological images taken by atomic force microscopy in similar membrane environment playing with the two extreme compositions, i.e. POPC:CHO 1:1 and DOPC:CHO 4:1. If our results and interpretations are convincing, we could interpret unresolved current increases as being associated by the growing of incomplete arc-shaped pores.

## 4.6. PFO AFM images

From the electrophysiological measurements, we identified different kinds of pores formed by Perfringolysin O or Listeriolysin O. In POPC:CHO 1:1 both toxins formed very define-step like increases that we associated with ring-shaped structure. In DOPC:CHO 4:1, they presented smaller and more noisy openings or unresolved current increases that can be correlated with incomplete arciform pore structures, which can eventually grow in size by the addition of further monomers. I schematized the two different models for pore opening in Figure 4.20: pre-pore to pore transition (Figure 4.20a) and arc-shaped formation (Figure 4.20b). The two models differ not only in the final pore structure but also in the pore-forming mechanism. In the first case, ring pore model, the monomers interact with the membrane, bind to it and start the oligomerization towards the formation of fully proteic annular structures. Only after reaching the complete ring shape, there is the cooperative insertion of the protein domains devoted to membrane perforation and β-barrel formation. Instead, in the arciform pore formation, the monomers bind to the membrane, oligomerize till they reach an arc structure large enough to have the energy to collapse into the bilayer. In this case the active lesion is made of both protein and lipid head groups and could therefore be less stable.

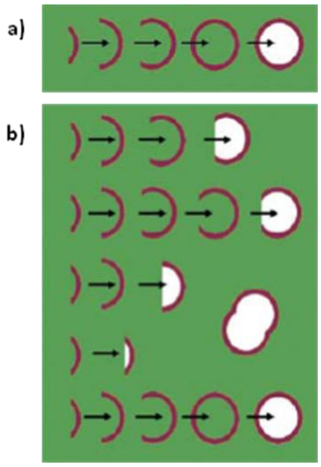


**Figure 4.20 Two pore-forming mechanisms**.

a) Pre-pore to pore models: monomers bind, oligomerize on membrane surface and when a complete ring is formed the pore is opened; b) Oligomeric pore formation: monomers bind and oligomerize but active pores can formed even if the ring structure is not completely organized (figure modified from Gilbert, 2005)**.**

Our results seems to fit and support both models present in the literature, not privileging one over the other. The two different behaviors seem linked with membrane fluidity and cholesterol exposure, which has a remarkable influence on the toxin binding affinity.

In order to confirm the electrophysiological activities and our hypothesis about the two pore structures, we decided to use nano-resolution microscopic techniques to visualize what the pores look like. Based on a previous paper of Czajkowsky et al., 2004, we decided to use Atomic Force Microscopy (AFM), a facility present at Bruno Kessler Foundation in Pederzolli's group.

In that paper, Czajkowsky et al. reported the use of AFM as a tool to discriminate PFO inactive pore structures from active ones on supported lipid bilayer. It is known, from Tilley et al., 2005, that Pneumolysin (PLY), and all CDCs in general, is subject to a huge 3D conformational rearrangement that shortens the monomer height by about 3nm. Using Cryo-EM techniques on liposome with bound PLY oligomers, they were able to visualize and reconstruct two oligomeric pore forms: the pre-pore structure that rises 100Å above the membrane surface and the active pore form that rises 70Å from the bilayer.

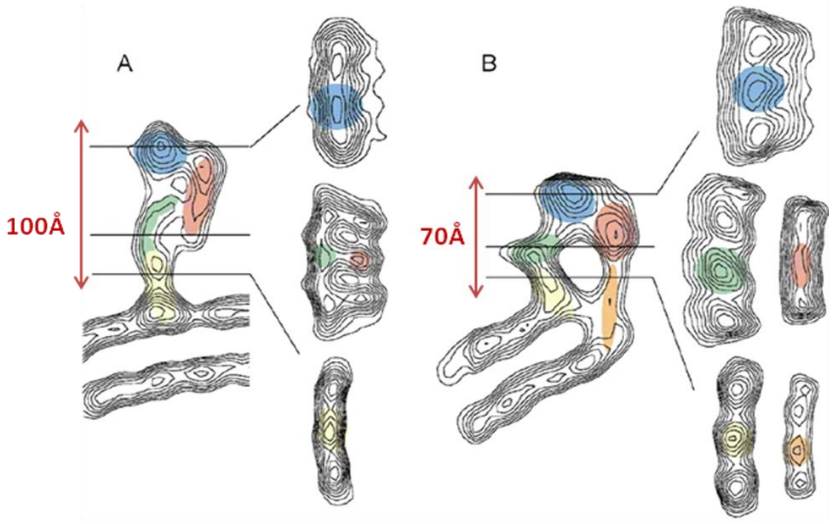


**Figure 4.21 Different heights between bound and inserted protein.**

A) Bound monomer is exposed 100Å from the lipid bilayer; B) Inserted monomer has an height of 70Å above the membrane (figure modified from Tilley et al., 2005).

The vertical collapse of the structure is therefore a characteristic hallmark that allows to discriminate the active pore from the bound but non inserted oligomeric structures. Since AFM can describe both the surface profile and the height of the sample, we can discriminate the active from the not active pore structures.

### 4.6.1. PFO structures on POPC:CHO 1:1 supported membrane

We started our investigation using the same condition applied in Czajkowsky et al., 2004, changing only the method to obtain the supported bilayer (from Langmuir-Blodgett deposition to liposome fusion technique). POPC:CHO 1:1 membrane was the first composition analyzed. After setting all the parameters, we were able to replicate the PFO data in literature. The supported membrane we produced was very homogeneous, and protein structure stable enough to obtain good resolution in tapping mode condition.

The best sample on POPC:CHO 1:1 was obtained incubating 64nM PFO for 10 minutes, pH 7.4, at room temperature. In this condition, PFO forms very well structured ring pores (97% of the structures), as visible in Figure 4.22.

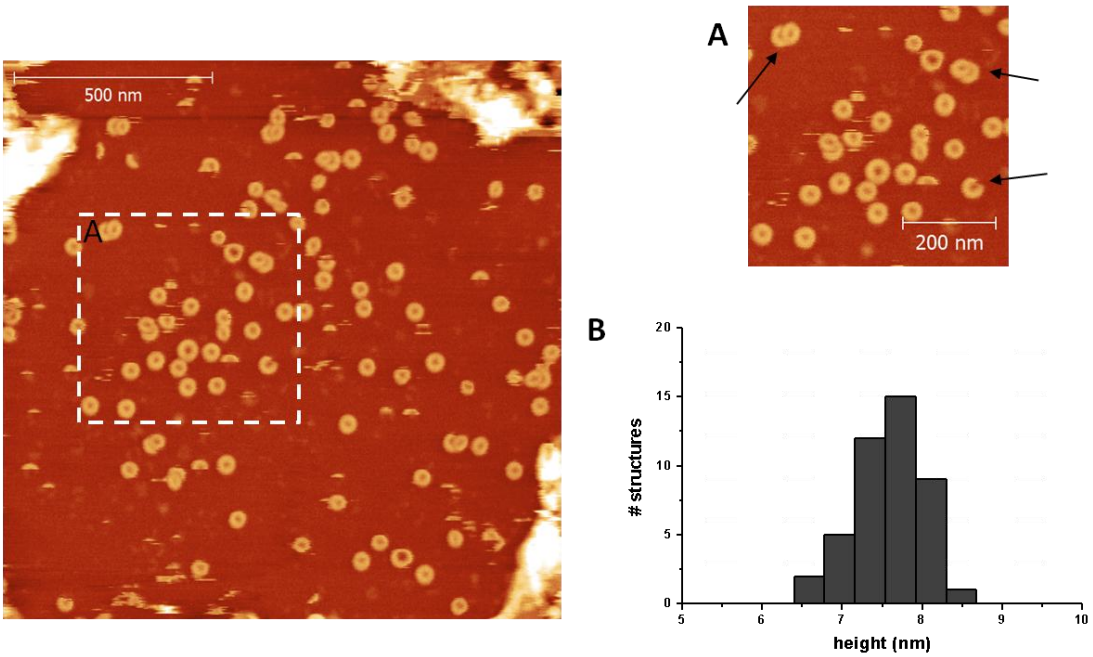


**Figure 4.22 PFO pore structure on POPC:CHO 1:1 supported bilayer at pH 7.4.**

Liposome fusion made a uniform supported bilayer in which pore structures are visible. They are predominantly rings, well defined and similar in dimension, with some few arcs and clustered arc-ring structures (arrows in the zoomed field in fig. A). B) Cumulative histogram of structures' heights. Mean height value is 7.6 ± 0.4 nm (44 heights reported).

In the representative image reported above, there are predominantly circular structures but there are also the minor presence of incomplete structures or "double ring" assemblies.

The dimensions of the ring are quite homogeneous, even if there are some variations as reported in Figure 4.23. The mean diameter value calculated is 24.8 nm, with the diameter values most concentrated between 18-30nm.

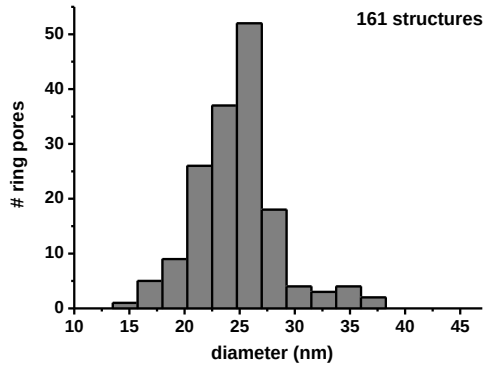


**Figure 4.23 PFO Ring pores diameter.**

Cumulative histogram of 161 ring structures formed on POPC:CHO 1:1 supported membrane. The measured diameter (in nm) was calculated from three different images.

As mentioned before, with AFM we can also analyze if the pore is in an active or closed configuration simply measuring the height of the structures protruding from the membrane surface. As clear from the heights profile in Figure 4.22-B, all PFO structures are collapsed into the bilayer, both the well structured rings and also the incomplete arcs.

We also tested different PFO concentrations and incubation time. Working at higher toxin concentration (64 nM) we induced the formation of protein multilayers on the membrane which do not permit to recognize single pore structures. A similar effect was also obtained increasing the incubation time with 64nM PFO concentration.

Another important result was obtained on EggPC:CHO 1:1, membrane composition that produces more stable supported bilayer especially at pH 5.5 (typical LLO conditions) as I will discuss later. EggPC is a phospholipid mixture extracted from chicken egg that, besides a few percent of sphingolipids, predominantly contains POPC, so PFO activities would be similar to those reported for POPC:CHO 1:1.

The images of that sample were indeed very similar to those obtained on POPC:CHO 1:1. In fact, they showed the presence of well defined ring pores and also incomplete arc-shaped structures. It may be worth noting that in proximity of arciform pores the bilayer structure is partially destroyed and mica becomes accessible by the AFM tip.

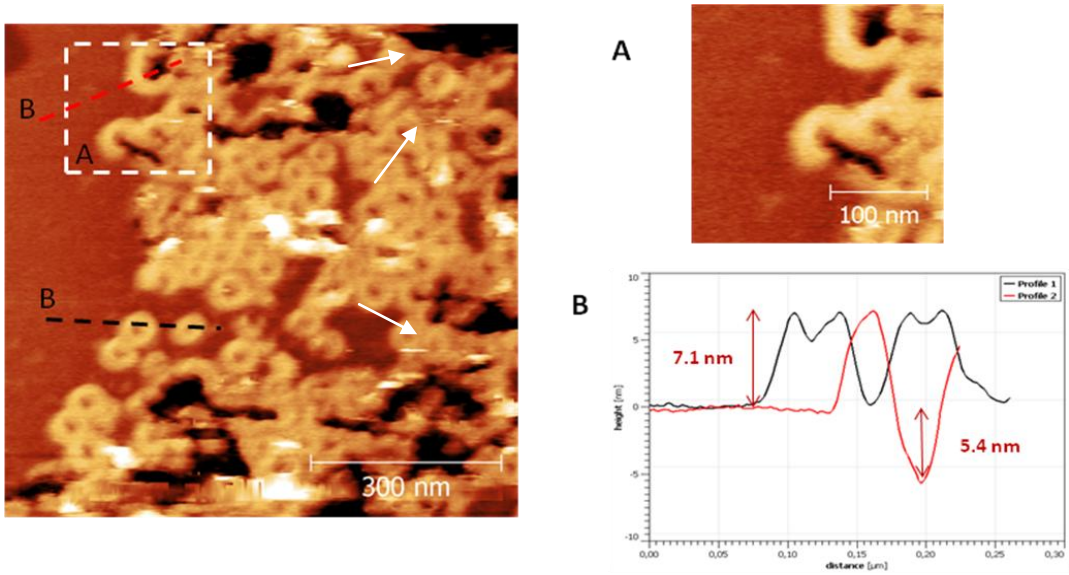


**Figure 4.24 PFO activity on EggPC:CHO 1:1, pH 7.4.**

PFO formed mostly ring structures with some interconnected arc-shaped pores. These last structures formation disrupt the internal lipid bilayer meaning they are correctly inserted into it. A) Magnification of two interconnected arcs. $[PFO]_{final}$= 64nM and 45 min incubation time. B) Two topographic profiles of ring structures and multiple arc formations with membrane disruption.

Besides permitting a fine tuning of the AFM heights, this behavior highlights the propensity of arciform oligomers to modify the bilayer lamellarity.

Our first results demonstrated that we succeeded to reproduce and visualize the ring pores as presented in Czajkowsky paper with a higher "efficiency". In our PFO wt images we clearly confirmed the significant presence of arciform oligomers which accounts for almost 50% of all the structures seen, structures present in Czajkowsky paper as well but not discussed there. Another aspect to take into account is that the beautiful full-ring structures reported in Czajkowsky work were obtained with a blocked version of Perfringolysin O mutant that cannot insert into the bilayer and can therefore favor full ring completion.

In our results with this membrane composition, most of the PFO pores are complete proteic rings but also evident is the presence of arciform oligomers in their inserted (and therefore functional) configuration. This finding matches very well with our electrophysiological results in which we observed bimodal distribution of well defined step-like increases: big pores can be associated to complete rings; small and noisy pores correspond to arc-shaped oligomers, that are active pores.

### 4.6.2. PFO structures on DOPC:CHO 4:1 supported membrane

We have shown that PFO is very sensitive to membrane cholesterol content with PLM analysis. We highlighted DOPC:CHO 4:1 as the extreme condition where it was almost impossible to sort out a step-like increase in the current traces, so we decided to interrogate this particular membrane with AFM.

Interestingly we confirmed the instability of the protein sample, in fact PFO structures were mobile on the bilayer plane and not strongly anchored on it. The sample presented region covered by protein, more or less organized, and naked bilayer regions. Moreover, in this case the protein formed a first layer on the membrane surface simply lying on the bilayer (2-3 nm in heights) and some oligomeric structures. In Figure 4.25 it is possible to see that most of the structures were arc-shaped oligomers (90%) with the presence of some sporadic rings.

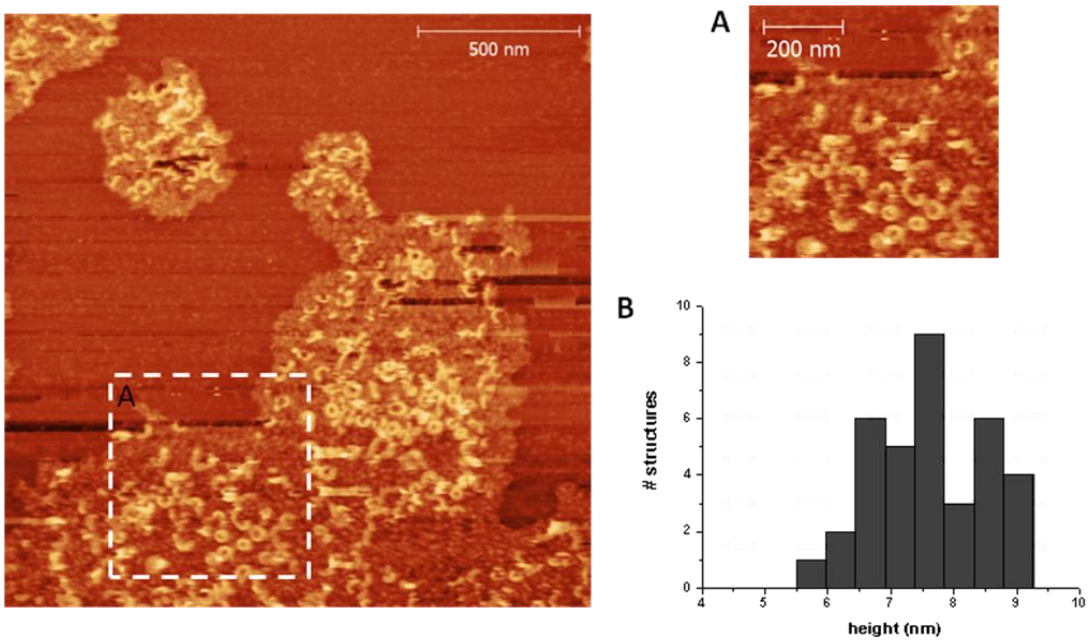


**Figure 4.25 PFO pore structures on DOPC:CHO 4:1 membrane, pH 7.4.**

On this membrane composition, PFO forms regions of monomers lying on the bilayer containing many arc-shaped structures and also some ring structures. $[PFO]_{final}$= 64nM and 10 min incubation time. A) Magnification of some PFO structures. B) Cumulative heights histogram of PFO structures. Mean height = 7.6 ± 0.9 nm (36 heights reported).

All the structures (arcs and rings) are inserted into the bilayer, as visible from the height profile in Figure 4.25-B. The height of the oligomers is about 7.6 nm and the layer of protein is around 2.8-3nm, which corresponds to the monomer width.

## 4.7. LLO AFM images

After setting all the experimental conditions with the better known PFO, we moved to characterize Listeriolysin O. From PLM analysis, we demostrated pore-forming similarity between PFO and LLO in the different membrane composition tested. Both toxins showed similar activities in 50% cholesterol containing membrane but the pore formation on 20% cholesterol is sligthly different. PFO is sensitive to both sterol amount and phospholipid acyl chain, instead LLO is more influenced by the acyl order of the phospholipids. Looking at PLM results, in fact, PFO presented two diverse behaviours on 20% cholesterol containing membranes (small step-like increase on POPC and indefine increase on DOPC), different also from the PFO pore formation in lipid:sterol 1:1 composition. Instead, LLO presented similar behaviour on POPC membranes (both 50% and 20% cholesterol amount) and smaller step-like increase or noisy increase on DOPC:CHO 20% bilayer.

Also in the case of LLO, we wanted to recognize the active pore structures and their correlation with membrane composition. Since the most effective parameter is the phospholipid order, we decided to investigate with AFM the two extreme membrane compositions POPC:CHO 1:1 and DOPC:CHO 4:1. One important thing to remember is that LLO acts mainly at pH 5.5 which means that AFM images had to be taken at this pH. We found that the acidic pH environment makes less stable supported bilayer, especially in 50% cholesterol containing membrane. We had to play a lot with all the experimental parameters (salt concentration, $Ca^{2+}$ amount, incubation time and washing steps) to find the best condition for getting stable supported membranes.

### 4.7.1. LLO structures on POPC:CHO 1:1 supported membrane

As mentioned before, a stable and homogeneous membrane is necessary to acquire high resolution images in liquid environment and to avoid distorsion effects on the pore structure. As it is reported in Figure 4.26, for LLO on POPC:CHO 1:1 at pH 5.5, the bilayer is not present in all the scanned sector. This can be due to an intrinsic instability of the supported bilayer that during the washing step is pulled up or it can be an effect of LLO interaction with the membrane.

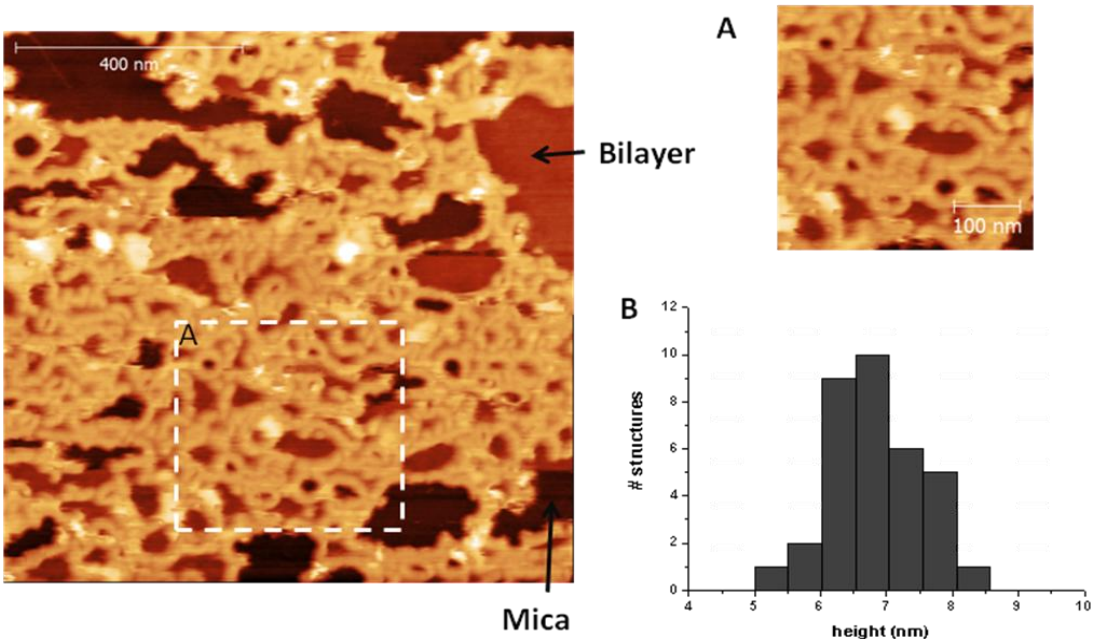


**Figure 4.26 LLO pores on POPC:CHO 1:1 membrane, pH 5.5.**

Supported bilayer is not uniform, there are many spot in which Mica is visible. $[LLO]_{final}$= 28nM and 10 min incubation time. A) Magnification of some ring and arc structure from the bigger field. B) Cumulative histogram of the measured heights. Calculated Mean height is 6.8 ± 0.7 nm (34 structures analyzed)

On the stable bilayer patches LLO undergoes vertical collapse and forms inserted structures, as confirmed by the histogram of the heights. Among all the structures the percentage of rings consists of 40%.

Slightly changing the experimental conditions (moving to EggPC:CHO 1:1 membrane), we were able to further improve the bilayer stability: some broken membrane areas are still present, tipically inside huge hyper-structure of arciform-oligomers as reported also for PFO on EggPC:CHO 1:1. The finding of similar arcs hyper-structures depleted of internal bilayer both for PFO and LLO and at both pHs reveals the ability of arciform oligomers to form active pores, which means insertion of β-barrel into the bilayer and pore aperture.

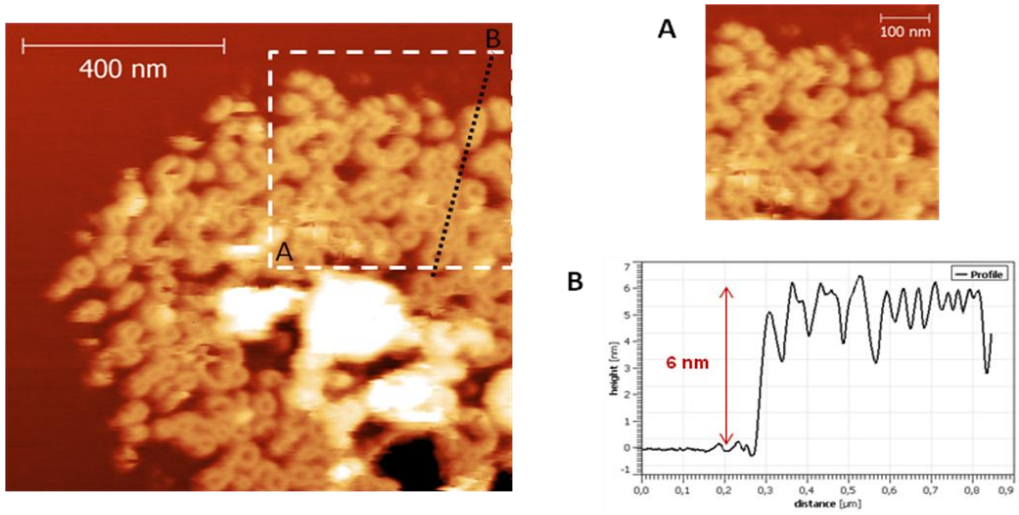


**Figure 4.27 LLO activity on EggPC:CHO50% membrane, pH 5.5.**

EggPC:CHO 1:1 membrane is uniform and LLO pore structures (mainly rings) are clusterized insome spots. $[LLO]_{final}$= 130nM and incubation time of 45 minutes. A) A magnification of some structures in the left image. B) A topographic profile of some LLO structures (mean height around 6 nm).

As seen in Figure 4.27, EggPC at pH5.5 improves membrane and protein structure stability, allowing the acquisition of images with higher spatial resolution. We observed many "island" of protein pores surrounded by membrane bilayer. Zooming on the sample, it became possible to visualized well resolved circular structures with some arc assemblies. Also in this case, some hyper entities of arcs with inner membrane lacking are present; this fact supports the hypothesis of arc activation and insertion into the bilayer leading to the huge 'hole' constituted of more arcs. In the figure below, the distribution of pore diameters is reported.

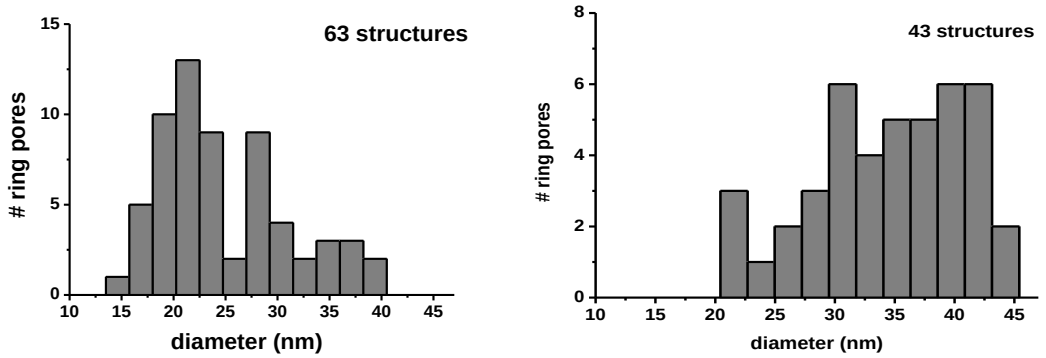


**Figure 4.28 Cumulative histogram of ring pore diameter calculated on AFM images.**

Comparison between the dimension of the pores observed in POPC:CHO 1:1 (left histogram) and EggPC:CHO 1:1 (right histogram).

LLO pores on EggPC:CHO 1:1 are slightly bigger than those on POPC:CHO 1:1, i.e. 34.2 ± 6.1 nm and 24.6 ±6.3 nm respectively.

### 4.7.2. LLO structures on DOPC:CHO 4:1 supported membrane

Once visualized the ring promoting membrane, we were interested also to understand the kind of structures made by LLO into DOPC:CHO 4:1. We prepared and imaged LLO sample on this membrane incubating LLO for 10 minutes as we did with POPC:CHO 1:1.

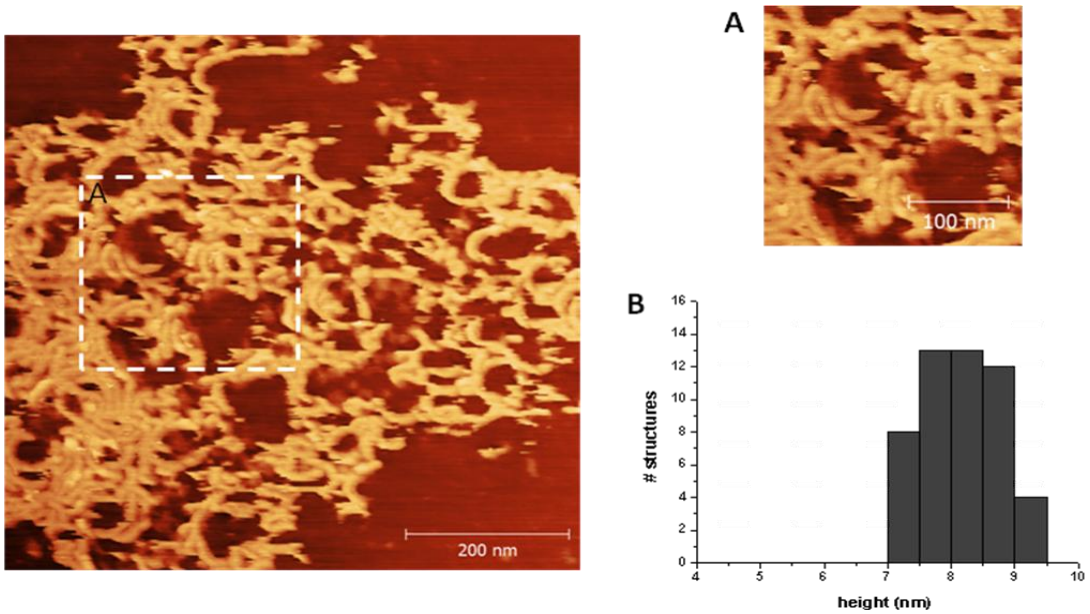


**Figure 4.29 LLO pore structures on DOPC:CHO 4:1 membrane, pH 5.5.**

Arc-shaped structures visible in localized areas on the supported bilayer. $[LLO]_{final}$= 28nM and 10 min incubation time. A) Magnification of the pore structures. B) Height cumulative histogram of 50 structures. Mean height = 8.2 ± 0.6 nm

The sample presented an uniform bilayer covered by LLO arc structures. In all the field scanned there is no ring-shaped structures but only arciform oligomers, eventually clusterized and attached to each other, as visible in Figure 4.29

The heights of the structures are compatible with LLO active pores. However, what it is strange is the absence of membrane disruption inside the hyper-structure of arciform oligomers that are instead present in the membranes with higher cholesterol content. This membrane composition seems to be more resistant to the toxin perforation and opening of huge 'holes'. Making a comparison with PFO structures in the same membrane composition, it is evident that LLO is more organized into stable structures than PFO, maybe reflecting a higher binding affinity of LLO for this membrane.

## 4.8. LLO mutants production and purification

In order to understand better if LLO can form different kinds of active pore structure, we planned to produce inactive mutants that allow us to visualized not inserted structures on supported lipid bilayer. From the literature, there are many examples of PFO recombinant inactive proteins. Based on these, we designed two inactive mutants (monomer rearrangement is blocked by a disulfide bond) that can be activated with reducing agent addition. So, we studied LLO hypothetical monomeric 3D structure (remodeling by comparison with PFO crystal structure and sequence similarity between the two toxins) and we found two regions of the protein where a disulfide bond can block the conformational changes occurring during monomer insertion into the membrane. We identified two amino acids in D3 domain (TMH1 region) closed enough to create a S-S bridge and two residues that, mutated in two cysteines, can connect D3 with D2 domains, as visible in Figure 4.30.

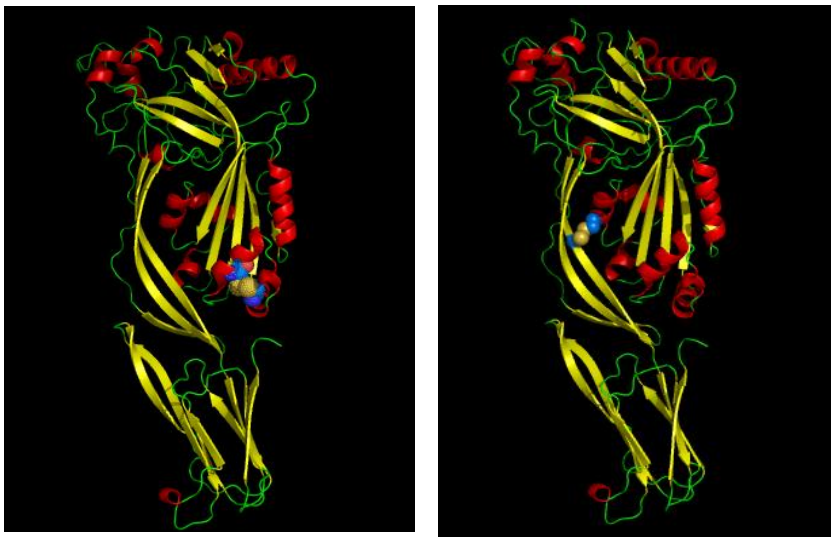

**Figure 4.30 Predicted tridimensional structure of LLO.**

Left image, LLO A318C-L334C structure with the two cysteine residues depicted in blue and yellow. Both the substitution are on D3 domain, the one that gives rise to the β-barrel structures. Right image, LLO Q216C-Y206C structure with the two cys in blue and yellow. One cys rediue is in the α-helix of D3 domain, instead the second one is on a β-strand of D2 domain.

The first double mutant, A318C-L334C, is connecting the two short α-helices (TMH1 part) in D3 domain, linked positions that do not allow the transition from α-helices to β-hairpins. The second LLO mutant, Q216C-Y406C, has one amino acid substitution in TMH2 helix and the other substitution at the level of one of the β-strands of D2 domain. This S-S

bridge created is less exposed than the previous one and it will probably maintain the monomer more packed, inhibiting completely the unfolding process to active pore conformation.

Starting from the two pET8c-LLO plasmids obtained after mutagenesis, I transformed BL21 cells, grew 4 L of culture till it reached an $OD_{600}$ = 0,9-1 and induced LLO overnight expression by IPTG addition (final concentration 0,5 mM). After LLO expression, bacteria was lysed and centrifugated to recover LLO from the supernatant. The purification consisted in two steps: a first purification on Ni-NTA column (His-tag affinity) and a second Cation-exchange chromatography.

### 4.8.1. Purification

I loaded all the supernatant coming from 4L of culture in a homemade Ni-NTA column and eluted LLO protein with a 300 mM Imidazole buffer. The peak is all recovered (10 ml) and dialyzed overnight to exchange the buffer solution (pull down Imidazole concentration and decrease salt concentration according to the next step of Cation-exchange chromatography). All the following data were coming from the first double cys mutant (A318C-L334C) purification but similar results were obtained for the purification of the second mutant (Q216C-Y406C).

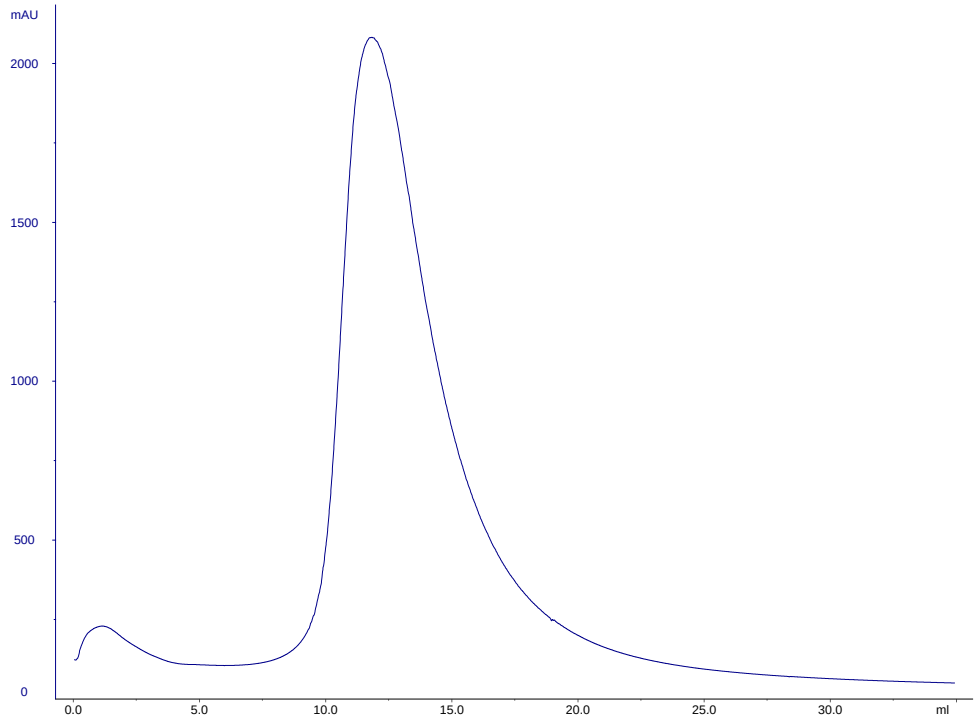


**Figure 4.31 Ni-NTA purification profile.**

Elution profile of His-tag LLO from Ni-NTA column. The elution is performed with a single step of 300mM Imidazole buffer. The two peaks in the UV profile (blu trace) is the LLO containing fractions.

Checking all samples, bacterial and purified ones, on an acrylamide gel it is possible to see that LLO is easily expressed in BL21 cells (AI band between 75 and 50 kDa). LLO presence in the two peaks coming from Ni-NTA column was confirmed but the protein is still not very pure; a lot of bands at lower molecular weight than LLO protein were present (contaminant bands).

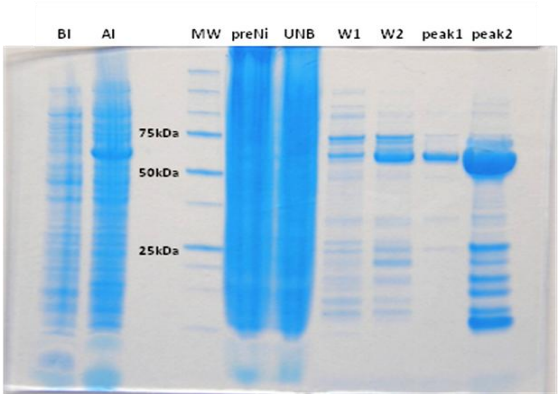


**Figure 4.32 SDS-PAGE of several LLO A318C-L334C samples from expression and Ni-NTA purification step.**

The sample loading order is the following: **BI**, cells before induction; **AI**, cells after induction (slightly visible LLO band around 60kDa); **empty column; MW**, molecular weight marker; **preNi**, cell lysate before chromatographic column; **UNB**, unbound sample from column; **W1 and W2**, two washing steps of the column; **peak1 and peak2**, LLO elution peaks.

After this step, peak1 and 2 was purified by Cation-Exchange Chromatography using a salt gradient to better separate the peak. From this second purification step, LLO is elute almost pure.

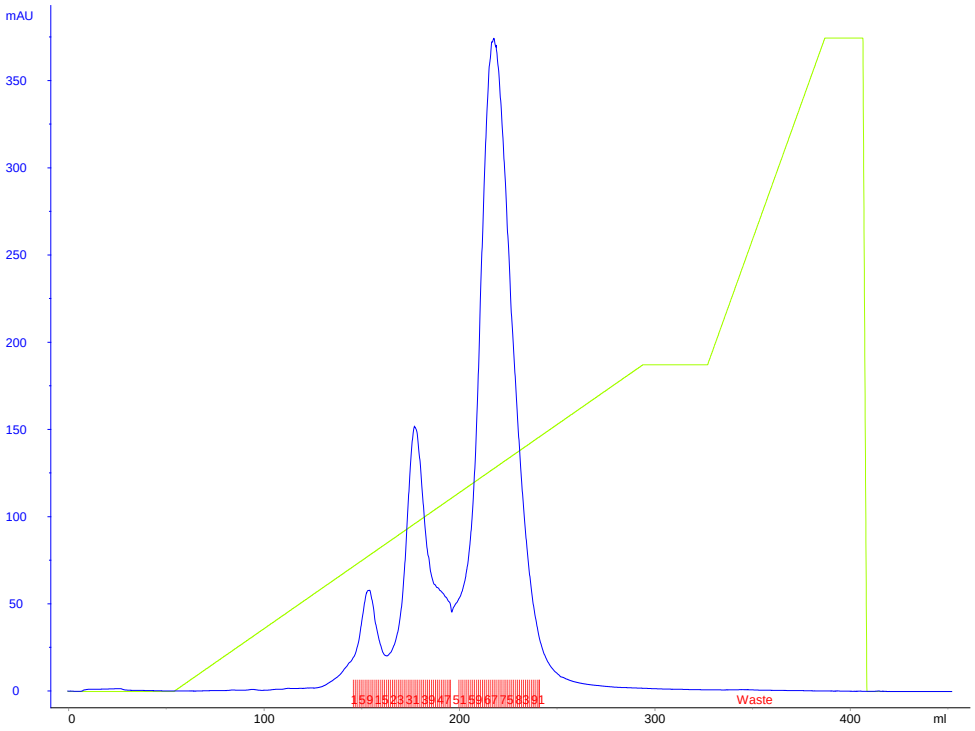


**Figure 4.33 LLO A318C-L334C cation-exchange chromatography profile.**

Blue curve: UV profile of eluted protein. Green curve: salt concentration gradient for LLO elution. Red bars: protein fractions collected. Maximum salt (NaCl) concentration passed through the column is 1M (ending step to elute everything).

Three peaks were present in LLO elution profile from CEC column. Screening them on a SDS-PAGE gel, it was possible to indentify the purest fractions that finally were concentrated and used for the experiments.

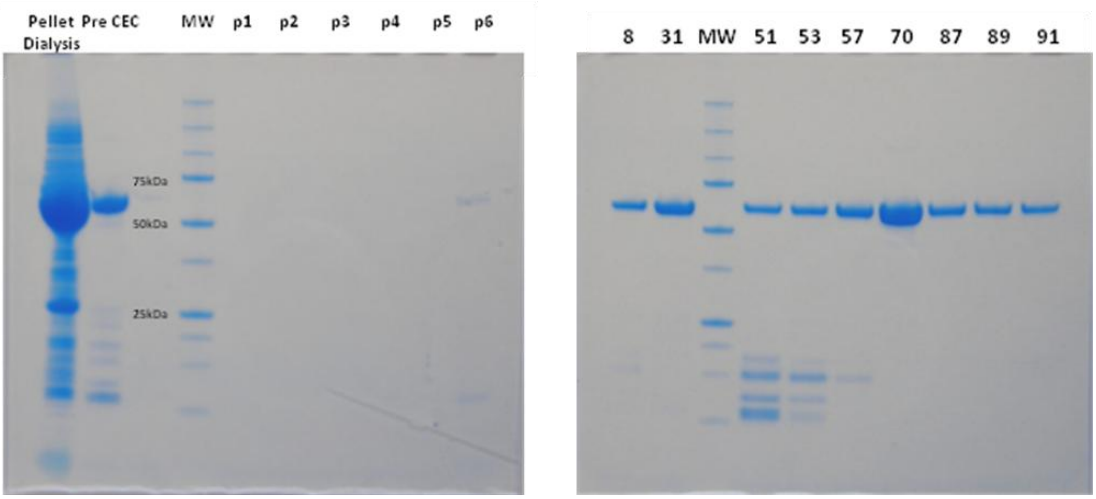


**Figure 4.34 SDS-Page gels of A318C-L334C cation-exchange fractions.**

Gels containing LLO sample from CEC column. *First gel on the left*: **Pellet dialysis**, protein pellet obtained after centrifugation of dialyzed sample; **Pre CEC**, supernatant after centrifugation; empty column; **MW**, molecular weight marker; **p1 to 6**; six fractions of the first peak in the elution profile. *Second gel on the right*: **MW**, molecular weight marker (same of the other gel); **8 and 31**, fractions of the second peak present in the elution profile;**51 to 91**, sample fractions of the third higher peak.

After analyzing the gel, I decided to take the fractions from 57 to 91, concentrate them till the final concentration of 10 mg/ml (around 1 ml final volume) and store protein aliquots at -80°C till use. The same procedure was applied to the second double mutant.

### 4.8.2. Hemolytic assay

First of all, I wanted to test the lytic activity of the two mutants in order to verify if they were re-activable, so I performed a hemolytic assay on Human Red Blood Cells (HRBC). From our plans, these mutants have to be inactive when they are completely oxidized (disulfide bond should block the monomer unfolding) but in presence of a reducing agent their pore forming activity should be restored. I screened different samples: LLO wt (as control), and both the double mutants (A318C-L334C or Q216C-Y406C) pre-incubated or not with oxidizing agents or DTT as a reducing agent.

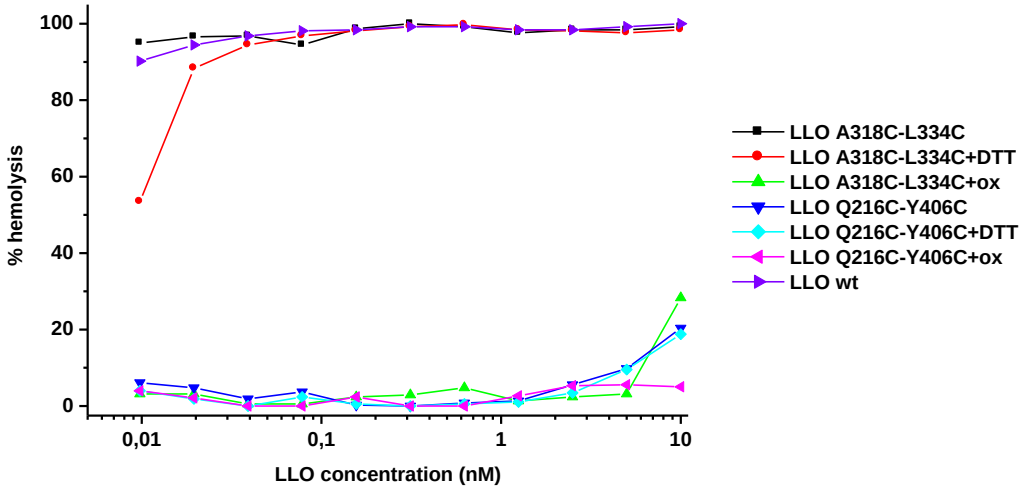


**Figure 4.35 Hemolytic activity of several LLO concentrations on HRBC.**
Legend on the right reported the sample order. The assay was done at pH 7.4.

The hemolytic assay revealed that mutant A318C-L334C was purified as active toxin, but it can be easily inactivated with oxidizing treatment. Then, if needed, pore forming activity can be restored incubating LLO with reducing agents. The mutant Q216C-Y406C instead, seemed to be less interesting than the first. In fact, the first hemolytic test showed no lytic activity in the three conditions tested: as it comes from the purification, after oxidizing treatment and after reducing treatment. The preliminary results were not so attractive for this mutant but going deeper into the matter I found a more interesting result. Restored activity can be obtained if DTT is applied after mutant incubation with (Human or Rabbit) Red Blood Cells. This fact suggests that the disulfide bond is accessible for DTT only when the protein in the membrane bound configuration.

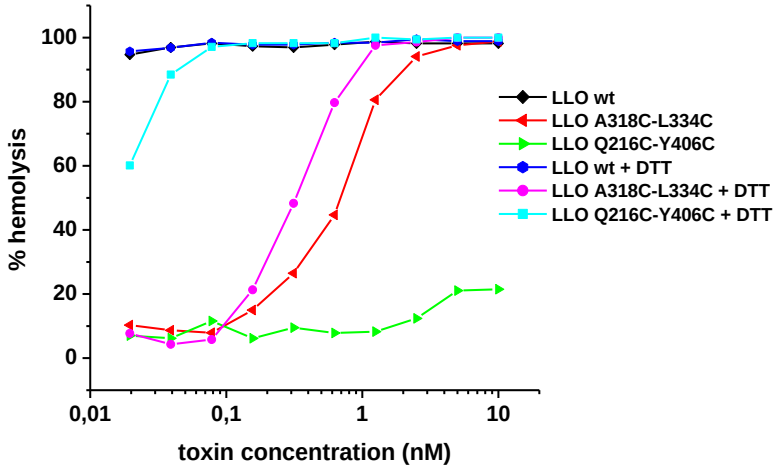


**Figure 4.36 Hemolytic test of the three mutants with a second step of sample reduction.**

Proteins were first incubated with RBC for 30 min (black, red and green samples) and after there was DTT addition and other 30 min kinetic measurement (blue, pink and cyan samples)

### 4.8.3. Protein stability

For getting information on the protein structure (either wt or double mutants) we performed Differential Scanning Fluorimetry (DSF) assay (Niesen et al., 2007) at different pHs and temperatures. This test allows to monitor protein thermal unfolding in a easy way. The fluorescent dye used, SYPRO Orange, binds to the hydrophobic part of proteins, so it is specific to follow denaturation and aggregation (fluorescence increasing meaning protein unfolding). In order to compare the three proteins, we looked at the Tm value (inflection point) of each fluorescent curve (see 3.2.5) and organized all the value in a graph 'pH vs Tm'.

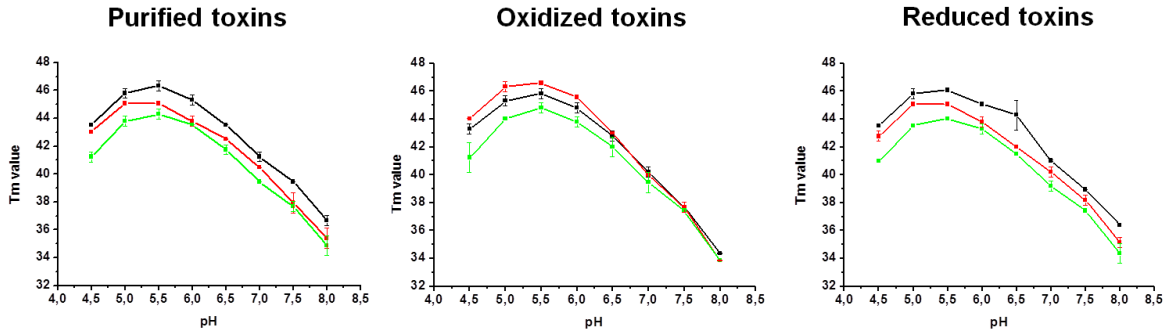


**Figure 4.37 Thermal stability of LLO wt, LLO A318C-L334C and LLO Q216C-Y406C at different pHs.**

Toxins (5µM) were tested as they are purified, after an oxidizing step and a reducing step. Black points: LLO wt; red points: LLO A318C-L334C; green points: LLO Q216C-Y406C.

The results showed similar unfolding/stability curves among the three proteins tested but evidenced a small thermal decrease in stability (1-2°C) for the two mutants in comparison with LLO wt. LLO A218C-L334C mutant seemed to be the less stable, both as it was purified and after oxidizing or reducing treatments, meaning that the two substitutions destabilize the natural TMH1 folding. Interestingly, the other mutant was less stable than LLO wt as it was purified and after reducing treatment, but LLO Q216C-Y406C was a bit more stable of LLO wt when treated with oxidizing agents. This result confirmed that the second mutant works as expected: in fact, linking D2 to D3 domain, the disulfide bridge goes to block LLO activity but also prevents pH unfolding processes.

### 4.8.4. LLO double cys mutant images

The first hemolytic characterization revealed that the first double Cys mutant, A318C-L334C is exactly as we planned, instead the second one, Q216C-Y406C, has a particular unexpected feature. This second LLO mutant is very interesting since it seems to be re-activated only after membrane binding occurs. This aspect of the second mutant can be very useful to understand better the mechanism of LLO binding, α-helices to β-barrel rearrangement and active pore formation. But most of all, this protein makes our AFM sample preparation easier, less time-consuming, but also allows to avoid oxidizing conditions on supported bilayers chamber, which can destabilize the membrane. Since the best sample of LLO ring pores was on EggPC:CHO 1:1, we tested LLO Q216C-Y406C on this membrane composition. In this sample LLO structures were not equally distributed: there were some spots of very concentrated oligomers; single ring pores were found in different regions well separated from this island. The LLO concentrated area showed interconnected arcs, one inside the other, which reduce the sample resolution.

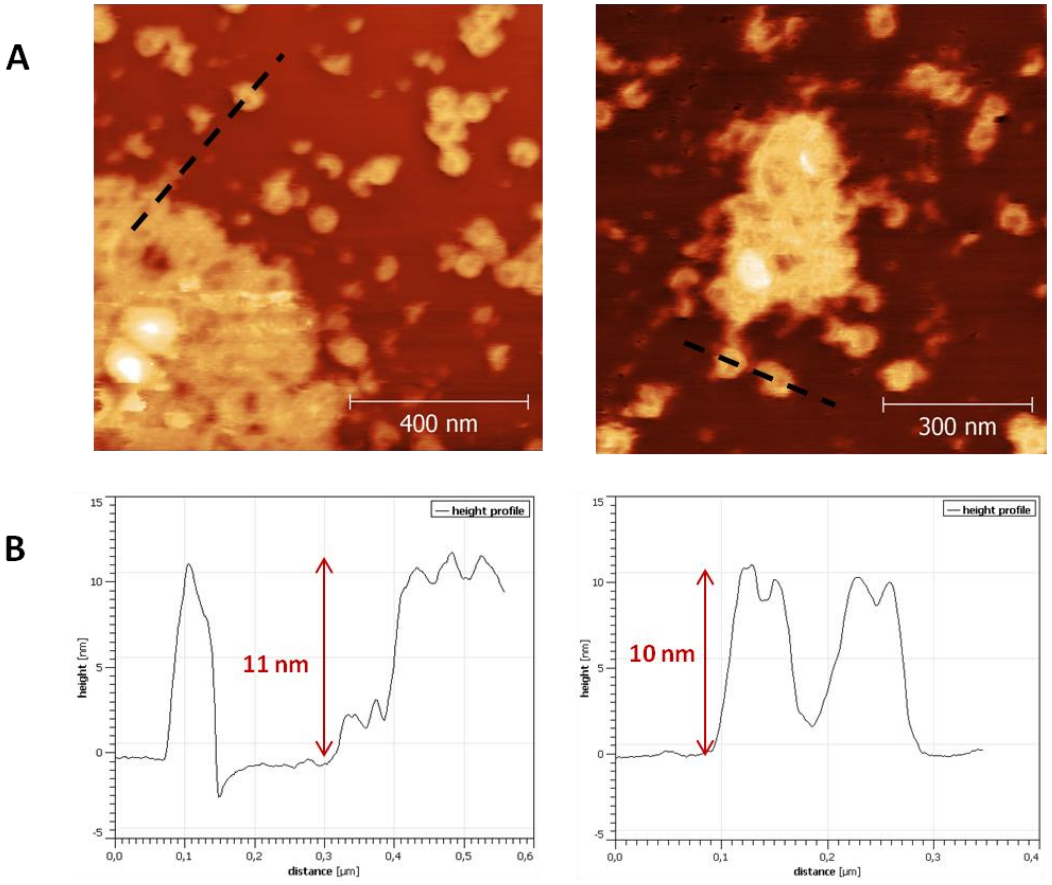


**Figure 4.38 LLO Q216C-Y406C pores on EggPC:CHO 1:1, pH 5.5.**

Toxin (64nM) was incubated for 45 min and after a washing step, pore structures were visualized. A) Two fields presented arc assemblies stuck to each other with surrounding isolated pore structures, both arcs and rings. B) Topographic profile of the arc assemblies on the left, and ring pore structures on the right. Both structure heights correspond to the not inserted protein.

Isolated in the surrounding membrane, rings and a few arcs are visible, but also in this case the structures were not very stable. Proteins stack to the membrane due to the simple interaction but no insertion of the protein into the bilayer was observed. The heights of all the structures corresponded to the not inserted protein, so inactive pore or pre-pore states are the only structures present. This result was just what we wanted to obtain and gives us much information about the pore structure and formation.

Then we tried to reduce the Q216C-Y406C disulfide bond to restore the lytic activity as we did for hemolytic tests. The best result was obtained incubating LLO mutant for 15 min (protein interaction with the membrane), addition of 0.2 mM DTT inside the sample chamber and incubated for 30 min (for reducing the S-S bond and activating the protein). We obtained a mixture of inactive and re-activated pores. In fact, part of the protein had a height of 10-11 nm and part lower, around 7 nm in height. Obviously, the reducing step

was not optimized to have only active, inserted LLO pores but it was a promising sample for further investigations. Moreover, this partial reduction allowed to have information on both inactive monomer and active LLO.

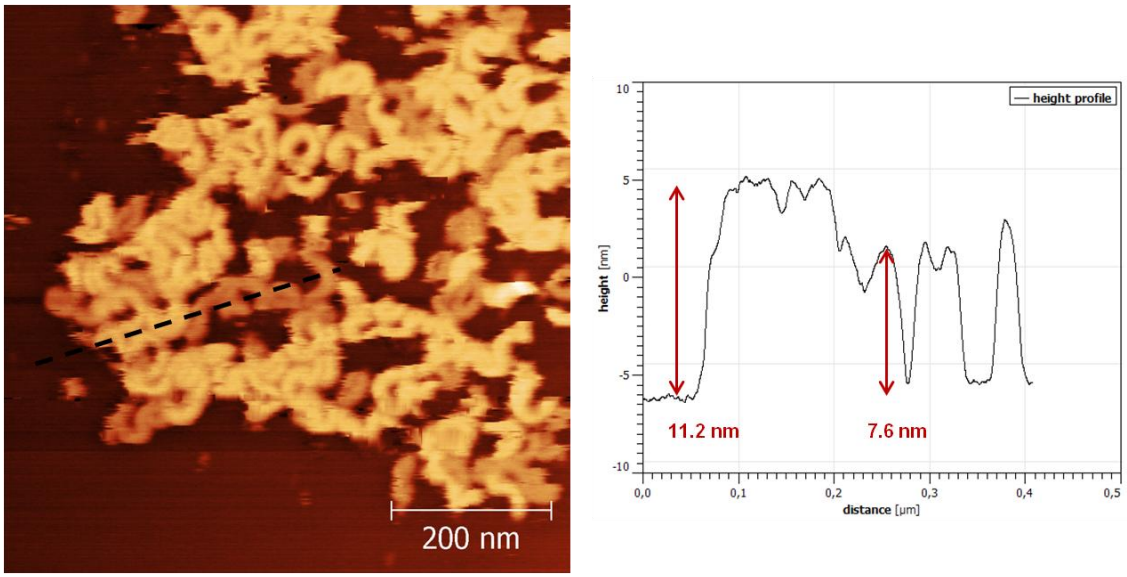


**Figure 4.39 LLO Q216C-Y406C reduced with DTT.**

LLO was incubated for 15 minutes and then a reduction step with $[DTT]_{fin}$ = 0,2 mM was performed. Visible pore structures are both arc and ring pores and in the field is evident the presence of not inserted (higher structures) and inserted pores.

Most of the structures present in the fields, Figure 4.39, are arciform oligomers, but there are also ring pore formations. This sample revealed that LLO can form both complete proteinaceous pores (rings) and proteolipidic pores (arcs) and that is the latter are not only a transient oligomeric step of pore formation, but a separate pore formation mechanism by itself.

## 4.9. PLM analysis of pH dependence

When I presented the Planar Lipid Membrane analysis, I mentioned and discussed the effect of different membrane composition on PFO and LLO pore-forming ability. What I haven't underlined before is the remarkable effect of the pH on LLO activity on POPC:CHO 1:1 membrane. It is known from the literature that LLO is inactivated at pH 7.4 as a result of a premature unfolding, so we expected less protein available and less lytic activity. Instead, interestingly, the membrane affinity seemed to be the same or higher (similar number of pores per time) and the pores were well define step-like increase at both pHs. In the following panel, Figure 4.40, I report the cumulative G histograms of LLO wt at pH 5.5 and 7.4 and it is evident from them that the pores formed at the two pHs differ in size. In fact, the two distributions have G mean values of 12 ± 5nS and 5 ± 2nS at pH 5.5 and pH 7.4, respectively.

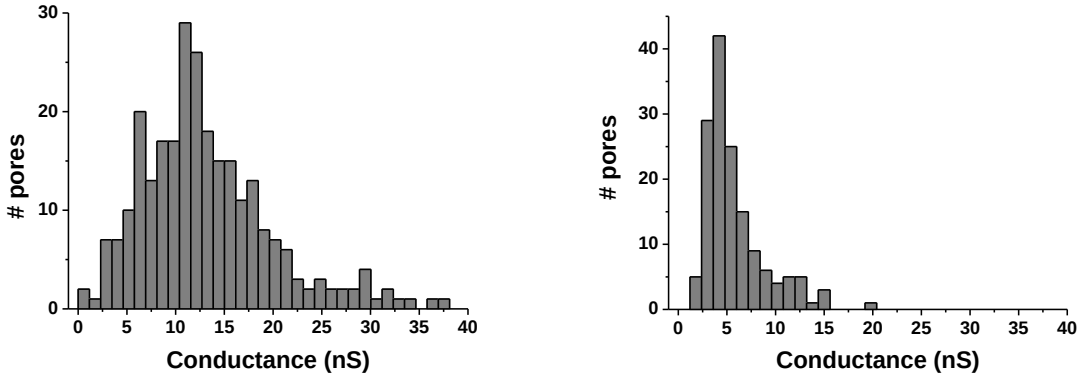


**Figure 4.40 Histogram of LLO pores on POPC:CHO 1:1 at the two pHs.**

On the left, there is reported the conductance histogram of pores made at pH 5.5 (276 pores). On the right, conductance histogram of pores at pH 7.4 (150 pores).

There are two simple possible explanations for this conductance difference:

- less monomeric units form LLO pore at pH 7.4
- the pore molecularity is the same but pH modulates the ion flux, for example by a titratable group positioned in the pore lumen and able to change its internal diameter.

It is already known that LLO premature unfurling at pH 7.4 is due to the titration of three acidic residues in D3 domain, (Schuerch et al., 2005). That unfolding and protein

aggregation can only explain the inactivation of LLO at physiological pH but not the different pore conductivity. Considering the pH sensitivity range, the histidine residue would be a good candidate for this pH titrability in fact, histidine has an isoelectric point of 6.04 (value for single amino acid free in solution). Looking at protein sequence, LLO contains six His residues along its four domains.

**LLO wt sequence**

XXXXXXXHHHHHDYDIPTTENLYFQGAMGSKDASAFNKENSISSMAPPASPPASPKTPIE
KKHADEIDKYIQGLDYNKNNVLVYHGDAVTNVPPRKGYKDGNEYIVVEKKKKSINQNNAD
IQVVNAISSLTYPGALVKANSELVENQPDVLPVKRDSLTLSIDLPGMTNQDNKIVVKNAT
KSNVNNAVNTLVERWNEKYAQAYPNVSAKIDYDDEMAYSESQLIAKFGTAFKAVNNSLNV
NFGAISEGKMQEEVISFKQIYYNVNVNEPTRPSRFFGKAVTKEQLQALGVNAENPPAYIS
SVAYGRQVYLKLSTNSHSTKVKAAFDAAVSGKSVSGDVELTNIIKNSSFKAVIYGGSAKD
EVQIIDGNLGDLRDILKKGATFNRETPGVPIAYTTNFLKDNELAVIKNNSEYIETTSKAY
TDGKINIDHSGGYVAQFNISWDEVNYDPEGNEIVQHKNWSENNKSKLAHFTSSIYLPGNA
RNINVYAKECTGLAWEWWRTVIDDRNLPLVKNRNISIWGTTLYPKYSNKVDNPIE

**Figure 4.41 LLO amino acidic sequence and His residue.**

Complete amino acidic sequence of our LLO protein with the 6 His residues highlighted in yellow.

Listeriolysin O crystal structure is not published yet, so the only way to make some structural hypothesis is to take advantage of PFO/LLO sequence similarity and make LLO 3D structure simulation. From this 3D model, we identified one His residue that is situated in a crucial part of LLO: His 311. This amino acid is probably placed inside the loop connecting one β-sheet of D3 domain and the α-helix TMH1 (green residue in Figure 4.42). Once the conformational change from α-helix to β-barrel occurs, H311 residue will be located upon one of the four β-barrels that form the internal pore wall.

**Figure 4.42 H311 position in LLO 3D structure model.**

The amino acid H311 is highlighted by green spheres. Hypothetical amino acid position based on 3D modeling of LLO sequence compared with PFO crystal structure.

Position H311 seems to be a good candidate for our pH study so we decided to mutagenize the native Histidine into Alanine residue.

During protein production, it turned out that we lost a lot of protein during the dialysis between the first affinity column and the final cation-exchange purification. It was evident that decreasing salt concentration down to 100 mM we induced LLO aggregation. In order to obtain a higher purification yield, we decided to change the purification methods. For these proteins, we inserted LLO wt gene inside pPROEX-HTb plasmid, which contains a TEV restriction site between the His-tag sequence and LLO sequence. The purification steps consisted now of two Ni-NTA column passages which didn't need salt decreasing. The first passage partially purified the full LLO construct (some contaminant were present in the fraction as in the case of the double mutants), then, after His-tag cleavage, the second Ni-NTA chromatographic passage released the pure LLO in the column flow-through.

As previously mentioned, we performed site-direct mutagenesis (His to Ala) on LLO wt gene, transformed bacteria, grew them and induced protein expression. Purified proteins were tested on POPC:CHO 1:1 membrane at the two different pHs previously used.

## LLO wt

As LLO H311A mutant doesn't have His-tag at the N-terminus, I've decided to start the characterization from LLO wt protein not containing His-tag. The main reason is to be sure that the conductance differences at the two pHs is not due to His-tag modulation of the pore luminal aperture.

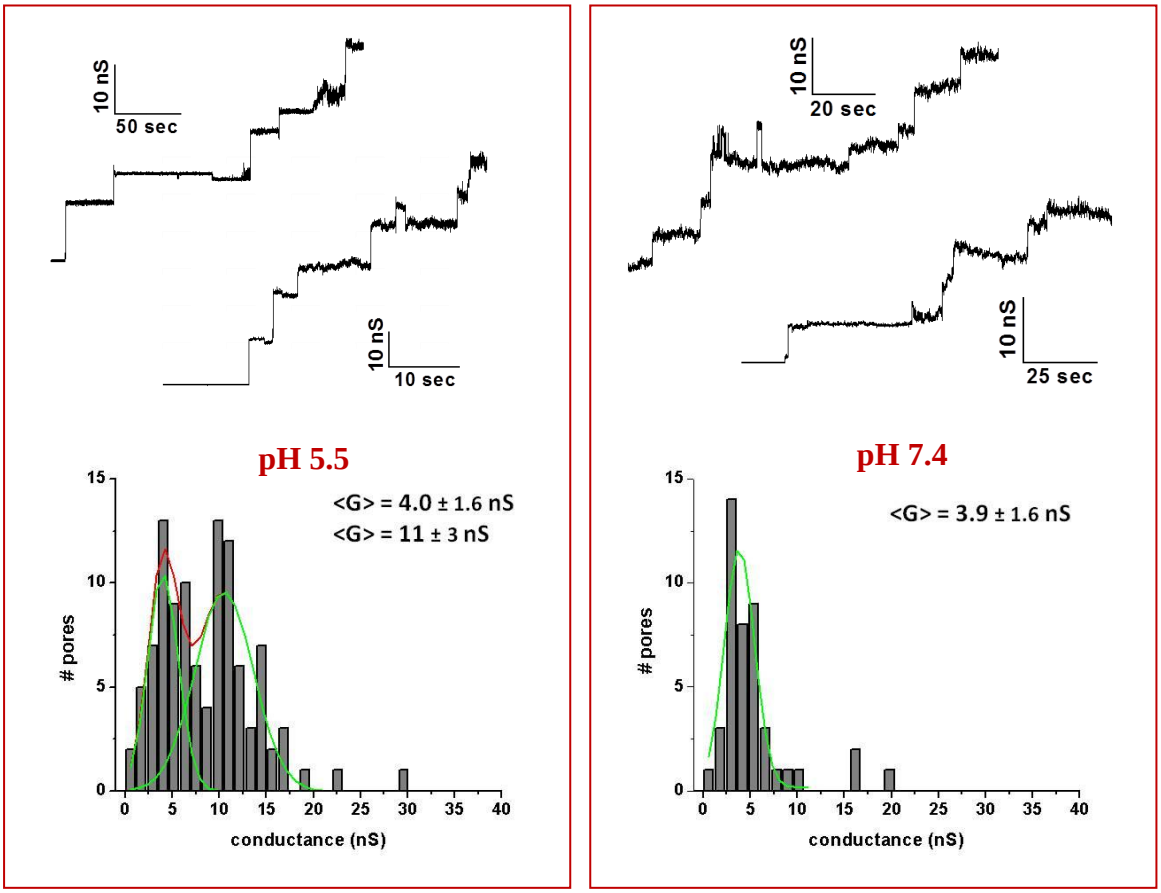


**Figure 4.43 LLO wt activity on POPC:CHO 1:1 membrane.**

Top panels: some examples of current traces at the two pHs. Bottom panels: cumulative G values histogram. Pores analized: 107 pores at pH 5.5 ([LLO]=5nM) and 45 pores at pH 7.4 ([LLO]=2,5nM).

As for LLO wt with His-tag, the protein used till now for all the experiments, also this form of LLO wt shows differences in pore conductance between acidic and physiological pH. From the conductance histograms reported in Figure 4.43, it is clear the presence of bigger pores at pH 5.5 than pH 7.4. These results support our idea of pH modulation on pore diameter.

## LLO H311A

LLO H331A pores conductances observed are very similar to those of wt: in fact, as reported in Figure 4.44, the mean conductance is around 4 nS at both pHs.

The abolition of pH-dependence of this mutant confirms our hypothesis of His311 importance in luminal pore modulation. This residue is apparently the right one for explaining pH dependence.

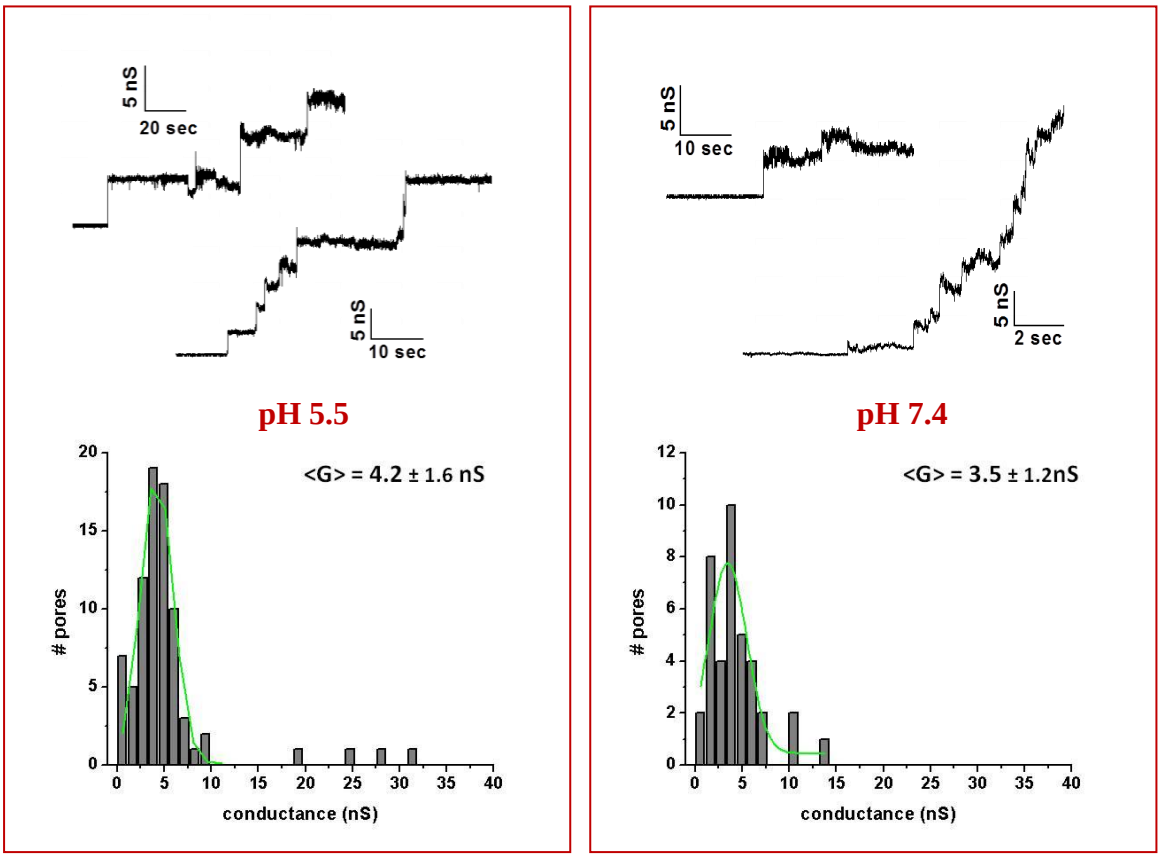


**Figure 4.44 LLO H311A activity on POPC:CHO 1:1 membrane.**

Top panels: some examples of current traces at the two pHs. Bottom panels: cumulative G values histogram. Analyzed pores: 82 pores at pH 5.5 ([LLO]=5nM) and 38 pores at pH 7.4 ([LLO]=2,5nM).

After this first mutant, other mutants at the same 311 position were created changing the moiety of the residue (side chain charge, hydrophobicity, length, ecc.) trying to understand better how Histidine can act as modulator of pore conductance. We planned to substitute the His residue with negatively or positively charged ones, or to hydrophobic ones, in order to understand the kind of interaction in which His residue is involved. Unfortunately, not all the substitutions produced complete proteins and we were able to produce only two other LLO mutants, H311L and H311S, but not the negative charged H311E and the positive charged H311K.

## LLO H311S

Serine residue is another non titratable residue in the pH range tested but the lateral chain is slightly longer than Alanine, so maybe it can highlight some other aspect of His modulation activity. As for H311A, I tested this mutant on POPC:CHO 1:1 membrane at the two pHs.

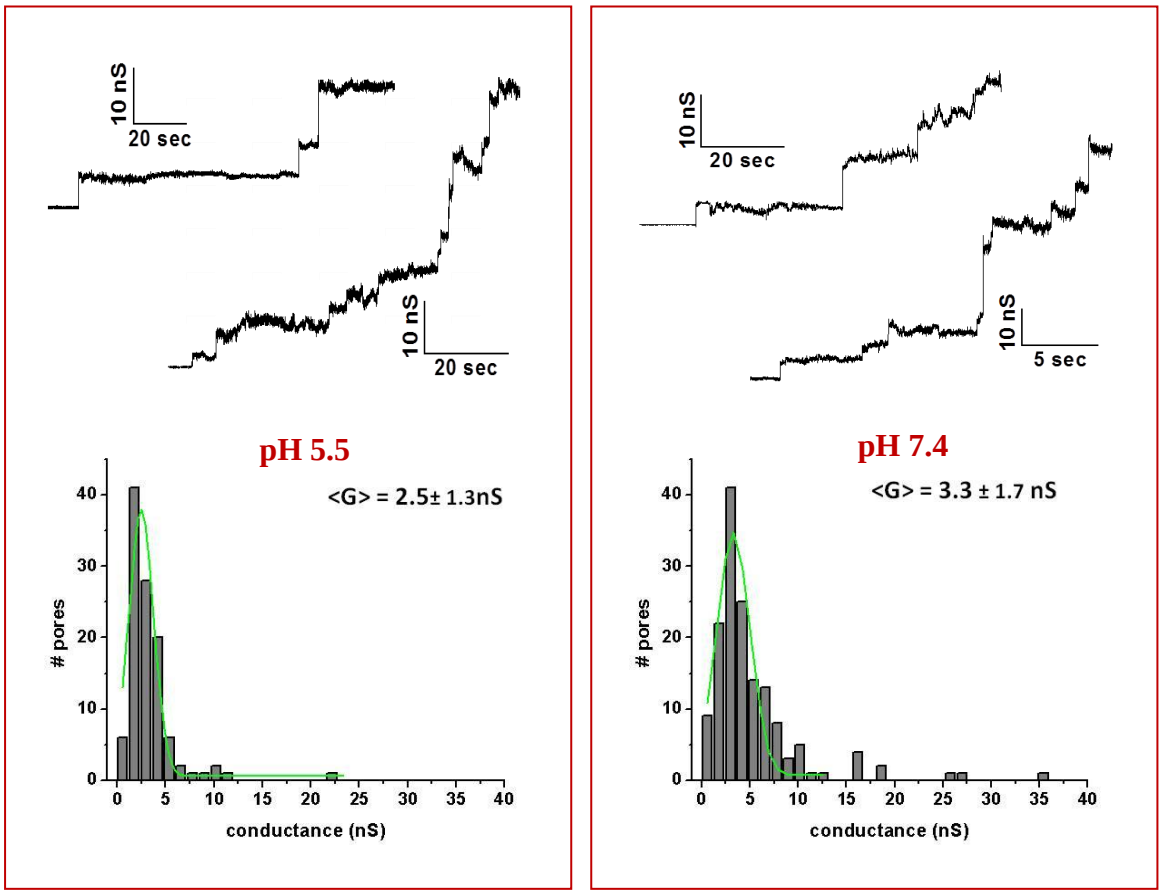


**Figure 4.45 LLO H311S activity on POPC:CHO 1:1 membrane.**

Top panels: some examples of current traces at the two pHs. Bottom panels: cumulative G values histogram. Analyzed pores: 109 pores at pH 5.5 ([LLO]=5nM) and 152 pores at pH 7.4 ([LLO]=2,5nM).

The conductance histogram reported in Figure 4.45 demonstrated the insensitivity of Ser residue to the pH, as expected and as it is seen for Alanine residue. From the mutants analyzed so far, it seems that the slight positivity of His residue at pH 5.5 is the reason of diameter dimension modulation.

## LLO H311L

The last mutant analyzed is LLO H311L. Leucine residue is still not titrable like Ala and Ser but the lateral chain is longer and more similar to His one.

Also in this case, we expected the same pore-forming abilities at pH 5.5 and 7.4, instead, surprisingly, H311L mutant showed something different.

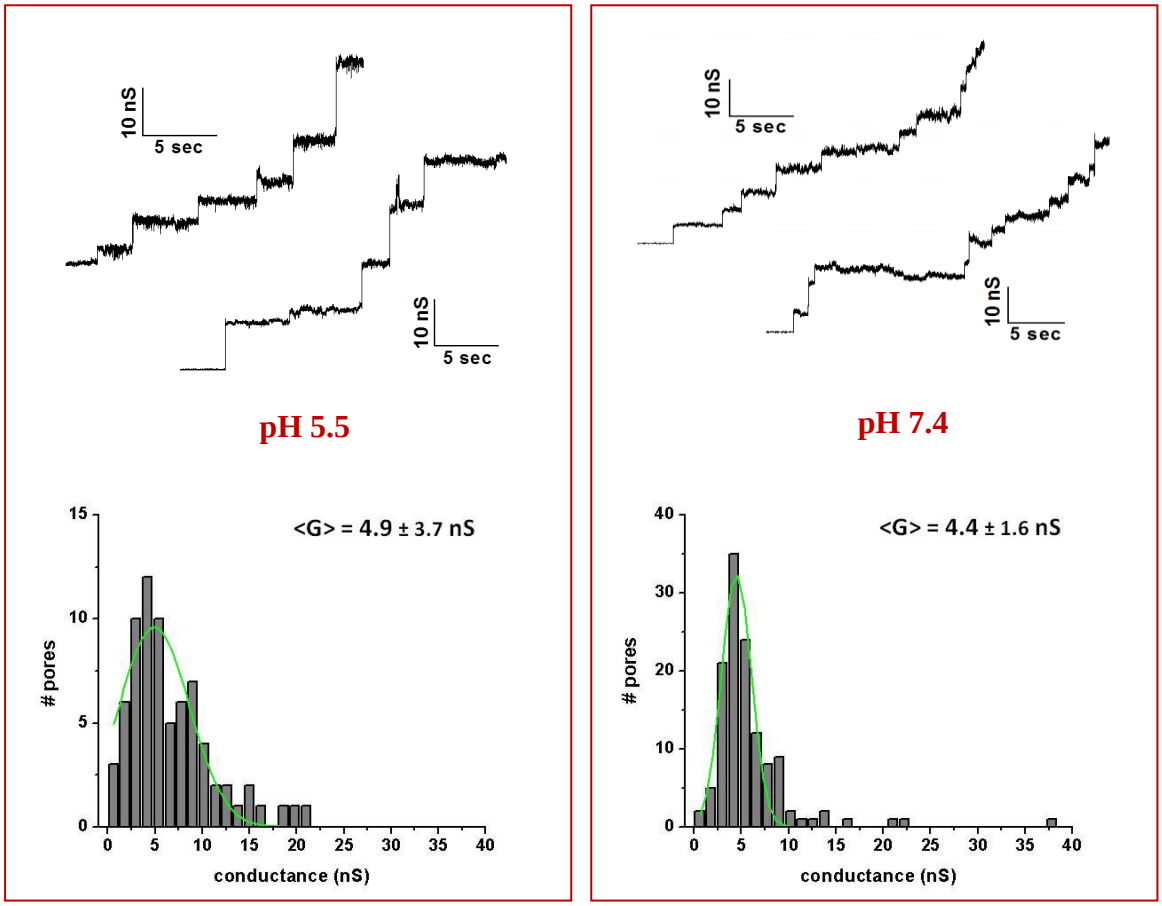


**Figure 4.46 LLO H311L activity on POPC:CHO 1:1 membrane.**

Top panels: some examples of current traces at the two pHs. Bottom panels: cumulative G values histogram. Analyzed pores: 74 pores at pH 5.5 ([LLO]=5nM) and 126 pores at pH 7.4 ([LLO]=2,5nM).

In Figure 4.46, in fact, the conductance histograms are pretty much like the ones obtained with wt protein at the two pHs. Obviously, our hypothesis is not completely validate since it is evident that His modulation is not simply linked on NH group titration. We can suppose that His, at pH 5.5, is a key residue both for the positive charge and the steric hindrance of his lateral chain. Probably, His is only one of the players of diameter modulation, but without a certain 3D structure, we can only hypothesize which of the surrounding residues is the one interacting with His.

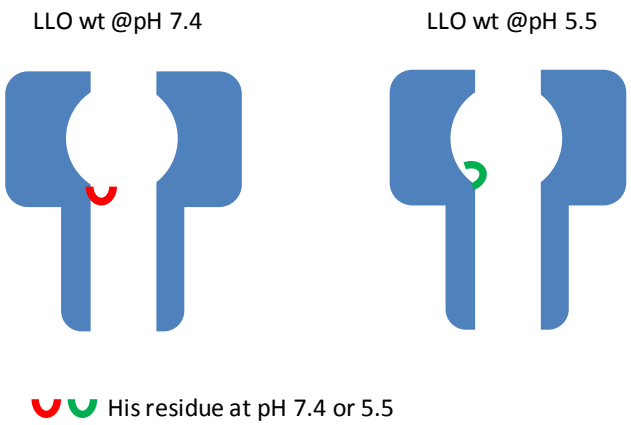


**Figure 4.47 Proposed His residue behavior at the two pHs.**

His at pH 7.4 is more neutral and probably it looses some interaction with the surrounding amino acid residue and partially clogs the luminal part of the pore leading to a smaller inner diameter. At pH 5.5, His residue is less positively charged and electrostatic interactions with the surrounding residues can stretch it to the pore wall, bigger luminal part.

Our preliminary and simplest model is limited by the lack of LLO 3D structure and by the few mutants produced and is based on the assumption that the pore architecture does not change much at the two pHs considered.

At pH 5.5 His311 is slightly positively charged and lies close to the pore walls, where negative fixed charges in proximity to position 311 could stabilize its staying there. The pore lumen is large and permits high ion flux. At pH 7.4 His is uncharged, so it can detach from the pore walls and partially clog the pore lumen. This will reduce the ion current.

Ala in H311A is insensitive to pH and its conductance does not change. It is in the low conductance state since Ala is free to wave into the pore lumen. Similarly Ser in H311S is hydrophilic but neutral and not titratable: this mutant is insensitive to pH change and shows a low conductance state as for H311A. Leu in H311L is hydrophobic, so it should be insensitive to pH. Our experimental data are not so clear with this mutant. The exposition of Leu to the pore lumen could cause some torsions into the local protein structure for lodging it closer to the more convenient lipid environment.

## 4.10. Perforin results

Perforin (PFN) pore-forming activity is known since the protein was discovered as the lytic component of NK-cells. Many studies characterized the role of this protein in the immune system response but till a few years ago, less was known about the tridimensional structure and the pore forming mechanism. As reported in the introduction, PFN is involved in granule-mediated apoptosis, a phenomenum that facilitates the intracellular delivery of granule-associated proteases (granzymes, Gzm) to the host cell. Since PFN is involved in apoptotic stimulation, its pore-forming activity needs to be perfectly tuned otherwise its pores can lead to necrotic death (with subsequent cytoplasmic components release, inflammation and death). The structural similarity of Perforin with Cholesterol-Dependent Cytolysins (Law et al., 2010) allows the association with the pore-forming mechanisms proposed for CDC toxins, ring pore and arc shaped pore. In Praper et al., 2011a, Perforin cytolytic activity was characterized by Planar Lipid Membrane technique on different membrane compositions. From this study, the authors identified that Perforin is able to rearrange into different pore structures depending on membrane properties. Ordered phospholipids and cholesterol presence in the membrane promote more defined and stable pore formations, while, in the presence of more disordered phospholipid, PFN pores are less regular and very noisy. The current trace noise was used by the authors to proposed a model comprising multiple pore structures that could be involved in Grz delivery. GrzB can pass directly through the PFN pores (rings) or can be internalized in endosomal vesicles together with PFN. The internalization can be stimulate by calcium influx (ions passage through PFN transient pores) or can be stimulated directly by PFN. It was, in fact, demonstrated that PFN is able to induce invagination in GUVs (Giant Unilamellar Vesicles) without membrane disruption (Praper et al., 2011b). The presence of this vesicle induction could be another pathway through which PFN promotes Grz delivery. Studies in cells (Metkar et al., 2011) demonstrated the influence of PFN apoptosis promotion, but, most important, the PFN-dependent translocation of phosphatidylserine (PS) to the external leaflet as a prelude of granzyme internalization. This flip flop of anionic phospholipids can be explained by the presence of a toroidal pore (arc pores) composed of an incomplete PFN oligomers and plasma lipids. The hypothesis is that these arc-shaped pore would allow the translocation of cationic granzymes through the bilayer to anionic inner leaflet, mechanism similar to cell penetrating peptides.

### 4.10.1. Perforin activity on Planar Lipid Membrane

Our collaborators suggested to us to investigate the effect of an antihuman PFN Ab (pf-80), known to rescue target cells from PFN-mediated necrosis (Zuber et al., 2005) on pore forming activity (probable effect speculated by cell experiments of increasing arc formation). So we started the characterization of PFN on pure lipid membrane and checked the pore-forming abilities in presence and absence of Pf-80. The membrane used is POPC:CHO 1:1 at pH 7.4, composition in which it is known ring pores are the major PFN structures (Praper et al., 2011a). Electrophysiological measurement were made in the presence of PFN without the Ab and with increasing concentrations of Pf-80. PFN concentration used was 100 ng/ml and those of PFN:Pf-80 tested were 1:0.25, 1:0,5, 1:1. Similar concentrations of Pf-80 alone was tested as negative controls. In the following panel, I report some examples of traces obtained on POPC:CHO 1:1 membrane.

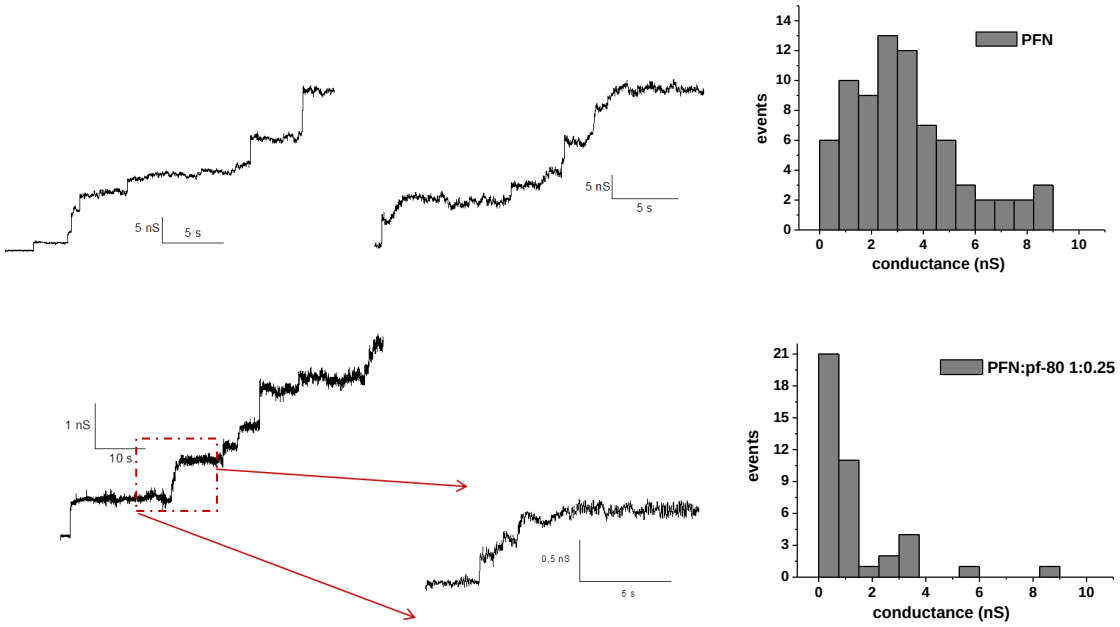


**Figure 4.48 PFN activity with or without Pf-80 on POPC:CHO 1:1 membrane.**

On the left, some examples of PFN activities (top PFN:Pf-80 1:0 and bottom PFN:Pf-80 1:0.25). On the right, the corresponding cumulative G histograms (75 pores and 41 pores respectively).

In this membrane composition, PFN formed mostly well define step-like increase, ring pores, but interestingly there were also some pores opened as a step with a subsequent current increase to reach a final plateau like in Figure 4.48. Based on this results, we hypothesized a model of pore-forming activity of PFN visualized by our PLM technique.

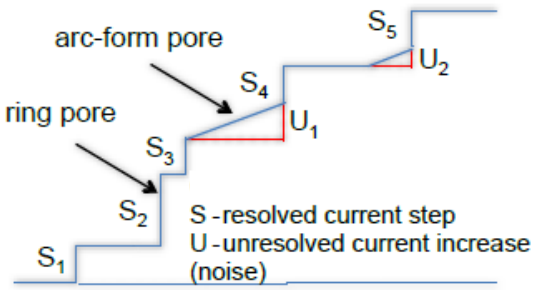


**Figure 4.49 Model of ring pore and arc-form pore visualized by PLM**

From this model, analysis of define step and increasing current can give us an estimation of ring or arcs that can be fixed or can grow by PFN monomer addition. I reported in Figure 4.50 the conductance of the pores visualized by PFN:Pf-80 1:0, PFN:Pf-80 1:0.25, PFN:Pf-80 1:0.5. For PFN:Pf-80 1:1 experiments, PFN activity was more difficult to analyze as step-like increase are not visible and PFN seemed to perturb the membrane more than open a pore.

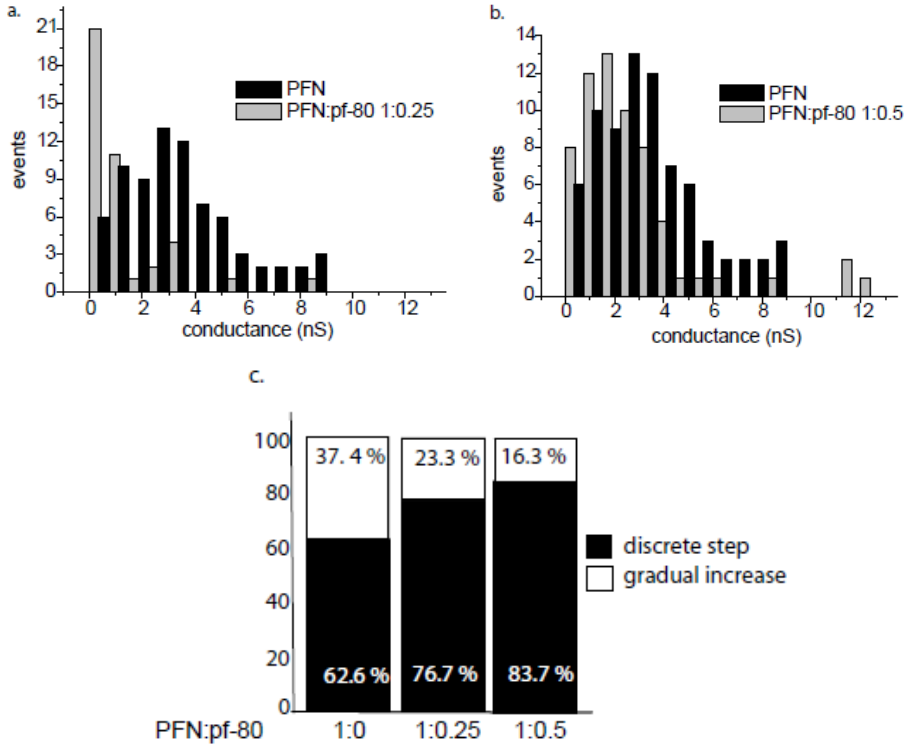


**Figure 4.50 Pore analysis of PFN:Pf-80 ratio.**

a-b) cumulative histogram of PFN pores; c) discrete step vs gradual increase analysis

The PLM results indicate that Pf-80 promotes the formation of smaller pore that could be associated to arc pores since the epitope of this Ab is accessible only in the not inserted PFN monomer. The binding blocks PFN structure as an arc-form and does not allow further oligomerization (i.e. growing of the arc).

### 4.10.2. AFM images of PFN structures

Our results indicate that the binding of Pf-80 to PFN monomer blocks the formation of a complete ring pores, promoting a ring:arc ratio more towards the second structure. In order to confirm our hypothesis of pore structures, we decided to visualize the same tested sample by AFM. On POPC membrane, PFN formed very define ring structures of variable dimension, some arc-shaped structures and some interconnected structures (especially in PFN:Pf-80 1:0 sample)..

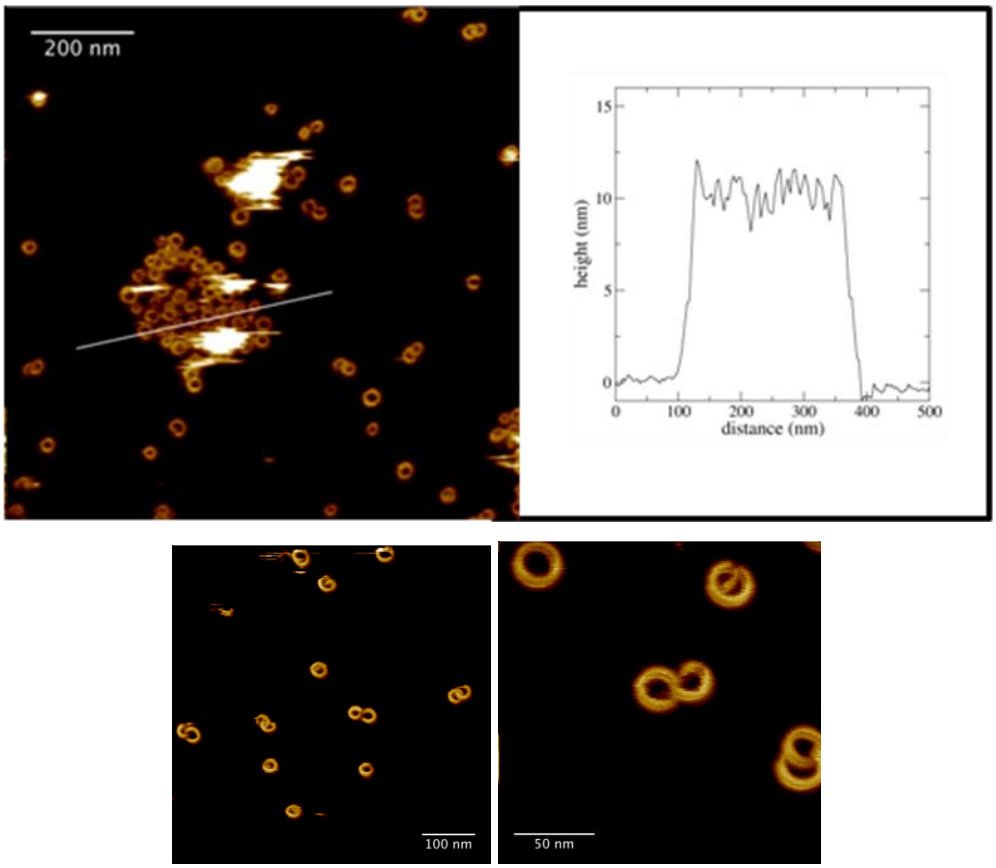


**Figure 4.51 PFN structures on POPC membrane.**

Top panel: Pore structures image and profile of the selected line in the image. PFN concentration used 12.5nM. Bottom panel: a field of PFN structures and a magnification of the interconnected structures.

The reason of this kind of conformation is not clear and since PFN has the same height both in bound configuration that in the inserted version, so it is impossible to discriminate if they are active or not.

In the presence of Pf-80, the scenario was similar but in these samples the presence of the bound antibody promotes arc formation.

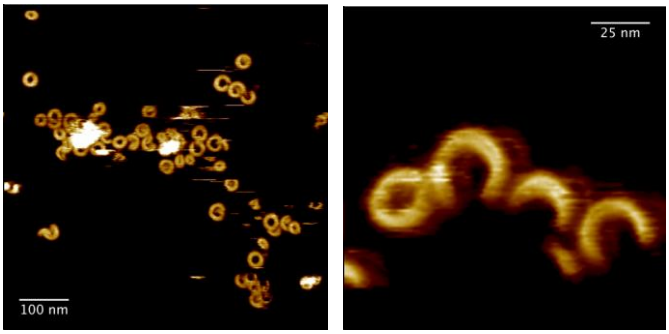


**Figure 4.52 PFN:Pf-80 1:0.25 sample visualized by AFM.**

Right image a magnification of another fields of the sample showing very define arc form.

Summarizing all the experiments in ring:arc ratio, we could confirm that the Ab Pf-80 binds to PFN oligomers blocking the oligomer growth and promoting the arc-shaped pore configuration.

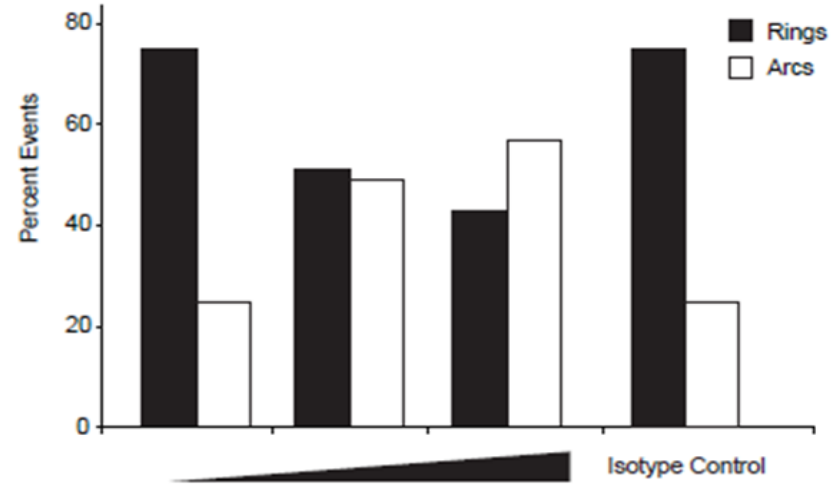


**Figure 4.53 Percentage summary of rings and arcs from AFM experiments.**

Isotype Ab was used as negative control.

Moreover, the AFM data, combined with PLM data, showed that in the presence of Pf-80, the small formed pores could be considered mostly arc-shaped pores.

# 5. Conclusions

In the literature, two physiological configurations of CDCs and Perforin pores are proposed: ring and arc structure that could have different implication on the biological mechanism of action of these PFPs. By using artificial membrane with different lipid compositions, we are able to enrich the ring or the arc fraction allowing a molecular and structural characterization of the two physiological structures.

In fact, starting from the information on PFO-binding modulation to different membrane compositions (Flanagan et al., 2009; Nelson et al., 2007), we discriminated the two different pore-forming structures and demonstrated that both of them are indeed active, i.e. they are both able to conduct ions. From PLM analysis of PFO and LLO ion current data, we identified two membrane compositions that strongly promote either ring formations or arciform oligomers. In fact, on POPC:CHO 1:1 membrane both PFO and LLO formed well defined and stable pores that are visualized in PLM traces as step-like increases in ionic current. AFM studies under similar experimental conditions allowed us to visualize the pores that were mostly ring-shaped with only few arciform structures and some interconnected assemblies (visible only on PFO samples). We tried to correlate the pore dimension calculated from the measured conductance values with the diameter of the ring structures visualized by AFM. The trend is respected, even though the absolute didn't coincide as we were indeed comparing two different kinds of diameter as schematized in Figure 5.1. In fact, with PLM measurement we were looking at the luminal part of the pore (the real path of membrane perforation), instead with AFM we could only measure the diameter of the highest part of the pore.

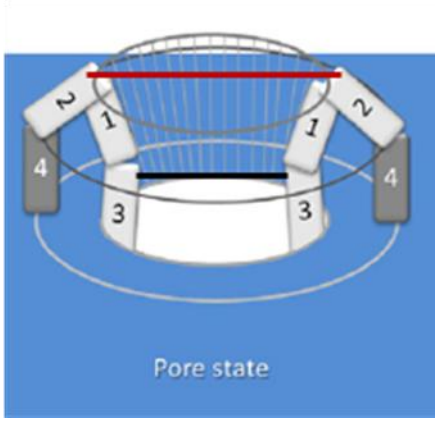


**Figure 5.1 Cartoon of CDCs pore state.**

In the figure, the two different dimensions highlighted by red and black lines correspond to the AFM diameter estimation and the electrophysiological calculated diameter of the pore. (Figure modified from Hupp et al., 2013).

On DOPC:CHO 4:1 membrane, instead, both toxins presented a less stable pore structure, functionally characterized by unresolved increases in ionic current. In PFO sample, this behavior is surely the most frequent one with no possibility of seeing discrete steps, meaning that ionic paths through the membrane are not related to stable oligomeric arrangements. We speculated that this activity may be due to the growing of arc-shaped oligomers by the sequential insertion of newly recruited monomers. AFM studies on this membrane composition visualized incomplete oligomeric forms, mostly arc-liked configurations which could be correlated with the not defined electrophysiological activity.
Thus AFM allowed us to visualize the architecture of pores formed on the different conditions, which were either full rings or incomplete arcs. Thanks to the CDCs' vertical collapse, we were able to understand if the imaged structures were active or inactive pores. All the structures visualized by AFM had an height compatible with inserted protein structures (around 7 nm). Moreover, analysis of a blocked LLO version confirmed that both rings and arcs were organized in a pre-pore configuration and that the two structures, after re-activation, were able to insert into the membrane and open active pores.
In order to have a complete characterization of the arc structures and formation, it will be necessary to investigate the pore opening kinetics both measuring current passage and visualizing the responsible oligomeric structure, possibly on the same sample. This goal is very challenging because of the small pore dimensions that imposes the use of nano-resolution technologies combined with electrophysiological measurements.
In the future, we would like to go deeper into arc formation aspects studying other features that can confirm our hypothesis of arc-shaped promotion, for example investigating changes in lipid flip-flop rate, that is an indirect evidence of toroidal pore formation.
LLO results obtained at the two different pHs revealed that LLO is subjected to a modulation of the luminal profile of the pore in response to pH changes, besides the already reported inactivation by premature unfurling of the monomer before membrane binding. We identified the histidine at position 311 as an amino acid involved in this modulation; further investigations will be necessary to understand the titration mechanism and to find other residues eventually involved.

Similar pore structures were visualized also in the analysis of human perforin. Thanks to the use of a monoclonal antibody Pf-80, we were able to promote a preferential formation of arciform oligomers. The modulating effect of Pf-80 can be used to understand the role of PFN in Grz internalization. Interestingly, arciform pores involve changes in the lamellar

structure of the cell membrane, with a connection between internal and external leaflets visible also as PS increasing exposure in high-throughput cell experiments. Besides increasing the flip-flop rate which may speed up exchanges of lipid bound receptors, this lipid feature resembles that adopted in vesicle fusion. Both routes may play a key role in PFN facilitated Gzm uptake.

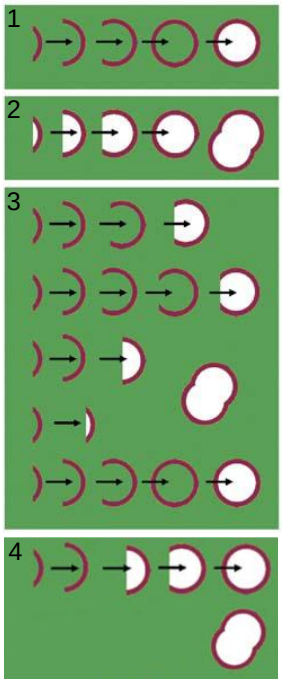


**Figure 5.2 Pore-forming mechanisms improved from the two present in literature.**

1) ring pore insertion; 2) growing arc formation; 3) multiple mechanism due to protein availability; 4) defined minimal arc formation with possible subsequent oligomeric growing.

Collectively, our results demonstrated the presence of several pore-forming mechanisms that can lead to different protein features in pathogenesis (CDCs protein) and immune synaptic response (PFN).

# 6. Acknowledgements

At the end of my Ph.D. period, I want to acknowledge everyone that, in several ways, have been present to support me during this experience.

Starting from the scientific people I want to thank:

*Mauro* to allow me to joint his group and to start a long, and not always easily, way in the biophysical world. I image that I'm not fully converted but I started to think in a more physical way.

*Menestrina's wife* and the *CNR* for supporting my fellowship that allow me to enter in the pore-forming study.

*Gregor Anderluh* (National Institute of Chemistry at Ljubljana) for hosting me in his lab to express all the LLO proteins, for the useful discussion and the scientific support on double mutants design and characterization.

*Lorenzo Lunelli* (Bruno Kessler Foundation) for his constant presence in AFM experiments. Thanks for the uncountable hours on the microscope to obtain the beautiful images and for the support with the result analysis.

*Tilen* and *Sunil* to give me all the acknowledge about perforin useful for the experiments. Thanks *Sunil Metkar*, and *Chris Froelich*, from Department of Medicine, Evanstone, to provide me human purified PFN and the monoclonal Ab;

*"Mauro's Angels" group: Laura, Manuela and Valeria*. Valeria as advisor but also introducing me into PLM experiments with LLO and helping me to improve my knowledge on CDCs and to increase my PLM data; Manuela, my lab guide at the beginning of the PhD and invaluable source of advice during all these years; Laura, always present during the PLM long time consuming experiments without results (lab coat and pen holder creative moments!). Thank you both, Manuela and Laura, also for the funny moments outside work.

*Framba*, the theoretical physicist that have made me crazy with never ending discussion of physical, electronic, computer and any other topics. If my mind is more physicist-like, it's for you.

*The two "hybrid physicists" Lorenza e Francesco*. Lorenza to all the time spent together during this PhD experience (lessons, seminars, and lab times). Francesco, who explain to me physical problems in a biologically-friendly manner and for all

the time spent together in office, lab and to keep me in touch with Trento since I was in Ljubljana.

*All the researchers that work, or had worked, in the joint lab*: Cristina, Laura P., Lavinia, Paola, Matteo, Sonja, Josè, Liaisan, Aurora, Michele, Veronica, Roberto, Gabriella, Daniele, Silvia, Carlo and Cecilia…I hope to have mention all people…Thanks to have shared the lab time, to the lunch time together and all the chat and laughter.

*My office mate:* Gaia, Laura, Francesco, Faraz and Fabio. Sorry for my loud "talking to myself" moments during thesis writing. I hope I didn't disturb you so much.

At the end I want to thank the not scientific-working people:

*My parents, my sister, my grand-parents, uncles and aunts and any other relatives* that are so happy to see me and chat with me during my week-end trips at Vicenza. I really love knowing how much you support me and I something missed not to be closer like before.

*All my friends from Vicenza* which continue to be my friends even if we are not so closed during this last year. Now, I think I will have more time to get together.

*Diego* to be my life landmark, to comfort me in the difficulties, to tolerate my stress and madness (non te ghé tute le fassine al coerto) moments. Thanks for all the beautiful moments that we had and hopefully will have.

Just to conclude…thanks you all, also the one I do not mention but present in my thoughts, that have made a change (even smaller) in my life. I think I've grown a lot as a scientist but also as a person. Thank you all!!!!!!

# 7. Bibliography

Aleshin, A.E., Schraufstatter, I.U., Stec, B., Bankston, L.A., Liddington, R.C., and DiScipio, R.G. (2012). Structure of Complement C6 Suggests a Mechanism for Initiation and Unidirectional, Sequential Assembly of Membrane Attack Complex (MAC). Journal of Biological Chemistry *287*, 10210–10222.

Alouf, J.E., Billington, S.J., and Jost, B.H. (2006). Repertoire and general features of the family of cholesterol-dependent cytolysins. The Comprehensive Sourcebook of Bacterial Protein Toxins *3*.

Anderluh, G., and Lakey, J.H. (2008). Disparate proteins use similar architectures to damage membranes. Trends in Biochemical Sciences *33*, 482–490.

Bavdek, A., Gekara, N.O., Priselac, D., Gutiérrez Aguirre, I., Darji, A., Chakraborty, T., Maček, P., Lakey, J.H., Weiss, S., and Anderluh, G. (2007). Sterol and pH Interdependence in the Binding, Oligomerization, and Pore Formation of Listeriolysin O †. Biochemistry *46*, 4425–4437.

Billington, S.J., Songer, J.G., and Jost, B.H. (2002). The variant undecapeptide sequence of the Arcanobacterium pyogenes haemolysin, pyolysin, is required for full cytolytic activity. Microbiology *148*, 3947–3954.

Czajkowsky, D.M., Hotze, E.M., Shao, Z., and Tweten, R.K. (2004). Vertical collapse of a cytolysin prepore moves its transmembrane β-hairpins to the membrane. The EMBO Journal *23*, 3206–3215.

Dalla Serra, M.D., and Menestrina, G. (2000). Characterization of Molecular Properties of Pore-Forming Toxins with Planar Lipid Bilayers. In Bacterial Toxins: Methods and Protocols, O. Holst, ed. (Humana Press), pp. 171–188.

Dunstone, M.A., and Tweten, R.K. (2012). Packing a punch: the mechanism of pore formation by cholesterol dependent cytolysins and membrane attack complex/perforin-like proteins. Current Opinion in Structural Biology.

Farrand, A.J., LaChapelle, S., Hotze, E.M., Johnson, A.E., and Tweten, R.K. (2010). Only two amino acids are essential for cytolytic toxin recognition of cholesterol at the membrane surface. Proceedings of the National Academy of Sciences *107*, 4341–4346.

Flanagan, J.J., Tweten, R.K., Johnson, A.E., and Heuck, A.P. (2009). Cholesterol Exposure at the Membrane Surface Is Necessary and Sufficient to Trigger Perfringolysin O Binding. Biochemistry *48*, 3977–3987.

Froelich, C.J., Orth, K., Turbov, J., Seth, P., Gottlieb, R., Babior, B., Shah, G.M., Bleackley, R.C., Dixit, V.M., and Hanna, W. (1996). New Paradigm for Lymphocyte Granule-mediated Cytotoxicity Target Cells Bind And Internalize Granzyme B, But An Endosomolytic Agent Is Necessary For Cytosolic Delivery And Subsequent Apoptosis. Journal of Biological Chemistry *271*, 29073–29079.

Gilbert, R.J.C. (2005). Inactivation and activity of cholesterol-dependent cytolysins: what structural studies tell us. Structure *13*, 1097–1106.

Gilbert, R.J.C., Mikelj, M., Dalla Serra, M., Froelich, C.J., and Anderluh, G. (2012). Effects of MACPF/CDC proteins on lipid membranes. Cellular and Molecular Life Sciences.

Hamon, M.A., Ribet, D., Stavru, F., and Cossart, P. (2012). Listeriolysin O: the Swiss army knife of Listeria. Trends in Microbiology.

Hotze, E.M., and Tweten, R.K. (2012). Membrane assembly of the cholesterol-dependent cytolysin pore complex. Biochimica Et Biophysica Acta (BBA) - Biomembranes *1818*, 1028–1038.

Hotze, E.M., Le, H.M., Sieber, J.R., Bruxvoort, C., McInerney, M.J., and Tweten, R.K. (2012). Identification and characterization of the first cholesterol-dependent cytolysins from Gram-negative bacteria. Infect. Immun.

Hupp, S., Förtsch, C., Wippel, C., Ma, J., Mitchell, T.J., and Iliev, A.I. (2013). Direct Transmembrane Interaction between Actin and the Pore-Competent, Cholesterol-Dependent Cytolysin Pneumolysin. Journal of Molecular Biology *425*, 636–646.

Kondos, S.C., Hatfaludi, T., Voskoboinik, I., Trapani, J.A., Law, R.H.P., Whisstock, J.C., and Dunstone, M.A. (2010). The structure and function of mammalian membrane-attack complex/perforin-like proteins. Tissue Antigens *76*, 341–351.

Law, R.H.P., Lukoyanova, N., Voskoboinik, I., Caradoc-Davies, T.T., Baran, K., Dunstone, M.A., D'Angelo, M.E., Orlova, E.V., Coulibaly, F., Verschoor, S., et al. (2010). The structural basis for membrane binding and pore formation by lymphocyte perforin. Nature *468*, 447–451.

Metkar, S.S., Wang, B., Catalan, E., Anderluh, G., Gilbert, R.J.C., Pardo, J., and Froelich, C.J. (2011). Perforin Rapidly Induces Plasma Membrane Phospholipid Flip-Flop. PLoS ONE *6*, e24286.

Mueller, M., and Ban, N. (2010). Enhanced SnapShot: Pore-Forming Toxins. Cell *142*, 334–334.e1.

Nelson, L.D., Johnson, A.E., and London, E. (2007). How Interaction of Perfringolysin O with Membranes Is Controlled by Sterol Structure, Lipid Structure, and Physiological Low pH: Insights Into The Origin Of Perfringolysin O-Lipid Raft Interaction. Journal of Biological Chemistry *283*, 4632–4642.

Niesen, F.H., Berglund, H., and Vedadi, M. (2007). The use of differential scanning fluorimetry to detect ligand interactions that promote protein stability. Nature Protocols *2*, 2212–2221.

Njoku-Obi, A.N., Jenkins, E.M., Njoku-Obi, J.C., Adams, J., and Covington, V. (1963). Production And Nature Of Listeria Monocytogenes Hemolysins. J Bacteriol *86*, 1–8.

Palmer, M., Harris, R., Freytag, C., Kehoe, M., Tranum-Jensen, J., and Bhakdi, S. (1998). Assembly mechanism of the oligomeric streptolysin O pore: the early membrane lesion is

lined by a free edge of the lipid membrane and is extended gradually during oligomerization. The EMBO Journal *17*, 1598–1605.

Pipkin, M., and Lieberman, J. (2007). Delivering the kiss of death: progress on understanding how perforin works. Current Opinion in Immunology *19*, 301–308.

Praper, T., Beseni\vcar, M.P., Istini\vc, H., Podlesek, Z., Metkar, S.S., Froelich, C.J., and Anderluh, G. (2010). Human perforin permeabilizing activity, but not binding to lipid membranes, is affected by pH. Molecular Immunology *47*, 2492–2504.

Praper, T., Sonnen, A., Viero, G., Kladnik, A., Froelich, C.J., Anderluh, G., Dalla Serra, M., and Gilbert, R.J.C. (2011a). Human perforin employs different avenues to damage membranes. Journal of Biological Chemistry *286*, 2946–2955.

Praper, T., Sonnen, A.F.P., Kladnik, A., Andrighetti, A.O., Viero, G., Morris, K.J., Volpi, E., Lunelli, L., Dalla Serra, M., and Froelich, C.J. (2011b). Perforin activity at membranes leads to invaginations and vesicle formation. Proceedings of the National Academy of Sciences *108*, 21016–21021.

Ramachandran, R., Heuck, A.P., Tweten, R.K., and Johnson, A.E. (2002). Structural insights into the membrane-anchoring mechanism of a cholesterol-dependent cytolysin. Nat Struct Mol Biol *9*, 823–827.

Ramachandran, R., Tweten, R.K., and Johnson, A.E. (2004). Membrane-dependent conformational changes initiate cholesterol-dependent cytolysin oligomerization and intersubunit β-strand alignment. Nature Structural & Molecular Biology *11*, 697–705.

Rosado, C.J., Buckle, A.M., Law, R.H.P., Butcher, R.E., Kan, W.-T., Bird, C.H., Ung, K., Browne, K.A., Baran, K., Bashtannyk-Puhalovich, T.A., et al. (2007). A Common Fold Mediates Vertebrate Defense and Bacterial Attack. Science *317*, 1548–1551.

Rossjohn, J., Feil, S.C., McKinstry, W.J., Tweten, R.K., and Parker, M.W. (1997). Structure of a cholesterol-binding, thiol-activated cytolysin and a model of its membrane form. Cell *89*, 685–692.

Saunders, F.K., Mitchell, T.J., Walker, J.A., Andrew, P.W., and Boulnois, G.J. (1989). Pneumolysin, the thiol-activated toxin of Streptococcus pneumoniae, does not require a thiol group for in vitro activity. Infection and Immunity *57*, 2547–2552.

Schuerch, D.W., Wilson-Kubalek, E.M., and Tweten, R.K. (2005). Molecular basis of listeriolysin O pH dependence. PNAS *102*, 12537–12542.

Shepard, L.A., Shatursky, O., Johnson, A.E., and Tweten, R.K. (2000). The Mechanism of Pore Assembly for a Cholesterol-Dependent Cytolysin: Formation of a Large Prepore Complex Precedes the Insertion of the Transmembrane β-Hairpins †. Biochemistry *39*, 10284–10293.

Thiery, J., Keefe, D., Boulant, S., Boucrot, E., Walch, M., Martinvalet, D., Goping, I.S., Bleackley, R.C., Kirchhausen, T., and Lieberman, J. (2011). Perforin pores in the endosomal membrane trigger the release of endocytosed granzyme B into the cytosol of target cells. Nature Immunology *12*, 770–777.

Tilley, S.J., Orlova, E.V., Gilbert, R.J.C., Andrew, P.W., and Saibil, H.R. (2005). Structural basis of pore formation by the bacterial toxin pneumolysin. Cell *121*, 247–256.

De los Toyos, J.R., Méndez, F.J., Aparicio, J.F., Vazquez, F., Del Mar Garcia Suarez, M., Fleites, A., Hardisson, C., Morgan, P.J., Andrew, P.W., and Mitchell, T.J. (1996). Functional analysis of pneumolysin by use of monoclonal antibodies. Infection and Immunity *64*, 480–484.

Tweten, R.K. (2005). Cholesterol-dependent cytolysins, a family of versatile pore-forming toxins. Infection and Immunity *73*, 6199–6209.

Vadia, S., Arnett, E., Haghighat, A.-C., Wilson-Kubalek, E.M., Tweten, R.K., and Seveau, S. (2011). The Pore-Forming Toxin Listeriolysin O Mediates a Novel Entry Pathway of L. monocytogenes into Human Hepatocytes. PLoS Pathogens *7*, e1002356.

Young, J.D.E., Hengartner, H., Podack, E.R., and Cohn, Z.A. (1986). Purification and characterization of a cytolytic pore-forming protein from granules of cloned lymphocytes with natural killer activity. Cell *44*, 849–859.

Zuber, B., Levitsky, V., Jönsson, G., Paulie, S., Samarina, A., Grundström, S., Metkar, S., Norell, H., Callender, G.G., Froelich, C., et al. (2005). Detection of human perforin by ELISpot and ELISA: ex vivo identification of virus-specific cells. J. Immunol. Methods *302*, 13–25.